Author:
Boukley Hasan, Wael

Title:
On Evaluating the Practicality of Using Massive MIMO in Real-World Scenarios and Identifying Solutions to Operational Deployments

On Evaluating the Practicality of Using Massive MIMO in Real-World Scenarios and Identifying Solutions to Operational Deployments

By

WAEL BOUKLEY HASAN

Department of Electrical & Electronic Engineering
UNIVERSITY OF BRISTOL

A dissertation submitted to the University of Bristol in accordance with the requirements of the degree of DOCTOR OF PHILOSOPHY in the Faculty of Engineering.

JANUARY 2019

Word count: 46,969

Abstract

We tend to assume that pervasive wireless connectivity exists everywhere, and with new applications such as Virtual Reality, Autonomous Driving and the Internet of Things, this with require a 1000-fold increase in capacity by 2020 based on cellular capacity in 2016. This increase now presents significant challenges to wireless system designers. The majority of consumer wireless technologies currently operate using spectrum between 380MHz and 6GHz. Given the favourable propagation for cellular communications, wireless local area networking (Wi-Fi), terrestrial television broadcasting and radar, this spectral spot has become extremely crowded, and mechanisms to enhance the spectrum efficiency are thus needed. Massive multiple-input, multiple-output (Ma-MIMO) enables efficient utilization of the limited radio resources providing significant capacity improvement by multiplexing more simultaneous users within the same radio resource by means of spatial domain signal processing.

This thesis evaluates the practicality of using Ma-MIMO in real-world scenarios and identifies solutions to operational deployments as they are uncovered. At the time this work commenced, only a few real-time evaluations had been conducted and the majority of the theoretical papers were not validated. The work in this thesis presents the per-cell spectral efficiency (SE) of 145.6 bits/s/Hz achieved with a 128-antenna Ma-MIMO testbed and introduces the challenges and the limitation factors that were revealed when delivering this level of spectrum efficiency enhancement. Here, the Ma-MIMO channel robustness is evaluated through various indoor and outdoor field trials, and the improved channel robustness was then exploited to design a simple uplink closed loop power control scheme.

This thesis also introduces novel adaptive user grouping algorithms to further enhance the Ma-MIMO advantages for different applications. The algorithms presented address the interference caused by the multiple simultaneous user channel vectors in the same frequency-time domain as well as errors due to hardware impairments. This can be achieved by means of a novel error vector magnitude (EVM) prediction method proposed herein. Importantly, all the proposed algorithms and approaches in this thesis have been evaluated experimentally by means of a software-defined radio Ma-MIMO testbed.

ACKNOWLEDGEMENTS

First and foremost, I would like to express my sincere thanks for my supervisors, Professor Angela Doufexi and Professor Mark Beach for giving me the opportunity to work on this project and for their continuous support and inspiring supervision. Professor Angela guided me through my research and encouraged me enthusiastically. Professor Mark provided me with so many ideas and opportunities to promote the success of this project. I would like to thank Dr. Paul Harris who worked so closely with me and supported technical matters on the massive MIMO testbed. I would also like to thank the massive MIMO team at the University of Bristol, Lund University (Sweden) and National Instruments for all the help provided through a fruitful collaboration.

I thank Engineering and Physical Sciences Research Council (EPSRC) Centre for Doctoral Training (CDT) in communications, British Broadcasting Corporation (BBC) research and development (R&D), Towards Ultimate Convergence All Networks (TOUCAN) and Department of Digital, Culture, Media and Sport (DCMS) for their financial support to build this work. I also thank Bristol City Council for access to the massive MIMO test-bed.

Last but certainly not least, I would like to thank my family for their support and encouragement. My dear wife, Marwa, has been extremely supportive and stood by me through this entire journey. This journey would not have been possible without my parents who made countless sacrifices to help me get to this point.

AUTHOR'S DECLARATION

I declare that the work in this dissertation was carried out in accordance with the requirements of the University's Regulations and Code of Practice for Research Degree Programmes and that it has not been submitted for any other academic award. Except where indicated by specific reference in the text, the work is the candidate's own work. Work done in collaboration with, or with the assistance of, others, is indicated as such. Any views expressed in the dissertation are those of the author.

SIGNED: ..... DATE: .....

TABLE OF CONTENTS

List of Abbreviations

$\mathbf{EVM}^{\mathbf{QPSK}}$ EVM requirements for QPSK

$\mathbf{EVM}^{\mathbf{TH}}$ EVM threshold

$\widetilde{\mathbf{EVM}}$ predicted EVM

$\widetilde{\mathbf{SE}}$ predicted SE

1G first generation mobile system

2G second generation mobile system

3G third generation mobile system

3GPP 3rd Generation Partnership Project

4G fourth generation mobile system

5G fifth generation mobile system

AD Autonomous Driving

ADC analogue-to-digital converter

AoA angle of arrival

AS angular spread

AWGN additive white gaussian noise

BBC British Broadcasting Corporation

BER bit error rate

BF beamforming

BLAST Bell Laboratories Layered Space-Time

BPSK binary phase-shift keying

BS base station

BT British Telecom

BW bandwidth

C2I Collaborate to Innovate

CDMA code-division multiple access

CDT Centre for Doctoral Training

COST European Cooperation in Science & Technology

COTS commercial off-the-shelf

CPA coordinated pilot assignment

CSI channel state information

CSI-RS channel state information RS

CSN Communication Systems & Networks

DAC digital-to-analogue converter

dB decibels

DCMS Department of Digital, Culture, Media and Sport

DDC digital down converter

DL downlink

DPC dirty paper coding

EE energy efficiency

EPSRC Engineering and Physical Sciences Research Council

EVD eigenvalue decomposition

EVM error vector magnitude

FD-MIMO full dimension multiple-input, multiple-output (MIMO)

FDD frequency division duplex

FDMA frequency-divison multiple access

FPGA field-programmable gate array

GP geometric program

GPIO General Purpose Input Output

GPS global positioning system

GSM Global System for Mobile Communications

GUI graphical user interface

HD high-definition

ICI inter-carrier interference

ID identity

IEEE Institute of Electrical and Electronics Engineers

IID independent and indentically distributed

IoT internet of things

ISI inter-symbol interference

IUI inter-user interference

JSDM joint spatial division multiplexing

KPI key performance indicator

LAN local area network

LDPC low-density parity-check

LED light emitting diode

LNA low-noise amplifier

LO local oscillator

LOS line-of-sight

LS least squares

LTE long-term evolution

M2M machine-to-machine

Ma-MIMO massive MIMO

MCS modulation and coding scheme

MF matched filtering

MGS modified gram schmidt

MIMO multiple-input, multiple-output

MMSE minimum mean square error

mmWave millimetre wave

MRC maximal ratio combining

MRT maximal ratio transmission

MS modulation scheme

MSE mean square error

MU multi-user

NI National Instruments

NLOS non-line-of-sight

OCXO oven-controlled crystal oscillator

OFDM orthogonal frequency division multiplexing

OTA over-the-air

P2P peer-to-peer

PA power amplifier

PC power control

PCIe peripheral component interconnect express

PHY physical layer

ppb parts-per-billion

PSS primary synchronisation signal

PXIe peripheral component interconnect express (PCIe) eXtensions for instrumentation

QAM quadrature amplitude modulation

QPSK quadrature phase-shift keying

R&D research and development

RB resource block

RF radio frequency

RMS root-mean-squre

RRH remote radio head

RS reference signal

RTM rear transition module

SC-FDMA single-carrier frequency-division multiple access

SE spectral efficiency

SIC successive interference cancellation

SINR signal to interference plus noise ratio

SISO single-input single-output

SM spatial multiplexing

SNR signal to noise ratio

SU single-user

SVD singular value decomposition

SVS singular value spread

TDD time division duplex

TDMA time-division multiple access

TOUCAN Towards Ultimate Convergence All Networks

TPC transmitter power control

TRX transceiver

TXRU transceiver unit

UCA uniform cylindrical array

UDP User Datagram Protocol

UE user equipment

UHD Ultra-High-Definition

UL uplink

ULA uniform linear array

UMTS Universal Mobile Telecommunications System

USRP universal software radio peripheral

V2I vehicle-to-infrastructure

V2V vehicle-to-vehicle

VNA vector network analyser

WARP Wireless Open-Access Research Platform

WCDMA wide band code-division multiple access

Wi-Fi wireless local area networking

WiMAX Worldwide Interoperability for Microwave Access

ZC Zadoff-Chu

ZF zero-forcing

NOTATION

D_b Calibration matrix downlink channel matrix during the downlink data transmission

E_b Energy per bit (J bit)

F_s Sampling rate (S/s)

G_R Receive Antenna Gain (dBi)

G_T Transmit Antenna Gain (dBi)

I_{Th} Inter-user spatial correlation threshold

K No. of single-antenna user terminals

M No. of base station antennas

N_{CP} Number of samples for OFDM cyclic prefix

N_{FFT} FFT size

N_R Number of receive antennas

N_T number of transmit antennas

N_{Used} Number of used subcarriers

N_o Noise Power Spectral Density (W/Hz)

T_p Uplink pilot periodicity (s)

$T_r[\cdot]$ Trace of matrix

$\Upsilon_{k,l}$ Partial EVM^2 error estimation value for user k which is caused only by user l

$\|\cdot\|$ Frobenius norm

Ξ Sum of eigen values for channel matrix $\boldsymbol{H}$

λ Wavelength (m)

$(\cdot)^{+}$ Moore-Penrose Psuedo Inverse

$(\cdot)^{H}$ Hermitian transpose

$|\cdot|$ Euclidean norm

$\mathbb{A}(\cdot)$ Adjugate operator

$\mathscr{A}$ A group of users

$\mathscr{G}$ A group vector where the index of the vector represents the group number and each group contains a set of users

$\mathscr{L}$ A vector of size K which contains the user IDs

$\mathscr{U}$ A set of un-assigned user equipment (UE)s waiting to be assigned into group $\mathscr{A}$

ν The average EVM prediction for a set of users in a group

ψ The SE prediction for a set of users in a group

ρ Transmitted power

ρ_R Received power

σ_n Noise variance

$\tilde{\boldsymbol{s}}$ Estimated downlink symbol vector

$\tilde{\boldsymbol{x}}$ estimated uplink symbol vector

$\boldsymbol{E}_{dl}$ The difference between the estimated channel and the actual channel during the downlink data transmission

$\boldsymbol{E}_{ul}$ the difference between the estimated channel and the actual channel during the uplink data transmission

$\boldsymbol{G}$ User-side Gram matrix

$\boldsymbol{H}_{dl}$ Downlink channel matrix during the downlink data transmission

$\boldsymbol{H}_{dl}$ Estimated downlink channel matrix between the BS and the users

$\boldsymbol{H}_{ul}$ Uplink channel matrix during the uplink data transmission

$\boldsymbol{H}_{ul}$ Estimated uplink channel matrix between the users and the BS

$\boldsymbol{I}$ Identity matrix

$\boldsymbol{P}$ MIMO precoding matrix

$\boldsymbol{U}$ Normalised unitary matrix

$\boldsymbol{W}$ MIMO decoding matrix

$\boldsymbol{s}$ Downlink transmitted symbol vector

$\boldsymbol{x}$ Uplink transmitted symbol vector

ξ_i ith eigenvalue of $\boldsymbol{H}\boldsymbol{H}^H$

ζ Estimated error caused by inaccurate CSI

c Speed of light (299,792,458 m/s)

$det(\cdot)$ Matrix determinant

f Frequency (Hz)

f_c Carrier frequency (Hz)

CHAPTER 1

INTRODUCTION

The work presented in this thesis is a part of the ongoing research within the Communication Systems & Networks (CSN) group at the University of Bristol in the field of fifth generation mobile system (5G) wireless communication technologies. The author's unique contributions to each chapter are clearly stated on each of the first pages. The contents of this chapter is summarized as follows:

- Summary of the background and the motivation behind the work of this thesis.
- Overview of massive MIMO technology in the concept of wireless communications.
- Highlighting the author's main contributions to the state of the art technology.
- Explaining the structure of this thesis.

Our use and reliance on Smartphone technology for services beyond voice and basic data communications is now so evident in both our business and personal lives. Smartphones are being used for various services such as downloading music or video clips, using digital maps, shopping online, browsing the internet, etc. Now it is easier than any time before for families and friends in different continents to video-stream at almost anytime and anywhere using smartphones. It's being used at some universities and learning institutions between the students and the lecturer to increase the class efficiency through a real-time interaction and feedback. It is also an easy method to share accidents related to crime and document any evidence just by using a smartphone's camera and a wireless network.

In addition to personal use, industries are exploiting wireless technology to increase the flexibility and the productivity of their work. For example, the BBC in moving towards the all wireless studio and using more high-definition (HD) wireless cameras at major cultural or sporting events. New promising products and applications are heavily based on the wireless technology. Drones technology with built-in light emitting diode (LED) lights has already started to replace the fireworks in many festivals, concerts and recently in the Winter Olympics held in South Korea [1]. The army of drones covered in LED lights are controlled via a secure and a reliable wireless technology. Autonomous Driving (AD) is one of the sensitive technology which required a truly remarkable engineering work towards establishing reliable channels with a very low latency links for vehicle-to-infrastructure (V2I) and vehicle-to-vehicle (V2V) [2]. Other applications such as machine-to-machine (M2M), internet of things (IoT) and delivering high bandwidth (BW) to trains among other promising technologies are also utilizing the benefits of wireless networks [3–5]. Furthermore, Smart cities are becoming more than a trend as several cities around the world are digitally transforming such as Bristol in the United Kingdom, New York in the United States of America and Dubai in United Arab Emirates. Managing the wireless radio resources plays a significant role in creating an efficient and a reliable smart city platform.

Various challenges have been addressed through the evolution of mobile wireless communication networks to achieve different goals. The first generation mobile system (1G) dealt with the challenge of providing voice calls through a wireless network by using an analogue signals. Sending text messages was supported by using the digital technology in the second generation mobile system (2G). Supporting data transmission with high data rate was started in the third generation mobile system (3G) and enhanced in the fourth generation mobile system (4G) [6]. The ongoing work towards 5G focuses on different kinds of challenges to support the new demands of future applications. The existing paradigms for exploiting the wireless resources won't be able to support the 1000-fold increase in capacity requirements forecast for 2020 [7] and the key performance indicator (KPI) targets for 5G networks have been set accordingly [8, 9].

The motivation behind investigating the massive MIMO (Ma-MIMO) technology to increase the spectral efficiency (SE) is outlined in the rest of this chapter.

Table 1.1: An overview of frequency assignment for the sub-6 GHz.

Wireless Access Technology	**BW**	**Frequency Range**
802.11b/g/n	20–40 MHz	2.4–2.5 GHz
802.11ac/n	20–160 MHz	5.1–5.9 GHz
GSM	9.6–59.6 MHz	380 MHz to 1.9 GHz
UMTS FDD	5 MHz	700 MHz to 3.5 GHz
LTE	1.4–20 MHz	450 MHz to 5.9 GHz

1.1 The Capacity Crunch of the Low Frequency Bands (sub-6GHz)

The radio spectrum range between 380MHz and 6GHz is being used by many wireless technologies, where the number of customers is increased dramatically. Given the favourable propagation for cellular communications, wireless local area networking (Wi-Fi), terrestrial television broadcasting and radar, this spectral sweet-spot is extremely crowded and mechanisms to enhance the spectrum efficiency are thus needed [10]. Table 1.1 shows the frequency range for main cellular services such as long-term evolution (LTE), Universal Mobile Telecommunications System (UMTS) and Global System for Mobile Communications (GSM) [11–13]. It also shows the short-range fixed access services such as 802.11 [14]. In communications system, path loss is increased by using higher carrier frequencies due to the electrical scaling of the antenna aperture. This is known as the Friis Transmission formula which is expressed mathematically as follows:

$$\rho_R = \frac{\rho G_T G_R c^2}{(4\pi R f)^2} \tag{1.1}$$

where ρ and ρ_R are the transmitted power and the received power, respectively. While G_T and G_R are the transmit antenna gain and the receive antenna gain, respectively. f is the frequency and c is the speed of light. The distance between transmit and received antennas is denoted by R. Furthermore, higher frequencies have challenging propagation properties [15], highly effected by the phase noise [15] and associated with technical challenges in designing the hardware components [16]. The aforementioned challenges have led the majority of consumer wireless technologies to be more attracted to the lower frequencies. However, another kind of challenges comes with the sub-6 GHz such as larger size of antennas, limited bandwidth and congested spectrum.

Although 802.11ac and LTE have increased the capacity in the sub-6 GHz, the cost and the availability of radio spectrum are still need to be handled properly. The challenge for wireless system designers is what to do next.

Table 1.2: Advantages and disadvantages for sub-6 GHz and mmWave.

	Advantages	Disadvantages
sub-6 GHz	Favourable Propagation	Congested Spectrum Limited Bandwidth
mmWave	Large BW	Phase Noise Sensitivity to Doppler Lack of Reflected and Diffracted Signals

1.2 Use of Millimetre Wave

Another approach for addressing the capacity goals of 5G and beyond wireless communications is the use of millimetre wave (mmWave) [17]. The use of wideband channels is one of the key elements towards meeting the new capacity demands for 5G technology. The 5G New Radio specification is already using the high frequency bands to increase the capacity [18]. Up to 20 Gbits/s potential throughput was demonstrated by using a bandwidth of 2 GHz and a carrier frequency of 73 GHz [19]. 28 GHz mmWave technology was demonstrated in London by Samsung and Arqiva [20]. The world's first 5G high mmWave over-the-air (OTA) field trial was conducted by Huawei and Deutsche Telekom [21]. Different real-world environments were covered in this field trial using 73 GHz at the Deutsche Telekom campus in Germany. Adaptive beamforming and beam tracking techniques were used in multi-cell environments with different scenarios

The mmWave technology still needs the sub-6 GHz technology in urban areas to provide control and handover signalling between different small cells in the cellular networks. Although high data rate could be provided by the mmWave technology, it is still challenging to maintain a reliable data transmission due to the propagation properties of the high frequencies. Besides, line-of-sight (LOS) or strong reflected paths won't always be available in the city. Therefore, the need for squeezing the sub-6 GHz bands is crucial to accommodate the growing capacity demands and the new requirements for 5G technology. Table 1.2 shows a brief comparison between sub-6 GHz and mmWave.

1.3 Massive MIMO

Most of the radio resources are shared between several users by using different time slots, frequencies and codes. frequency-divison multiple access (FDMA) and time-division multiple access (TDMA) techniques are used to share the available radio resources in GSM. The code domain is an alternative approach that can be used to share the available radio resources, such as using the code-division multiple access (CDMA) in the UMTS. While orthogonal frequency division multiplexing (OFDM) and single-carrier frequency-division multiple access (SC-FDMA) are used in LTE by allocating users to resource blocks (RBs), which is a combination of time and

frequency domains.

To achieve the 5G requirements with the 1000-fold increase in capacity by 2020, a better approach for sharing the radio resources is needed. This increase now presents significant challenges for wireless system designers, where the radio spectrum in sub-6 GHz is highly congested as described in section 1.1. The success of multiple antenna signal processing has resulted in a technology shift to Ma-MIMO. This employs a large number of antennas at the base station and only a few at the user device. It is a transformative technology for increasing the SE, multiplex more simultaneous users within the same radio resource by means of spatial domain signal processing. This will enhance wireless access as well as enabling a multitude of new wireless applications and businesses. Ma-MIMO enables efficient utilization of the limited radio resources by providing significant capacity improvement by aggressively exploiting the spatial domain [22]. In mmWave, massive MIMO is used for beamforming array gain, where analogue phase control have been designed and studied for various applications. Only very recently digital beamforming is considered using MIMO techniques at mmWave frequencies, where adaptive control of the waveforms at each antenna is required [23].

The spatial multiplexing (SM) technique is one of the key elements behind improving the system capacity in LTE advance. A base station (BS) with eight antennas elements can spatial multiplexing up to eight users simultaneously [24]. By increasing the number of antenna elements at the BS, the transmitted signal can be directed more precisely towards the receiver. This decreases the inter-user interference (IUI), which improves the network capacity. The key aspects of the Ma-MIMO technology and its evolution from the basic MIMO system are covered in Chapter 2.

1.4 Summary of Contributions and Thesis Overview

The work in this thesis was started in 2015, when the concept of Ma-MIMO has been considered as a potential candidate for boosting the capacity in 5G. This thesis covers the journey of proofing the concept of Ma-MIMO, evaluating the practicality of using Ma-MIMO in real-world scenarios and identifying solutions to the operational deployments uncovered when using a 128 antenna Ma-MIMO system. This section presents a summary of contributions, publications and the thesis outline.

1.4.1 Summary of Contributions to the State of the Art

- Improving the University of Bristol Ma-MIMO testbed. It's the world's 1^{st} real-time 128-antenna Ma-MIMO testbed. The author has proposed, designed, built, and tested novel algorithms and methodologies to enhance its performance. Several contributions using field-programmable gate array (FPGA) implementations were made at the BS and the UEs for power control algorithms, OTA synchronisation (chapter 3), user grouping techniques

and error vector magnitude (EVM) estimations (chapter 5). In addition to these specific contributions, the author enabled controlling the switching mode between power amplifiers (PAs) and low-noise amplifiers (LNAs) based on the Ma-MIMO time division duplex (TDD) frame scheduled through General Purpose Input Output (GPIO) at the BS and the UEs sides.

- Demonstrating and evaluating the channel robustness in Ma-MIMO in different environments (chapter 3). Four measurement campaigns were conducted in indoor and outdoor environments. Static users and mobility scenarios were used. The measurement campaigns were conducted at the University of Bristol for the indoor environment with static users. While the mobility scenarios were conducted at Lund University. [1]

- Proposed and implemented a novel uplink closed loop power control scheme in a single cell for Ma-MIMO (chapter 3). The algorithm was evaluated through several indoor, outdoor and mobility Ma-MIMO measurements campaigns with real-time results.

- Introducing the challenges and the limiting factors when increasing the SE value (chapter 4).

- The author has bench-marked direct extraction from the physical implementation for realistic evaluation based on the EVM performance rather than relying on Shannon theoretic capacity (chapter 4).

- Showing that the inaccurate uplink (UL) channel state information (CSI) has greater impact on the downlink (DL) data transmission than it is on the UL data transmission due to the error amplification caused by the reciprocity calibration matrix (chapter 4).

- Shown through theory and practical evaluation that by using zero-forcing (ZF) or minimum mean square error (MMSE), a lower number of antennas at the BS with high hardware quality could be better than increasing the number of antennas and reducing the hardware quality (chapter 4).

- Introduced an estimation method with high accuracy between the EVM and the signal to interference plus noise ratio (SINR) values for massive MIMO with ZF and MMSE (chapter 5).

- Introduced an EVM prediction method for a subset of users taken from the original set of simultaneous users in a single cell Ma-MIMO (chapter 5).

- Novel adaptive user grouping algorithms for a single cell Ma-MIMO scenario are proposed and shown to further enhance performance (chapter 5). For the first time, the algorithms address the interference caused by the user channel vectors as well as hardware impairments.

[1] A video of the mobility measurement campaigns at Lund University is available at https://bit.ly/2Ayiikj.

Here, this is uniquely achieved by extracting the EVM, and three different methodologies are applied to address specific wireless connectivity objectives. Importantly, real-world experimental data-sets have been used to evaluate the proposed user grouping algorithms.

- The author co-led a measurement campaign at British Telecom (BT)'s R&D headquarters [25][2]. The aim of the campaign was to explore the potential of Ma-MIMO technology and to validate some off-line analysis based on data collected from previous measurement campaigns. It also helped the mobile operator to understand the realistic benefits, challenges and requirements for the Ma-MIMO technology. The measurement campaign was conducted by a researchers and engineers from University of Bristol, Lund University, National Instruments (NI) and BT. The measurement campaign is described in appendix C.

- The author led the Ma-MIMO team at the '5G Layered Realities Weekend' –Showcase in Bristol', successfully establishing twelve reliable spatial multiplexed video streams [26] (chapter 5). This was the world's first urban 5G showcase funded by the UK Government's Department of Digital, Culture, Media and Sport (DCMS)[3]. The author was responsible for enhancing the Ma-MIMO testbed performance to enable reliable videos streams from cameras for UL and DL data transmission. Several techniques and approaches were proposed and implemented by the author to enable this work. The 5G showcase is described further in chapter 5. In addition to the hardware and software modifications, the author was responsible for the planing and the deployment stages. The author led the Ma-MIMO team in an indoor pre-trial in Wills Memorial Building and an outdoor pre-trial in Bristol's Millennium Square. The purpose of these pre-trials is to evaluate all the modifications before the 5G showcase. The first pre-trial is described in chapter 3 and the second pre-trial in described in appendix D.

[2]A video of the measurement campaign at BT's R&D headquarters is available at https://bit.ly/2DMZQaV
[3]A video of the world's first urban 5G Showcase is available at https://www.youtube.com/watch?v=7Qzv_TtyKMU

1.4.2 Published Work in IEEE

The outcomes of the aforementioned contributions have been published through the following conference and journal papers:

- W. B. Hasan, P. Harris, A. Doufexi, and M. Beach, "Real-Time Maximum Spectral Efficiency for Massive MIMO and its Limits," *IEEE Access*, vol. 6, pp. 46122–46133, 2018
- W. B. Hasan, P. Harris, A. Doufexi, and M. Beach, "Impact of User Number on Massive MIMO with a Practical Number of Antennas," in *2018 IEEE 87th Vehicular Technology Conference (VTC Spring)*, pp. 1–5, June 2018
- W. B. Hasan, P. Harris, A. Doufexi, and M. Beach, "Spatial Uplink Power Control for Massive MIMO," in *2017 IEEE 85th Vehicular Technology Conference (VTC Spring)*, pp. 1–6, June 2017
- P. Harris, W. B. Hasan, L. Liu, S. Malkowsky, M. Beach, S. Armour, F. Tufvesson, and O. Edfors, "Achievable Rates and Training Overheads for a Measured LOS Massive MIMO Channel," *IEEE Wireless Communications Letters*, vol. 7, pp. 594–597, Aug 2018
- P. Harris, W. B. Hasan, S. Malkowsky, J. Vieira, S. Zhang, M. Beach, L. Liu, E. Mellios, A. Nix, S. Armour, A. Doufexi, K. Nieman, and N. Kundargi, "Serving 22 Users in Real-Time with a 128-Antenna Massive MIMO Testbed," in *2016 IEEE International Workshop on Signal Processing Systems (SiPS)*, pp. 266–272, Oct 2016
- P. Harris, W. B. Hasan, H. Brice, B. Chitambira, M. Beach, E. Mellios, A. Nix, S. Armour, and A. Doufexi, "An overview of massive MIMO research at the University of Bristol," in *Radio Propagation and Technologies for 5G (2016)*, pp. 1–5, Oct 2016
- P. Harris, S. Malkowsky, J. Vieira, F. Tufvesson, W. B. Hasan, L. Liu, M. Beach, S. Armour, and O. Edfors, "Temporal Analysis of Measured LOS Massive MIMO Channels with Mobility," in *2017 IEEE 85th Vehicular Technology Conference (VTC Spring)*, pp. 1–5, June 2017
- P. Harris, S. Malkowsky, J. Vieira, F. Tufvesson, W. B. Hasan, L. Liu, M. Beach, S. Armour, and O. Edfors, "Performance Characterization of a Real-Time Massive MIMO System Mobile Channelswith LOS ," *IEEE Journal on Selected Areas in Communications*, 2017

1.4.3 Submitted Publication to IEEE

The following work has been submitted for publication:

- W. B. Hasan, P. Harris, H. Bromell, A. Doufexi, and M. Beach, "Adaptive User Grouping Based on EVM Prediction for Efficient &Robust Massive MIMO in TDD," *IEEE Transactions on Vehicular Technology*, 2018

1.4.4 Contributions to European Cooperation in Science & Technology (COST)

Besides publishing journal and conference papers with Institute of Electrical and Electronics Engineers (IEEE), the author has contributed to several technical meetings with European Cooperation in Science & Technology (COST) through the following papers:

- W. B. Hasan, P. Harris, A. Doufexi, and M. Beach, "User Grouping for Massive MIMO in TDD." TD(17)03069, February 2017
- W. B. Hasan, P. Harris, A. Doufexi, and M. Beach, "Preliminary Investigation of Uplink Power Control for Massive MIMO." TD(16)01084, June 2016
- P. Harris, S. Malkowsky, J. Vieira, F. Tufvesson, W. B. Hasan, L. Liu, M. Beach, S. Armour, and O. Edfors, "Temporal Analysis of Measured LOS Massive MIMO Channels with Mobility." TD(17)03043, February 2017
- P. Harris, W. B. Hasan, H. Brice, M. Beach, E. Mellios, A. Nix, S. Armour, and A. Doufexi, "Massive MIMO Mobility Measurements in LOS with Power Control." TD(16)02031, Oct 2016

1.4.5 Further Contributions

In addition to the aforementioned contributions, the author was invited as a speaker to the Testbed Design and Prototyping event at Toshiba Research Europe Limited [4], CommNet Winter School at BT's R&D in Ipswich and NI 5G event hosted by University of Cambridge. He was also invited as a speaker to private RF Round Table events led by NI in Leuven, Belgium; Sydney, Australia and Bristol, UK. Finally, the author's work has jointly received the 2017 Collaborate to Innovate (C2I) Award [5]

- U. of Bristol, L. University, N. Instruments, and B. Telecom, "Collaborate 2 Innovate: Information, Data & Connectivity Category." The Engineer, September 2017 [6]

and has honorary mentioned in the 2016 IEEE ComSoc Student Competition [7]

- P. Harris, S. Malkowsky, J. Vieira, and W. B. Hasan, "Communications Technology Changing the World." IEEE Communications Society, November 2016.

  Honorary Certificate of Appreciation

[4] Toshiba Research Europe 'Testbed Design and Prototyping' available at http://www.scavenge.eu/training/_4/
[5] The 2017 Collaborate to Innovate (C2I) Award available at https://www.theengineer.co.uk/c2i-2017-winners-announced/
[6] C2I Award also available at http://www.bristol.ac.uk/news/2017/september/massive-mimo.html
[7] The 2016 IEEE ComSoc Student Competition available at https://www.comsoc.org/education-training/student-competition/student-competition-winners

1.4.6 Thesis Outline

The remaining chapters of the thesis are as follows. Chapter 2 provides a background and a literature review for Ma-MIMO. It covers the main advantages and challenges in using Ma-MIMO. In Chapter 3, The University of Bristol Ma-MIMO testbed is introduced and real-time results from several experimental campaigns are presented. Chapter 4 evaluates the impact of spatially multiplexing and increasing the number of users within a single-cell Ma-MIMO system. It covers the per-cell SE of 145.6 bits/s/Hz achieved with a 128-antenna Ma-MIMO testbed and introduces the challenges and the limiting factors when increasing the SE value. Chapter 5 introduces novel user grouping algorithms to further enhance the Ma-MIMO advantages for different applications. It also presents an estimation method between the EVM and the SINR and introduces an EVM prediction method for a single cell Ma-MIMO.The first urban 5G showcase in covered in this chapter as well. Lastly, Chapter 6 presents the conclusions and the recommendations from this work.

CHAPTER 2

BACKGROUND AND THEORY UNDERPINNING MASSIVE MIMO

This chapter covers the evolution of Ma-MIMO and provides the underpinning literature review for the key aspects of this technology. The following summarize the contents of this chapter:

- An overview of MIMO architectures, signal processing and the evolution towards multi-user (MU)-MIMO ending up by Ma-MIMO.
- Illustrating the differences between analog beamforming and digital beamforming in the context of Ma-MIMO.
- Presenting the main advantages and challenges when deploying Ma-MIMO.
- Presenting some of the existing Ma-MIMO testbeds and highlighting their results.
- Presenting the 3rd Generation Partnership Project (3GPP) definition of Ma-MIMO and the relationship that this has with this PhD thesis.

2.1 MIMO Review

The early research of MIMO can be tracked back to 1970, where the concept of MIMO was introduced to deal with mutual interference without exploiting the multipath environment [42]. Practical solutions for MIMO using OFDM were introduced in [43], where the nature of the multipath propagation was exploited. Although real-time results were achieved in 1998 by Clarity Wireless [44] and Bell Labs [45], the first MIMO-OFDM was commercially released in 2004 by Airgo Networks for wireless local area network (LAN). The significant throughput improvement enabled new kind of applications. Since then, MIMO has been playing a major role in improving the link reliability and increasing the data rate [46]. Examples of Wi-Fi access point and cellular BS using the MIMO technology are shown in Figure 2.1.

Although the theoretical concept of MIMO can be applied to any wireless system, the industry usually pairs it with the OFDM thus implicitly providing channel equalisation. Figure 2.3 shows a narrowband UL MIMO system model with a number of transmit antennas N_T and a number of receive antennas N_R. The received signal $\boldsymbol{y}$ between two multi-antenna devices is commonly expressed in a $1 \times N_R$ column vector as follows:

$$\boldsymbol{y} = \sqrt{\rho}\boldsymbol{x}\boldsymbol{H} + \boldsymbol{n} \tag{2.1}$$

where $\boldsymbol{x}$ is the $1 \times N_T$ transmitted symbol column vector and $\boldsymbol{H}$ is the normalised $N_T \times N_R$ frequency domain channel matrix. The transmit power and the $1 \times M$ additive white gaussian noise (AWGN) vector are denoted by ρ and $\boldsymbol{n}$ respectively.

Decoding and precoding techniques are used to separate the transmitted data stream in MIMO. For a successful separation, the channel matrix $\boldsymbol{H}$ should be known at the transmitter, receiver or both sides. The CSI can only be known at the receiver or it can be fed back to the transmitter, which are described as open-loop and closed-loop respectively. An example of the open-loop method is the Bell Laboratories Layered Space-Time (BLAST) architectures [47] and the common linear signal detection techniques, such as matched filtering (MF), ZF and MMSE [48]. Whilst, the most common and practical closed-loop method is the eigenbeamforming technique [49].

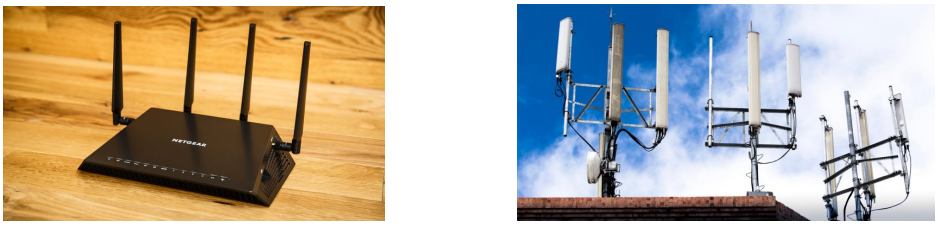

Figure 2.1: Examples of wireless communications using MIMO technology which can be seen everyday. Wireless router on the left and BS tower on the right.

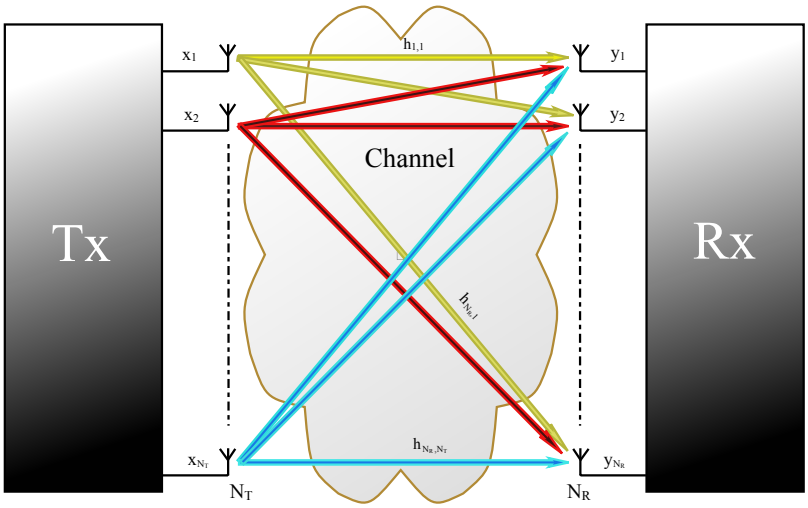

Figure 2.2: Generic Uplink MIMO System Model

Generally, MIMO can be divided into three categories: single-user (SU)-MIMO, MU-MIMO and Ma-MIMO. Several techniques such as space-time coding, beamforming and spatial multiplexing of data streams were used in SU-MIMO. These techniques improved the system performance in the 3G and 4G networks. Despite the huge benefits from each technique, they can't be fully used at the same time. A trade-off between spatial diversity and multiplexing schemes should always be considered in SU-MIMO such as the adaptive switching method used in LTE [50].

2.1.1 Multi-user MIMO System

MU-MIMO was developed to enhance MIMO system by exploiting the spatial multiplexing gain. It has been added to the 3GPP standards, the Worldwide Interoperability for Microwave Access (WiMAX) standards and the Wi-Fi standards since LTE Rel 8, 802.16m and 802.11ac respectively [51–53]. Here, K single-antenna users can be spatially multiplexed by M antennas at the BS, as shown in Figure 2.3, where $K \leq M$ in general [54] and $M \leq 8$ in LTE [55]. The unique spatial signature for each user allows simultaneous communications between all users and the BS by spatially sharing the wireless channel. However, the channel knowledge is more crucial compared to SU-MIMO since it is required in signal processing to suppress the IUI. Unlike the situation with SU-MIMO, joint encoding and detection among users are not needed with MU-MIMO and each user is unaware of the full CSI. The BS has full access to the CSI and handles the additional signal processing complexity. In UL data transmission, it detects the UL symbols by decoding the received signal. While in DL data transmission, it precodes the DL symbols so that no additional signal processing is required at the user side. Sections 2.2.3 and 2.2.4 covers the decoding and the precoding techniques used in MU-MIMO and Ma-MIMO, since Ma-MIMO has evolved from MU-MIMO.

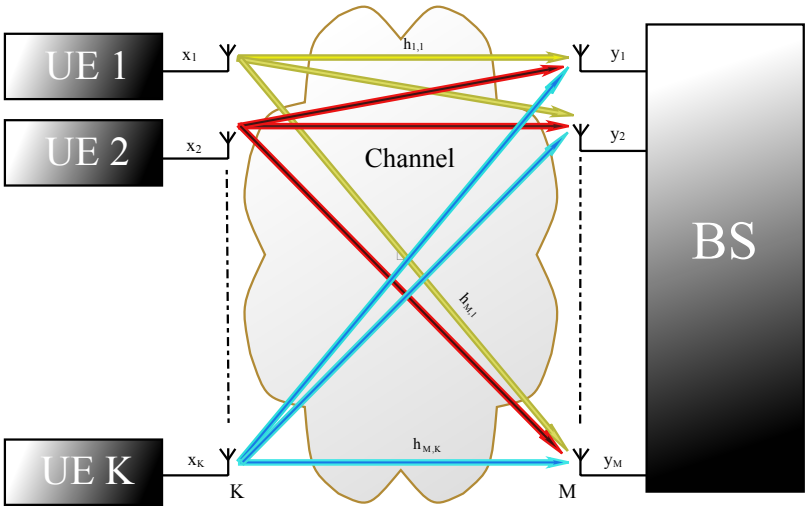

Figure 2.3: Generic Uplink MU-MIMO System Model

2.1.2 Channel Capacity in MIMO System

The achievable SE for a symmetrical MIMO system is shown in equation 2.2,where $N_R = N_T$ [49].

$$C_{MIMO} = \log_2 \left| \boldsymbol{I}_{N_T} + \frac{\rho}{N_T} \boldsymbol{H}\boldsymbol{H}^H \right| \text{bits/s/Hz} \tag{2.2}$$

where $\boldsymbol{I}_{N_T}$ is the $N_T \times N_T$ identity matrix. The Gramian matrix $\boldsymbol{H}\boldsymbol{H}^H$ can be rewritten using the eigenvalue decomposition as

$$\boldsymbol{H}\boldsymbol{H}^H = \boldsymbol{U}\boldsymbol{D}\boldsymbol{U}^H \tag{2.3}$$

where $\boldsymbol{D}$ is the diagonal matrix of N_T eigenvalues $\sigma_i^2 (i = 1...N_T)$ and $\boldsymbol{U}$ is a normalised unitary matrix. The rank of the channel matrix, R, is determined by the number of non-zero eigenvalues. This indicates the dimensions of the square matrices that form a linearly independent set. From equation 2.3 and 2.2, the achievable SE can be rewritten as shown in equation 2.4.

$$\begin{aligned}
C_{MIMO} &= \log_2 \left| \boldsymbol{I}_{N_T} + \frac{\rho}{N_T} \boldsymbol{U}\boldsymbol{D}\boldsymbol{U}^H \right| \\
&= \log_2 \left| \boldsymbol{U} \left(\boldsymbol{I}_{N_T} + \frac{\rho}{N_T} \boldsymbol{D} \right) \boldsymbol{U}^H \right| \\
&= \log_2 \left[|\boldsymbol{U}| \cdot \left| \boldsymbol{I}_{N_T} + \frac{\rho}{N_T} \boldsymbol{D} \right| \cdot \left| \boldsymbol{U}^H \right| \right] \\
&= \log_2 \left| \boldsymbol{I}_{N_T} + \frac{\rho}{N_T} \boldsymbol{D} \right| \\
&= \log_2 \left[\prod_{i=1}^{R} \left(1 + \frac{\rho}{N_T} \sigma_i^2 \right) \right] \\
&= \sum_{i=1}^{R} \log_2 \left(1 + \frac{\rho}{N_T} \sigma_i^2 \right) \text{bits/s/Hz}
\end{aligned} \tag{2.4}$$

The above equation shows that the capacity of R single-input single-output (SISO) channels, where each channel i has gain σ_i^2, and the MIMO channel capacity are equivalent. The transmitter can split the total power equally between all antennas if it has no access to the CSI. The optimum distribution of channel eigenvalues needs to be considered in some scenarios. For example, in a full rank channel matrix with only one non small eigenvalue, the low gains prevent from having useful spatial modes and only one is likely to be established. The sum of all eigenvalues for a fixed channel matrix can be expressed as follows:

$$\Xi \equiv \sum_{i=1}^{R} \xi_i = \|\boldsymbol{H}\|_F^2 \tag{2.5}$$

The above equation is derived from the definition of trace and Frobenius norm. With a full rank MIMO channel and equal eigenvalues such that $\xi = \frac{\Xi}{R}$, the capacity in equation 2.4 can be rewritten as follows:

$$\begin{aligned} C_{MIMO} &= \sum_{i=1}^{R} \log_2\left(1 + \frac{\rho}{R}\xi_i\right) \\ &= \sum_{i=1}^{R} \log_2\left(1 + \frac{\rho\Xi}{R^2}\right) \\ &= R\log_2\left(1 + \frac{\rho\Xi}{R^2}\right) \text{bits/s/Hz} \end{aligned} \tag{2.6}$$

By normalising the channel matrix such that $\mathbb{E}\{\|\boldsymbol{H}\|_F^2\} = R^2$, the MIMO channel capacity with no CSI can be represented as follows:

$$C_{MIMO} = R\log_2\left(1 + \rho\right) \text{bits/s/Hz} \tag{2.7}$$

In a real environment, a water-filling algorithm is used for eigenbeamforming and optimum power allocation. The water-filling power allocation maximises the capacity by appropriately distributing the transmit power. This approach handles the commonly situation where some spatial modes have better gains than others [49]. By replacing R with K, the above expressions cover the MU-MIMO configuration. The water-filling algorithm is mostly inconvenient for MU-MIMO since it requires a full access to CSI at the transmitter and receiver sides.

2.2 Massive MIMO System

The capacity improvements achieved by MU-MIMO played a major role in proposing Ma-MIMO as an evolution of its concept by increasing number of antenna elements M at the BS [22]. Massive MIMO is a MU-MIMO architecture with a large number of antennas at the BS serving several users within the same time and frequency. The ratio between M and the number of simultaneous users served by one BS is still not agreed on. However, it was agreed that M is far outweigh the number of simultaneous users. The theoretical concept of Ma-MIMO equipped the

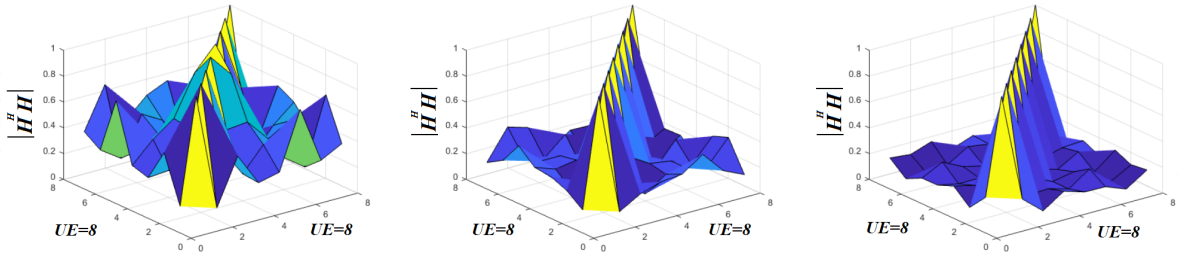

Figure 2.4: Normalised user-side Gramian matrix elements $\left|\boldsymbol{H}^H\boldsymbol{H}/M\right|$ for 8 users ($K = 8$) served by 8, 32 and 128 BS antennas (left to right). IID Rayleigh channels were used here.

BS with hundreds to infinity of antenna elements [56]. While from the 3GPP point of view, 16, 32 and 32+ antenna elements have been proposed so far as described in section 2.2.2.

The large number of antennas at the BS affects the MIMO channel by causing a very slow growth in the variance of mutual information compared to its mean. As a result, the off-diagonal values of the Gramian matrix become increasingly weaker compared to the diagonal value. This phenomenon is called channel hardening and becomes more prominent as the number of antennas is increased [57]. Figure 2.4 shows the effect of increasing number of BS antennas using independent and indentically distributed (IID) channels. This can be explained by the strong law of large numbers applied in equation 2.8 , which yields perfect and deterministic orthogonality when all entries are IID Gaussian [58]. The Ma-MIMO degrees of freedom could improve the MU-MIMO performance used in LTE.

$$\lim_{M\to\inf} \boldsymbol{H}\boldsymbol{H}^H \to M\boldsymbol{I} \tag{2.8}$$

It is shown in [59] that the effects of hardware impairments, small scale fading and noise could also be averaged out by the law of large numbers. This could decrease the latency, increase the SE and improve the link reliability, which enables Ma-MIMO to achieve the main physical layer requirements for 5G.

2.2.1 Analog Beamforming vs Digital Beamforming

The work in [22], by Dr. Thomas L.Marzetta, formulates the massive MIMO concept. The original idea was to exploit the scattering richness of the wireless environment caused by the very large number of BS antennas in a MU-MIMO system, which is named later a Ma-MIMO. By using the simple digital signal processing technique MF, a huge SE can be achieved. Different signals are digitally designed for each antenna element at the BS side to spatially multiplexing several data streams by transmitting superposition of the signals with separate directions. These superpositioned signals are then coherently combined at the user side. The aforementioned technique is commonly known as digital beamforming, where the amplitude/phase weights are

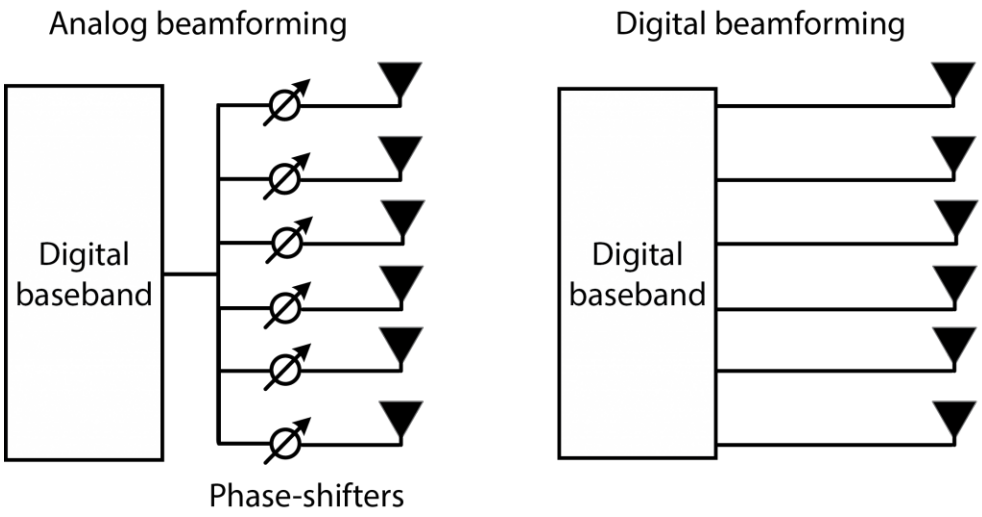

Figure 2.5: Left: analog beamforming. Right: digital beamforming

applied before the digital-to-analogue converter (DAC) in DL and after the analogue-to-digital converter (ADC) & digital down converter (DDC) in UL [60]. The number of transceivers required at the BS side for this technique is equal to the number of antennas, as shown in Figure 2.5 right.

An alternative method for exploiting the spatial domain was introduced to decrease the implementation cost in Ma-MIMO. Analog beamforming was proposed to be used instead of digital beamforming. The same signal is transmitted from several antennas with different phases by using the phase shifters, as shown in Figure 2.5 left. The amplitude/phase weights are applied to the analog signals in the transmission stage and summed up before the ADC in the reception stage. Therefore, only one transceiver unit is required with the analog beamfroming. Although the cost is reduced, the effectiveness of using analog beamforming is debatable in terms of capacity and the flexibility improvements for Ma-MIMO compared to the digital beamforming method.

The work in this thesis has adopted the original Ma-MIMO approach, where the digital beamforming is applied for below 6 GHz.

2.2.2 Ma-MIMO in 3GPP

In spite of the huge capacity improvements Ma-MIMO can offer, there are significant challenges for a successful commercialization. The cost and the power consumption are key factors for designing the BS. Active antenna technology is required in Ma-MIMO, which is becoming technically and commercially feasible. Therefore, the discussion of Ma-MIMO was started in 3GPP, where a two dimensional (2D) array structure was adopted in Release 13. This allows the BS to control the wireless signals in elevation and azimuth dimension. It was officially named full dimension MIMO (FD-MIMO) in Release 13 and a new reference signal (RS) was introduced called beamformed channel state information RS (CSI-RS) [61]. In addition to the beamformed CSI-RS, the non-precoding CSI-RS is supported by the FD-MIMO. A hardware distribution

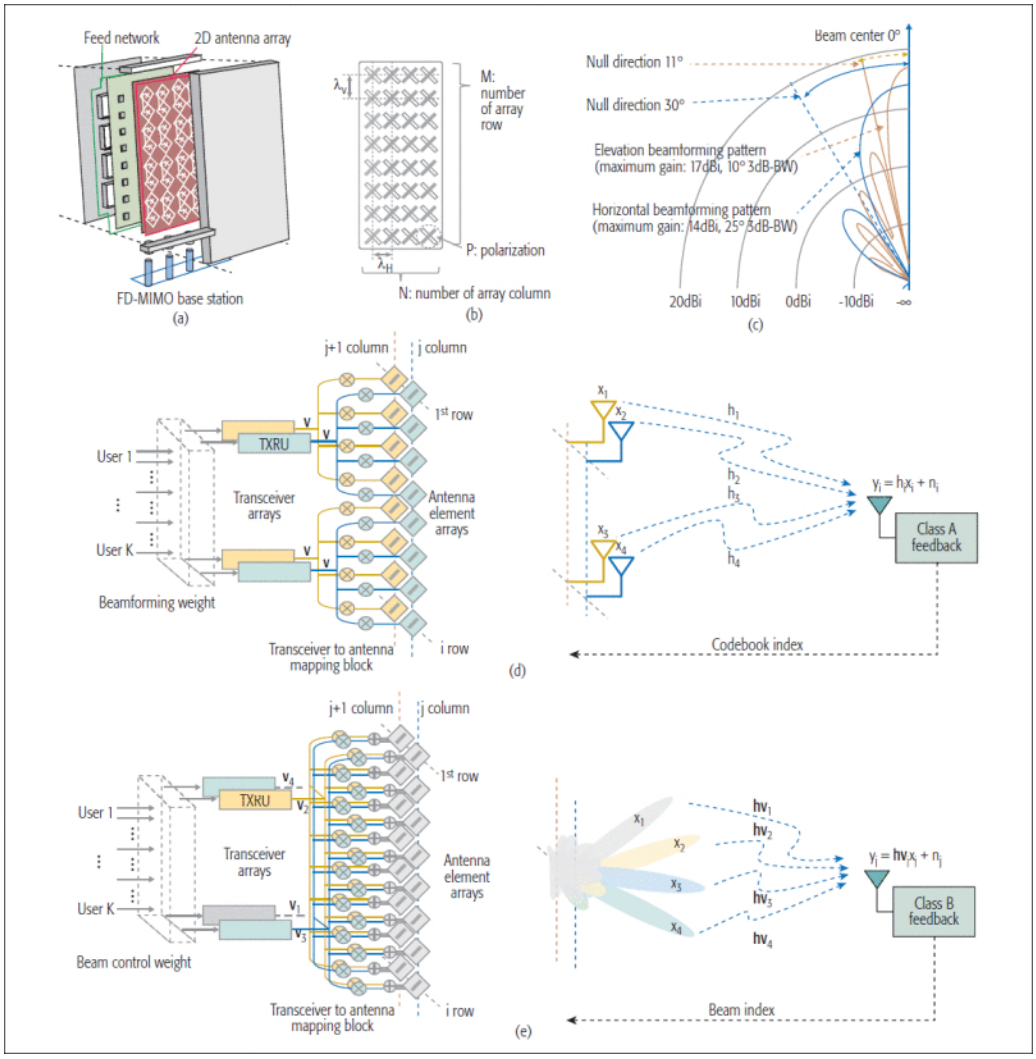

Figure 2.6: The 3GPP prospective for Ma-MIMO (FD-MIMO) [61].

structure between the baseband and the antenna array was proposed to enable both CSI-RS techniques. This hardware architecture known as transceiver unit (TXRU), which can be seen in Figure 2.6 (a). It provides the flexibility of controlling the signal's phase and gain in the digital and the analog domains, which is also known as hybrid beamforming.

For the non-precoded CSI-RS, the antenna array is divided to several groups as shown in Figure 2.6 (d). Each TXRU is connected to one of the groups. The user monitors the non-precoded CSI-RS transmitted from each of the groups, then feeds back two codebooks to the BS (vertical and horizontal channel information). This enables the user to adopt the channel variation. For the beamformed CSI-RS, the radio frequency (RF) signals from a group of TXRUs are connected to a single antenna. RF combining circuits are needed as shown in Figure 2.6 (c). The BS transmits several beamformed CSI-RS. The user selects the preferred beam after a scanning process. The beam index is sent back to the BS, which then select that beam for the data transmission.

Table 2.1: Massive MIMO in the 3GPP

Release number	**# of Antennas**
13	16
14	32
15+	32+

In DL, M resources are required for the non-precoding CSI-RS. While the required resources for the beamformed CSI-RS scales linearly with the number of beams. In UL, the feedback overhead depends on the codebock resolution and M when the non-precoding CSI-RS is used. While it only depends on the number of beams, when the beamformed CSI-RS is used. Therefore, the beamformed CSI-RS is more suitable for large number of antennas. Table 2.1 shows how the number of antennas at the BS was increased based on the 3GPP releases [62].

All the conducted works in this thesis are based on a fully digital system and follows the original concept of Ma-MIMO that was introduced in [22]. Although the 3GPP has not yet adopted this approach, it is still being considered for boosting the wireless capacity.

2.2.3 Linear Decoding Techniques

In a single-cell Ma-MIMO architecture, simple linear detectors and precoders become close to optimal due to the channel hardening effect [63]. Non-linear techniques could be optimal such as dirty paper coding (DPC) in DL and successive interference cancellation (SIC) UL, but the implementation require significant additional complexity [63, 64]. For brevity, only the common linear detection techniques, MF, ZF and MMSE, are outlined in this section.

In UL data transmission, linear decoders can be used to recover the original transmitted signal from equation 2.1. The equalized UL signal $\hat{\boldsymbol{x}} \in \mathbb{C}^{\mathbb{K}}$ can be expressed as

$$\hat{\boldsymbol{x}} = \boldsymbol{W}\left(\sqrt{\rho_{ul}}\boldsymbol{H}\boldsymbol{x} + \boldsymbol{n}_{BS}\right) \tag{2.9}$$

where $\boldsymbol{W} \in \mathbb{C}^{K \times M}$is the linear decoder matrix and ρ_{ul} is the corresponding UL transmit power. The additive noise vector in UL is denoted by $\boldsymbol{n}_{BS}$, where $\sigma^2_{n_{BS}}$ is the noise variance.

2.2.3.1 Matched Filtering

MF is a low complexity operation where the decoder used in the equalization process can be written as $\boldsymbol{W} = \boldsymbol{H}^H$. It is also known as maximal ratio combining (MRC) and maximal ratio transmission (MRT) for UL and DL scenarios, respectively. The decoder doesn't consider the

mutual interference between users and only maximises the user signal to noise ratio (SNR). By using MF, the equalized UL signal in equation 2.9 can be rewritten as

$$\hat{\boldsymbol{x}} = \sqrt{\rho_{ul}}\boldsymbol{H}^H\boldsymbol{H}\boldsymbol{x} + \boldsymbol{H}^H\boldsymbol{n}_{BS} \tag{2.10}$$

and the received symbol from user k can be expressed as shown in equation 2.11

$$\hat{x}_k = \underbrace{\sqrt{\rho_{ul}}\boldsymbol{h}_k^H\boldsymbol{h}_k x_k}_{\text{Desired Signal}} + \overbrace{\sqrt{\rho_{ul}}\sum_{i\neq k}^{K}\boldsymbol{h}_k^H\boldsymbol{h}_i x_i}^{\text{IUI}} + \underbrace{\boldsymbol{h}_k^H\boldsymbol{n}_{BS}}_{\text{Noise}} \tag{2.11}$$

The above equation shows that the received symbol from user k is affected by the IUI from $K-1$ users and the AWGN noise. In theory, MF is a perfect decoder for Ma-MIMO when number of antennas at the BS tends to infinity as the IUI is removed due to the low of large number shown in equation 2.8. Thus, there is no need for complex decoders such as ZF and MMSE, where the matrix inversion process is required. Besides, it is more more convenient for distributed Ma-MIMO [65]. However, increasing number of antennas at the BS is challenging due to hardware complexity and deployment difficulties [66]. As a results, more complex decoders could be needed to mitigate the impact of IUI.

2.2.3.2 Zero Forcing

This technique is also known as the channel inversion, which attempts to remove the interference between users [67]. With perfect CSI, ZF nulls out the IUI by multiplying the received signal with Moore-Penrose pseudoinverse of the channel, denoted as $\boldsymbol{H}^{\dagger}$. The ZF decoding matrix is shown in equation 2.12

$$\boldsymbol{W} = \left(\boldsymbol{H}^H\boldsymbol{H}\right)^{-1}\boldsymbol{H}^H \tag{2.12}$$

By using ZF, the equalized UL signal in equation 2.9 can be rewritten as

$$\begin{aligned}\hat{\boldsymbol{x}} &= \sqrt{\rho_{ul}}\left(\boldsymbol{H}^H\boldsymbol{H}\right)^{-1}\boldsymbol{H}^H\boldsymbol{H}\boldsymbol{x} + \left(\boldsymbol{H}^H\boldsymbol{H}\right)^{-1}\boldsymbol{H}^H\boldsymbol{n}_{BS}\\ \hat{\boldsymbol{x}} &= \sqrt{\rho_{ul}}\boldsymbol{x} + \left(\boldsymbol{H}^H\boldsymbol{H}\right)^{-1}\boldsymbol{H}^H\boldsymbol{n}_{BS}\end{aligned} \tag{2.13}$$

and the received symbol from user k can be expressed as shown in equation 2.14

$$\hat{x}_k = \underbrace{\sqrt{\rho_{ul}}\left(\boldsymbol{h}_k^H\boldsymbol{h}_k\right)^{-1}\boldsymbol{h}_k^H\boldsymbol{h}_k x_k}_{\text{Desired Signal}} + \underbrace{\left(\boldsymbol{h}_k^H\boldsymbol{h}_k\right)^{-1}\boldsymbol{h}_k^H\boldsymbol{n}_{BS}}_{\text{Noise}} \tag{2.14}$$

The ZF deecoding matrix does not consider the noise effect which might result a significant noise amplification. Thus, the system performs poorly in a noisy channel. If $\boldsymbol{z} = \left(\boldsymbol{H}^H\boldsymbol{H}\right)^{-1}\boldsymbol{H}^H\boldsymbol{n}_{BS}$, it is shown in [49] that the total noise power $P_{\boldsymbol{z}}$ can be written as the following:

$$P_{\boldsymbol{z}} = MT_r\left[\left(\boldsymbol{H}^H\boldsymbol{H}\right)^{-1}\right]\sigma^2_{n_{BS}} \tag{2.15}$$

The above equation shows that the trace of the term $\left(\boldsymbol{H}^H\boldsymbol{H}\right)^{-1}$ and the number of antenna elements at the BS M have the effect of increasing the total noise power. The noise amplification could be dealt with by increasing the transmission power, which does not always reflect well on the system.

2.2.3.3 Minimum Mean Square Error

This technique is also known as regularized channel inversion, which intends to mitigate the IUI and to increase the SNR when it is needed [67]. So it is a trade-off between interference reduction and signal strength, which are achieved by ZF and MF decoders, respectively. MMSE decoder is obtained by minimising the mean square error (MSE) between the received and the transmitted signal

$$\min_{\boldsymbol{W}} \mathbb{E}\left[|\boldsymbol{x} - \boldsymbol{W}\boldsymbol{y}|^2\right] \tag{2.16}$$

and the solution is optimised in equation 2.17, where γ is the SNR

$$\boldsymbol{W} = \left(\boldsymbol{H}^H\boldsymbol{H} + \frac{1}{\gamma}\boldsymbol{I}\right)^{-1}\boldsymbol{H}^H \tag{2.17}$$

shown in [58]. By using MMSE, the equalized UL signal in equation 2.9 can be rewritten as

$$\hat{\boldsymbol{x}} = \sqrt{\rho_{ul}}\left(\boldsymbol{H}^H\boldsymbol{H} + \frac{1}{\gamma}\boldsymbol{I}\right)^{-1}\boldsymbol{H}^H\boldsymbol{H}\boldsymbol{x} + \left(\boldsymbol{H}^H\boldsymbol{H} + \frac{1}{\gamma}\boldsymbol{I}\right)^{-1}\boldsymbol{H}^H\boldsymbol{n}_{BS} \tag{2.18}$$

and the received symbol from user k can be expressed as shown in equation 2.19

$$\hat{x}_k = \underbrace{\sqrt{\rho_{ul}}\left(\boldsymbol{h}_k^H\boldsymbol{h}_k + \frac{1}{\gamma}\boldsymbol{I}\right)^{-1}\boldsymbol{h}_k^H\boldsymbol{h}_k x_k}_{\text{Desired Signal}} + \overbrace{\sqrt{\rho_{ul}}\sum_{i\neq k}^{K}\left(\boldsymbol{h}_k^H\boldsymbol{h}_k + \frac{1}{\gamma}\boldsymbol{I}\right)^{-1}\boldsymbol{h}_k^H\boldsymbol{h}_i x_i}^{\text{IUI}} + \underbrace{\left(\boldsymbol{h}_k^H\boldsymbol{h}_k + \frac{1}{\gamma}\boldsymbol{I}\right)^{-1}\boldsymbol{h}_k^H\boldsymbol{n}_{BS}}_{\text{Noise}} \tag{2.19}$$

At high SNR, the MMSE decoder behaves similar to ZF. The IUI part from the above equation becomes small since the identity matrix component within the bracket is decreased. While with low SNR, the MMSE decoder behaves similar to MF. The IUI part is increased by increasing γ, but the spatial channel gains are maximised. However, the MMSE decoder has a high complexity compared with ZF and MF decoders. In theory, the noise variance $\boldsymbol{n}_{BS}$ should be estimated. While in practice, a regularised ZF could be used to optimise sigma manually for a certain system.

2.2.4 Linear Precoding Techniques

In DL data transmission, decoding the received signals are not required at the users side. The complexity of the linear equalization is only added at the BS side, where the signal is precoded then transmitted in DL. Therefore, knowing the channel at the BS is essential for DL transmission.

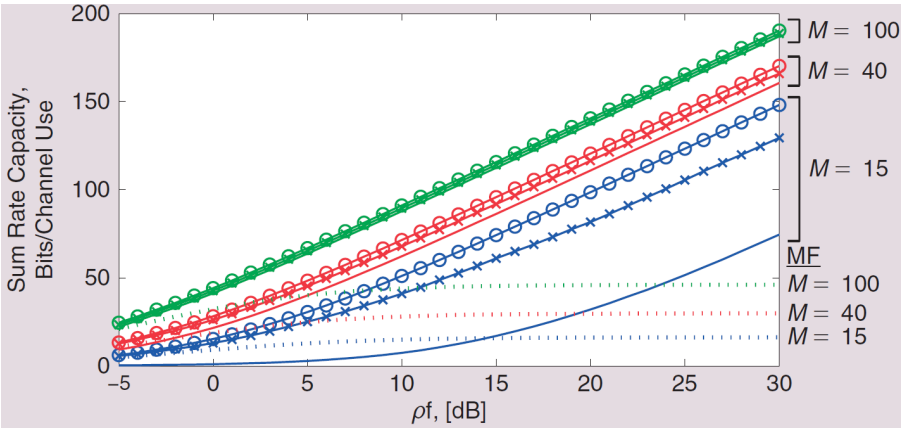

Figure 2.7: Sum-rate comparison between MF, ZF and DPC. IID channels were used with 15 users. The interference-free systems performance is denoted by 'o'. The DPC, ZF and MF performances are denoted by an 'x', solid lines and dotted lines respectively. While, ρf refers to the SNR. Obtained from [63].

Acquiring the CSI depends on the duplexing approach the Ma-MIMO system is using. By using a frequency division duplex (FDD) configuration, overheads resulting from acquiring the channel are scaled by M and K since the channel between each antenna element at the BS and each user should be estimated in UL and in DL. While by using a TDD configuration, the channel estimated in UL transmission can be used to precode the DL signal [68]. This is achieved by exploiting the channel reciprocity which resulting in overheads scaled with K [69]. Because of the lower overheads TDD configuration has, it is most feasible to be used for Ma-MIMO.

With reciprocal channel and perfect CSI, the equalized downlink signal $\hat{\boldsymbol{s}} \in \mathbb{C}^{\mathbb{K}}$ can be mathematically written as

$$\hat{\boldsymbol{s}} = \sqrt{\rho_{dl}}\boldsymbol{H}\boldsymbol{P}\boldsymbol{s} + \boldsymbol{n}_{UE} \tag{2.20}$$

where $\boldsymbol{s}$ represents the transmitted symbol vector from the BS to users in the same cell. The corresponding DL transmit power and the additive noise vector are denoted by ρ_{dl} and $\boldsymbol{n}_{UE}$ respectively. $\boldsymbol{P} \in \mathbb{C}^{M \times K}$ is the linear precoder matrix, formed by using MMSE, ZF or MF

$$where \quad \boldsymbol{P} = \begin{cases} \boldsymbol{H} & MF \\ \left(\boldsymbol{H}\boldsymbol{H}^H\right)^{-1}\boldsymbol{H} & ZF \\ \left(\boldsymbol{H}\boldsymbol{H}^H + \frac{1}{\gamma}\boldsymbol{I}\right)^{-1}\boldsymbol{H} & MMSE \end{cases}$$

Figure 2.7 shows a sum-rate capacity comparison between MF, ZF and DPC in a single-cell system. By using 100 antennas at the BS, ZF achieves the same sum-rate capacity as DPC. While by using MF, number of antennas is not large enough to handle the interference between users with high SNR values.

2.2.5 FDD vs TDD

In the TDD system, the same frequency spectrum is being used for communications between the base station and the users. This can be managed by allocating time slots for each of the uplink and the downlink data transmission. During the UL phase, the BS estimates the CSI. This is done by the orthogonal pilot sequences transmitted from the K users. The UL pilots precede the UL data transmission which enables the BS to estimate the channels and then detect the transmitted signals. The channel reciprocity can be used as an advantage on estimating the CSI for DL data transmission. Not only propagation conditions determine the radio channel, but also the transceiver front-ends at both sides of the radio link. Since different transceiver chains are used at the BS and the UE, calibration techniques need to by used to account for the channels differences [70, 71]. Only K pilots are required for estimating the channel in a TDD system. While in an FDD system, $M+K$ pilots are needed for estimating the DL channels. Prior precoding the DL signal, the BS should receive M feedback coefficients from each user terminal. Figure 2.8 shows a possible samples allocation within a coherence interval and Table 2.2 presents the pilot requirements differences in MIMO between FDD and TDD. Since a TDD system has lower channel estimation overheads, it has been widely accepted over an FDD system [59, 72]. However, Huawei and China Unicom have jointly conducted the 1st FDD based Ma-MIMO field trial [73] and Philippines telecom provider, Globe Telecom, has partnered with Huawei to conduct the world's 1st trial by using an FDD Ma-MIMO commercial product [74]. But no information was provided about the FDD system approach they are using.

Since an FDD system has large channel estimation overheads, much research has focused on providing alternative methods on estimating the channel in FDD. The work in [75] allocates the users into different groups followed by a precoding technique of two stages. This approach called joint spatial division multiplexing (JSDM). The similarity of angle of arrival (AoA) and angular spread (AS) metrics between some users is exploited in the first precoding stage. Low protocol overhead between the users and the BS handles the slow changing in the covariance information of the AoA and the AS metrics. Besides, the UL CSI can be used to refine the estimated covariance matrix. In each group, a smaller matrix dimensions is used during the second precoding stage. Although linear precoding can be used within these sub-channels, it is more feasible to use non-linear precoding techniques. It was shown that by increasing the number of dominant eigen modes in the pre-beamforming computation, a performance improvement can be achieved. This could happen when the similarity between several transmit correlation matrices are applied to larger number of groups. Although this larger number of groups improves the JSDM performance, it also decreases the number of users in the group and increases the feedback overheads. The pre-beamforming method has no advantage when only one users is allocated per group.

Table 2.2: Comparison between the three types of MIMO in terms of the minimum number of pilots required for channel estimation. For the channel estimation feedback, $M > K$ is assumed.

	number of pilots in FDD		number of pilots in TDD	
	Uplink	Downlink	UL	DL
Point-to-point MIMO (no CSI at the transmitter)	K	M	K pilots	M
Conventional MU-MIMO	K pilots + M CSI coeff.	M	K	M
Ma-MIMO	$K + M$	M	K	none

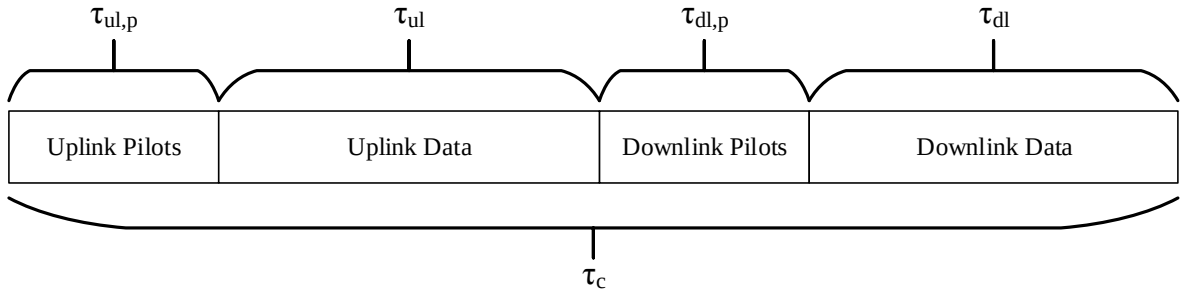

Figure 2.8: Possible samples allocations within a coherence interval.

FDD overcomes TDD only in terms of the power constraint over a certain BW [76]. The Shannon rate for the DL scenario in a TDD system is written in equation 2.21. Since the transmission happens over half of the time, it is divided by two.

$$\frac{BW}{2}\log_2\left(1+\frac{P}{BWN_0}\right) \tag{2.21}$$

While for an FDD system, the BW is divided by two since only half of the available bandwidth is used as shown in the FDD Shannon rate equation 2.22. Therefore, the SNR in an FDD system outperforms the one from a TDD system by three decibels (dB). The work in [76] shows that the TDD multiplexing capability compensates the three dB difference.

$$\frac{BW}{2}\log_2\left(1+\frac{P}{(BW/2)N_0}\right) \tag{2.22}$$

2.2.6 Pilot Contamination

So far in this chapter, a single-cell setup was only considered for the sake of simplicity. Additional challenges come with the multi-cell setup scenario. Pilot contaminations is one of these challenges which can't be avoided even by increasing the number antenna elements at the BS to infinity. It is considered as one of the theoretical upper bounds for increasing the capacity in Ma-MIMO [22]. In a multi-cell setup, the pilot or the training sequences can be contaminated from the

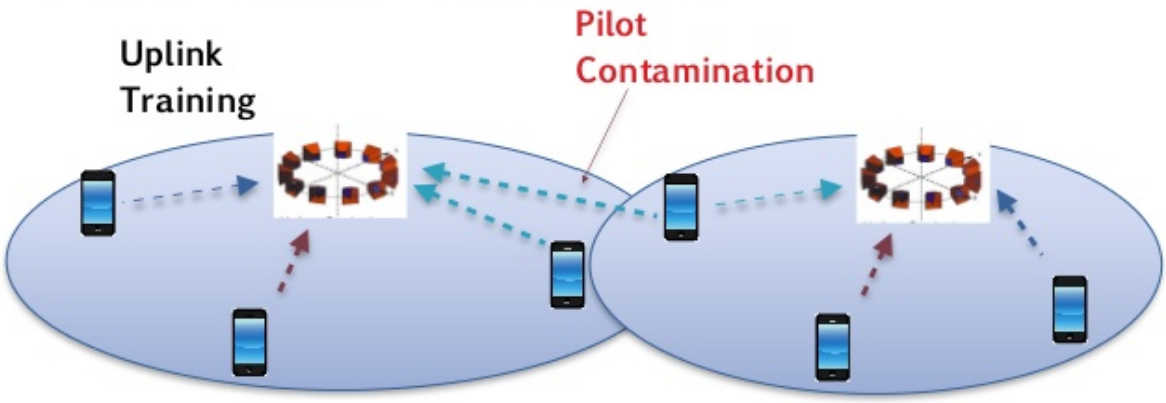

Figure 2.9: Pilot Contamination. Obtained from [79].

adjacent cells. Although the orthogonality of the pilots are preserved in each cell, but due to the resource limitation, the same training sequence might be used in the neighbour cell. This can be seen in Figure 2.9. As a result, the channel estimation might be affected from the adjacent cells which has a very harm impact on the system's performance. The poor decoding and precoding performance could introduce interference between users in the adjacent cells [77]. However, the work in [78] states that the pilot conatmination is not a limiting factor for increasing the capacity in Ma-MIMO. It was shown that with an appropriate multi-cell MMSE algorithm, unlimited asymptotic capacity could be achieved.

Several approaches have been proposed to tackle the pilot contamination problem such as the eigenvalue decomposition (EVD) based channel estimation approach [80], pilot contamination precoding [81], blind pilot decontamination [81] and BS coordination technique [82]. In the BS coordination technique, the multipath AoA from several users is exploited, where a selection of user terminals with a non-overlapping AoA are made. Thus, orthogonal covariance signal subspaces are established. Groups are assigned the same pilot sequence based on their spatial features differences. The safety of assigning the same pilot for the groups is increased by having more spatial features differences between them. And with larger number of users, the performance is increased. The spatial features similarity evaluation is achieved by using the MSE technique. Results by using Gaussian and uniformly distributed AoAs simulation show that the common least squares (LS) estimation method has higher error than the coordinated pilot assignment (CPA) method. The fast fading varies faster than the covariance information needed in this method. This decreases the required amount of overheads for this method. However, larger amount of overheads are needed with high mobility and there are limiting factors for decreasing the required overheads associated with this technique [83].

2.2.7 Interfering and Jamming Sources in Ma-MIMO

In a Ma-MIMO system, the interference and jamming should be handled carefully. The number of potential interfering sources is increased in Ma-MIMO due to the SM nature. The same solution that was proposed for the pilot contamination challenge could be used to tackle the interference problem, where the BSs cooperates with each others [84]. Besides, the wireless network used by the emergency services should be using robust techniques against any potential jamming or interfering sources [85].

Ma-MIMO properties could be used to mitigate the impact of the potential interfering sources. Generally, the estimated channel can be used to detect the jamming signals by comparing the eigenvalue ratios with a pre-determined thresholds. Besides, time slots could be used to detect the interference sources especially when the wireless network is used by the emergency services. The covariance matrix variation can also be used to track the jamming source movement [85].

2.2.8 Ma-MIMO Testbeds and Real-time Results

The majority of the theoretical Ma-MIMO research have adopted the IID mathematical model in their work. Although it is a useful model, but it could also be considered as an ideal scenario. Therefore, real-world channel measurements are an essential step towards understanding the channel behaviour in Ma-MIMO which allows us to produce valid mathematical channel models. Furthermore, real-time performance evaluation is needed for fair comparisons between the Ma-MIMO algorithms and approaches proposed in the theoretical researches. This could uncover the unpredicted challenges and limitations for each technique. Comparisons between the theoretical results and the ones from real-world deployment could be the key for producing new algorithms to enhance the Ma-MIMO performance. Besides, the implementation requirements for some algorithms or techniques could be set as a barrier towards using them in a real Ma-MIMO system. In this section, some channel sounders and Ma-MIMO testbeds are introduced, which have been already published when the author started his research in 2015. The University of Bristol Ma-MIMO testbed is covered in section 3.1.

2.2.8.1 Lund's Ma-MIMO Channel Sounder

Two different types of antenna array configurations were used for the channel sounders in [86] and [87], as shown in Figure 2.10. The first antenna configuration is a compact cylindrical array, where a MEDAV channel sounding solution was used [88]. The second antenna configuration is a physically large virtual linear array, where a vector network analyser (VNA) was used. Although the linear array has lower correlation and higher spatial resolution, it would still be more difficult to deploy compared to the cylindrical array. The work in [86] compared between the channel behaviour in different environments, where co-located LOS and non-line-of-sight (NLOS) were used. Figure 2.11 shows the spatial orthogonality comparison by using four users. The singular

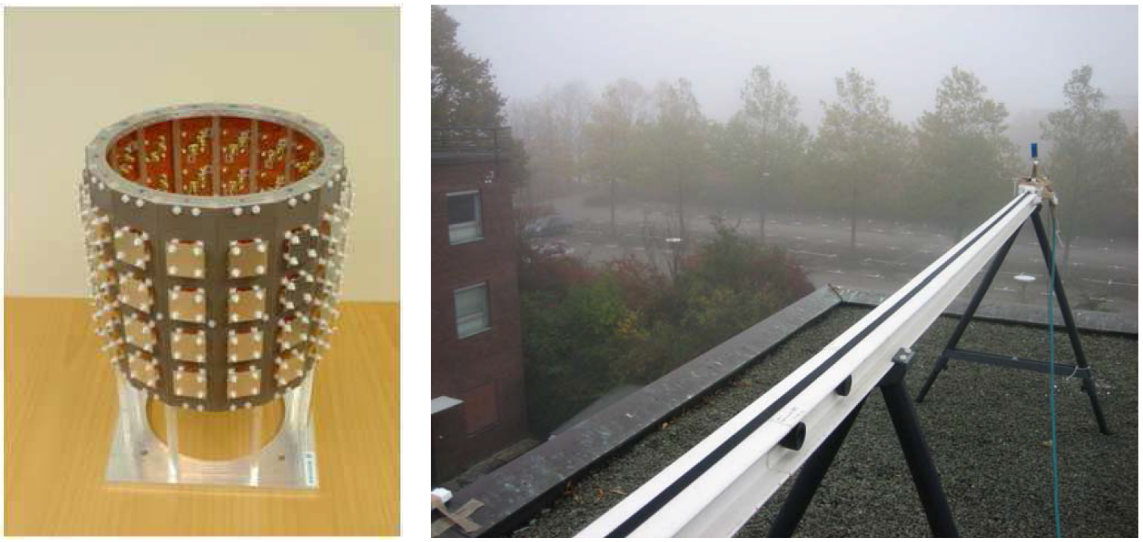

Figure 2.10: Antenna array configurations for Lund channel Sounder. left: cylindrical array. Right: physically large virtual linear array

value spread (SVS) was used for evaluating the spatial orthogonality, since it is one of the most powerful method that can be used in MIMO [89]. It is defined in equation 2.23 as the ratio between the largest singular value to the smallest singular value of the channel's matrix singular value decomposition (SVD)

$$\kappa_b = \frac{\sigma_{1,b}}{\sigma_{K,b}}, \tag{2.23}$$

where b is one resource block. The results in Figure 2.11 show that the NLOS case with linear array antennas performed similar to the IID Rayleigh channel. While the worst performance was achieved by using a cylindrical array with LOS and NLOS scenarios.

The DPC technique was used to evaluate the capacity of the aforementioned scenarios. Although the DPC associated with a very high implementation complexity, but it commonly used as a benchmark indication level because it is optimal in the sense of the sum-rate capacity. Figure 2.12, shows the DPC sum rate capacity by using the same aforementioned environments. The left plot shows the LOS case and the right plot shows the NLOS case, which are corresponding to the conditions in Figure 2.11. The best performance was achieved by using the uniform linear array (ULA) in both cases, where the NLOS performance was almost similar to the IID Rayleigh channel. While the worst performance was achieved by using the uniform cylindrical array (UCA) with a LOS environment. These results indicates that the scattering richness is an essential element on deciding the antenna array configuration for different environment.

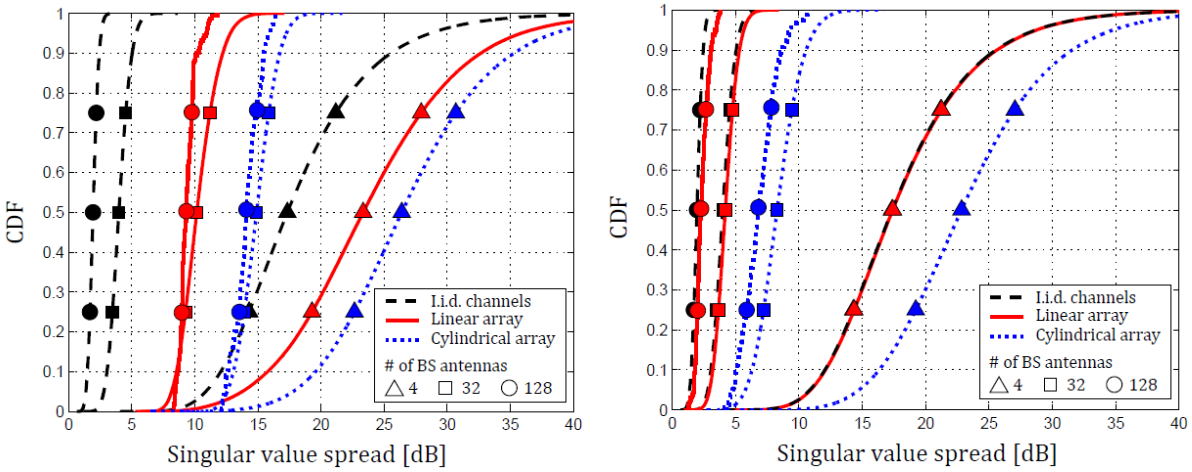

Figure 2.11: SVS comparisons between LOS and NLOS conditions from [86], where left is for the LOS and right is for the NLOS.

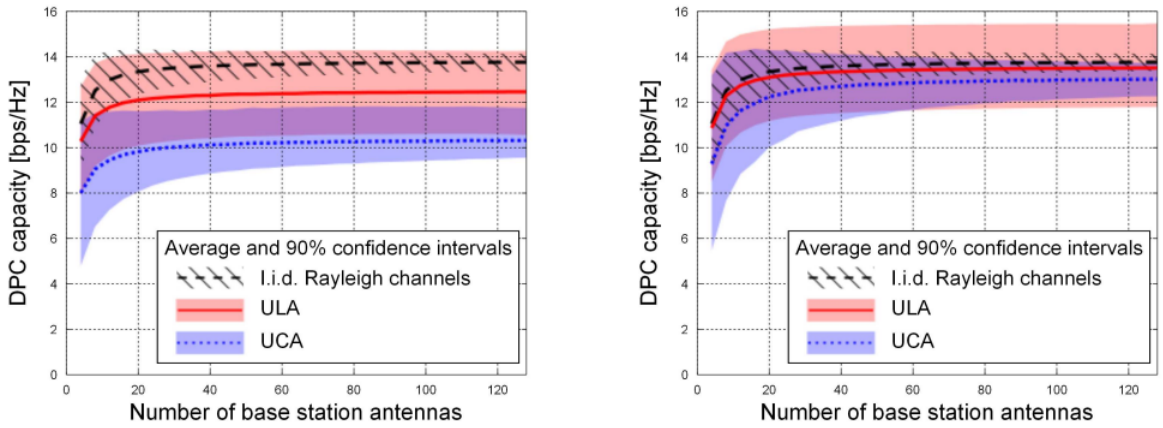

Figure 2.12: Capacity comparisons between LOS and NLOS conditions [86], where left is for the LOS and right is for the NLOS.

2.2.8.2 ARGOS Ma-MIMO Testbed

The first version of Argos test-bed has 64 antenna elements at the BS side, which can serve up to 15 terminals simultaneously [70]. This Ma-MIMO project is based on the Wireless Open-Access Research Platform (WARP). An AD9523 board provides the clock distribution and the sync pulse is being distributed by a different WARP board which enables the synchronisation in the system as shown in Figure 2.13. To increase the set-up flexibility of the testbed, a second version of Argos system was built. The newly customised rack has provided the flexibility of allocating the antennas in different places. Furthermore, dividing the BS into several BSs has become easier as well as increasing number of antenna elements up to 96. In addition to the hardware modifications, the software framework has been modified as well, where additional flexibility have been added to speed up the researchers work. The mobile client is equipped with four antennas,

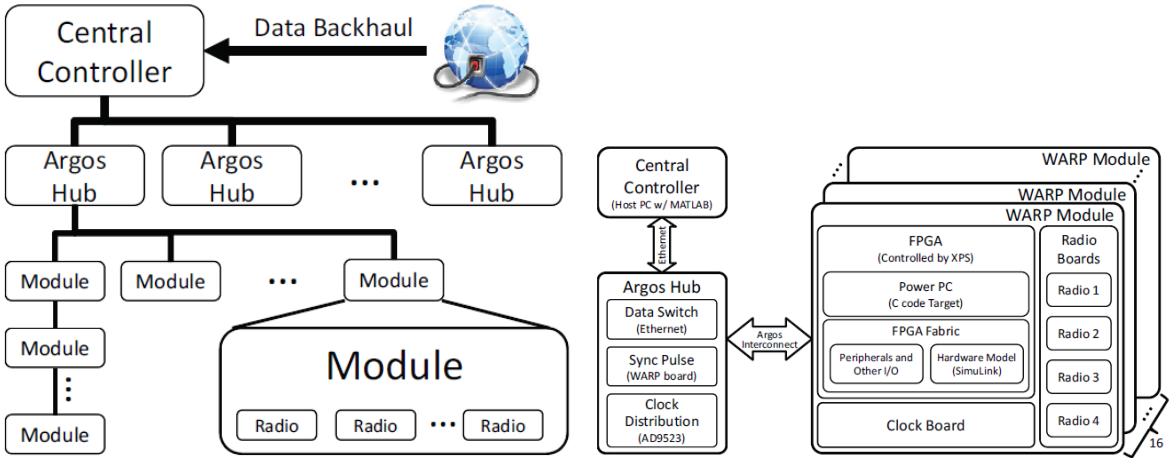

Figure 2.13: Argos Ma-MIMO Testbed [70], where Left is for the architecture and right is for the implementation.

which is named "ArgosMobile". It is capable of supporting out-of-band feedback through an 802.11 interface. The BS can serves up to four ArgosMobiles (equivalent to sixteen spatial streams). The ArgosMobile provides an easy set-up for mobility scenarios because of its eight hours battery life. To increase this flexibility, another version is being considered to provide mobile clients with smaller dimensions and higher level of weather protection.

So far, all the available results from this project are based on channel measurement and no real-time results have been published yet. Figure 2.14 shows the total capacity results and the channel measurements environment. By using a 64 antenna elements at the BS with 15 simultaneous users, the achievable SE could outreach the 80 bits/s/Hz with ZF technique. Figure 2.15 shows a linear sum-capacity increment by adding more simultaneous users with ZF and MF techniques. Although the sum-capacity growth with ZF is greater than MF, it was shown that the sum-capacity could drop rapidly with ZF. Besides, MF could achieve a greater sum-capacity with low transmission power and $M = K$. One adder and one bit-flip is only required for the MF implementation. While the complexity is increased for ZF implementation. The complexity level associated with the matrix inversion operation is MK^2. By using a specialised FPGA, 150 µs is needed for one matrix inversion operation (size of 15×15) [70]. The Argos beamforming (BF) approach has better performance when number of antennas is increased at the BS.

The Argos Ma-MIMO testbed is a TDD system. Two novel reciprocity calibration algorithms are used to handle the UL and DL channel variation caused by the different transceiver front-ends at both sides of the radio link. The first algorithm adopts an internal reciprocity calibration method named, "Internal Calibration", where no feedback is required from the user's side during the initialisation stage. It derives the calibration coefficients by using a single reference BS antenna, which then shares its relationship to the rest of the antenna elements at the BS. A feedback from all users to the reference antenna is still required. The second algorithm is an

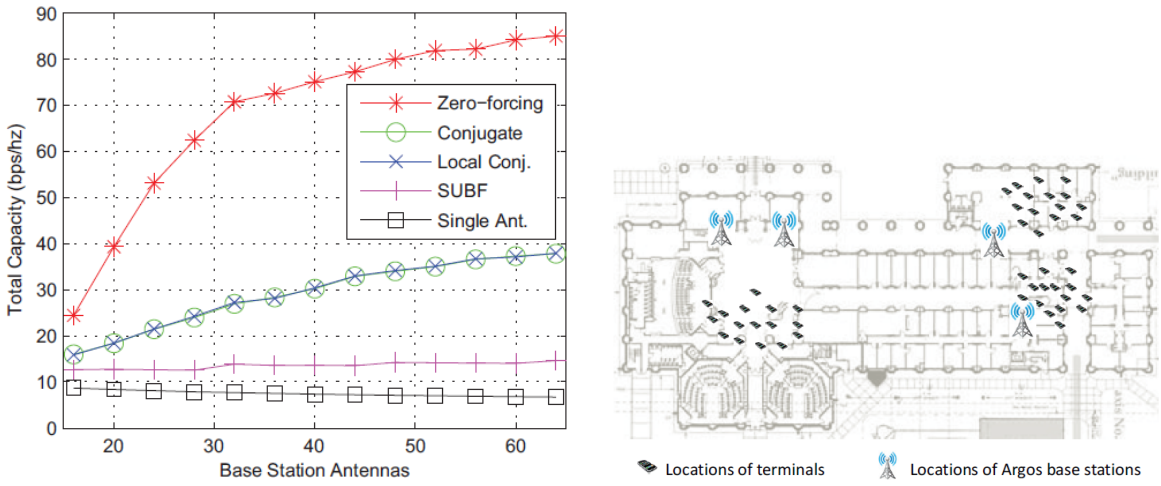

Figure 2.14: Capacity results from the first version of Argos Ma-MIMO testbed [70], where left is the capacity results and right is the testing environment

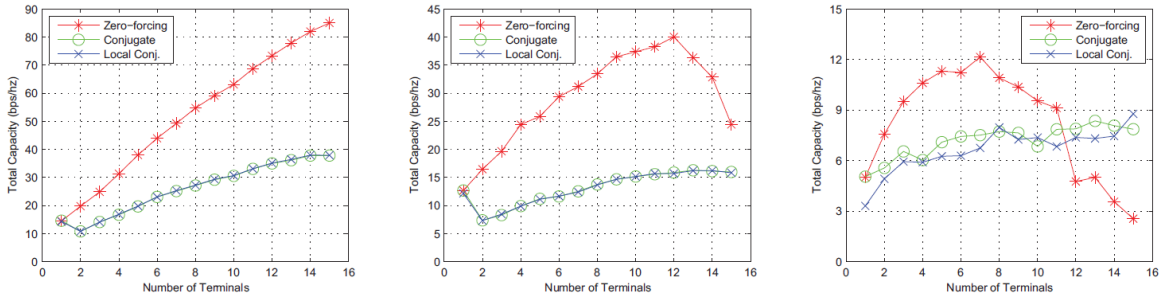

Figure 2.15: The cell-capacity results by increasing number of simultaneous users [70]. From left to right: $M = 64$ with regular transmit power, $M = 15$ with regular transmit power and $M = 15$ with reduced transmit power.

enhanced method of the first algorithm, which is called "Relative Calibration". The reason behind this name is the relative CSI deviation from all the antennas at the BS. Therefore, the same BF can be used by multiplying it with the phase offset. Although the absolute accuracy is no achieved, but a reciprocal channel was established. This work demonstrates how the reciprocal channel problem could be tackled in a TDD Ma-MIMO system. The reciprocity calibration algorithm was evaluated on the Argos Ma-MIMO testbed. The communications between the reference antenna and the remaining antenna elements at the BS was achieved by reporting the channel estimation repeatedly to the main controller due to the limited buffer capacities. 300 µs was needed for this precess, which is still within the coherence time for the trial's environment. The reference antenna was allocated in front of the antenna array with the same spacing distance, to tackle the amplitude variations between them. The results show a very good stability over 4 hours, where the frequency of the internal calibration stage was decreased.

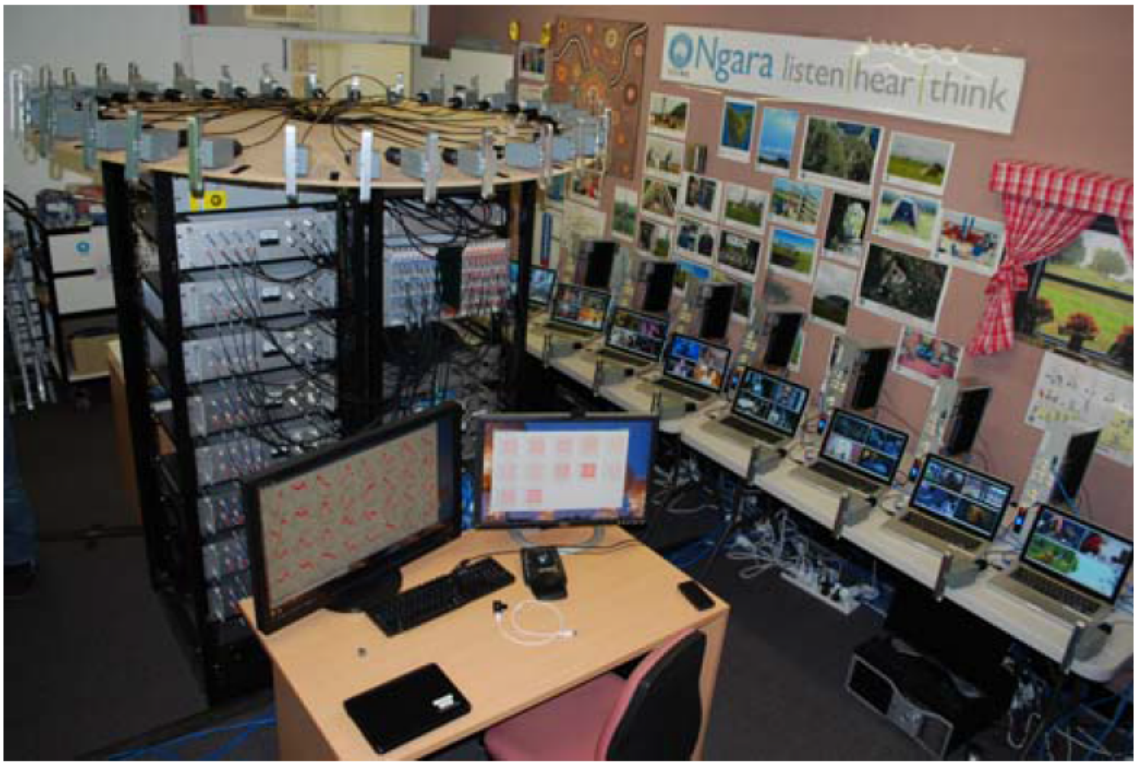

Figure 2.16: Ngara MU-MIMO Testbed in the demonstration environment [90]

2.2.8.3 NGARA FDD MU-MIMO

An FDD MU-MIMO system is presented in [90], with an interest of enhancing the rural wireless internet access. The system has 32 antenna elements at the BS and uses ZF technique for decoding the revived signal in UL and precoding the DL signal. However, the overheads associated with the FDD mode might be a limiting factor for increasing the number of antennas at the BS side. Nonetheless, they have presented a matrix inversion technique with the capability of inverting 3456 matrices (with dimensions of 14×32) in a less than 50 ms and with a high accuracy level. Figure 2.16 shows the environment setup used to demonstrate 14 simultaneous video streams. The BS antennas were allocated in the centre of the room while the users were distributed with lower hight level. MATLAB was used to generate both UL and DL OFDM packets and a SE of 25 Mbits/s was achieved during the video streams. The maximum UL and DL SE were achieved by serving more than eleven simultaneous terminals, where 67.26 bits/s/Hz and 50 Mbits/s are the recorded for the UL data transmission and the DL data transmission respectively. Despite these great results, the project still needs to deal with additional challenges, such as the different propagation channels with rural environment and to increase the number of antenna elements at the BS side.

Table 2.3: Summarising the descriptions of the Ma-MIMO Testbeds

Name	**BS # of Antennas**	**Users # of Streams**	**BW (MHz)**	**Carrier (GHz)**	**Duplex**
Ngara	32	32	28	0.6	FDD
Argos V2	96	16	n/a	2.6	TDD
Lund	100	12	20	3.7	TDD
Bristol	128	12	20	3.5	TDD

2.2.8.4 Nutaq Hardware Solution

On of the main challenges in Ma-MIMO is the hardware implementation. In addition to the complexity associated with some Ma-MIMO techniques, handling the aggregation samples from several RF chains is on of the key challenges [91]. PCIe 8x Gen 3 is a very high speed data bus which is considered as one of the highest speed products in the market. Although it has a capability to transfer up to 80 Gbits/s, it may not be enough to handle the aggregated samples from the Ma-MIMO RF channels at 100 MHz. If 12 bit sampling resolution is used for each RF channel, them maximum number of antennas at the BS would be 33. Titan MIMO achieved a baseband throughput of 768 Gbits/s [91]. This was achieved by using rear transition modules (RTMs) and a MicroTCA.4 chassis. To appropriately handle the point to point hight speed protocol, MiniSAS connectors were used. An alternative approach was adopted for designing Lund's Ma-MIMO testbed and Bristol's Ma-MIMO testbed, where the OFDM modulation/demodulation is performed at the remote radio head (RRH).

2.2.8.5 Lund's Ma-MIMO Testbed

This was the world's first Ma-MIMO testbed operates in real-time [92]. Figure 2.17 shows the BS side with the T shape patch panel antenna array. The testbed was developed through a collaboration between NI and Lund University. The system is capable of using up to 100 antenna elements at the BS and serves 10 simultaneous users. The 100 are connected to 50 dual-channel universal software radio peripherals (USRPs), which are allocated in one rack. University of Bristol constructed a Ma-MIMO testbed with 128 antenna element at the BS by using the same NI platform. In 2015, a collaboration between University of Bristol, Lund University and NI was started. The author worked closely with NI and the Ma-MIMO team at Lund University towards improving testbed performance. For Bristol's testbed implementation, a detailed description is presented in section 3.1.1.

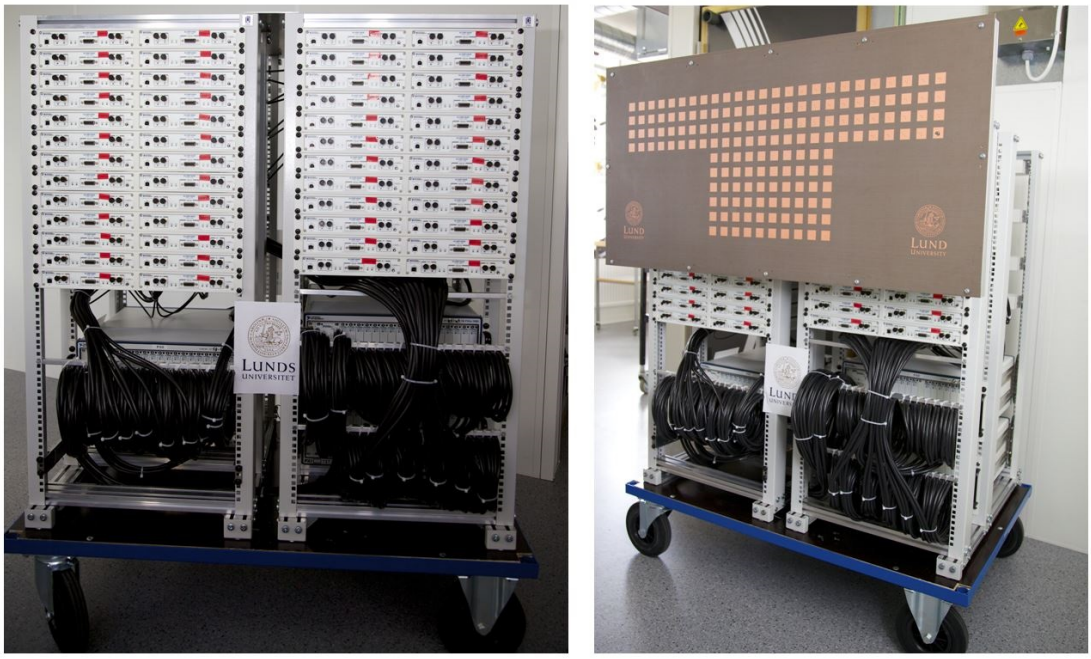

Figure 2.17: Lund's 100 Ma-MIMO Testbed [92].

2.3 Summary

This chapter has reviewed the key aspects of the Ma-MIMO technology and its evolution from the basic MIMO system. The differences between the digital and the analog beamforming was highlighted and the current 3GPP prospective for Ma-MIMO was introduced. A significant capacity improvements with linear algorithms could be achieved by using the original fully digital Ma-MIMO concept, which aggressively exploits the spatial domain. The main challenges towards implementing Ma-MIMO were presented along side with the potential solutions. However, real time evaluation is still required to understand the achievable results and the practical challenges for this technology. The remaining of this thesis shows real-time evaluations from a fully digital Ma-MIMO testbed.

For simplicity, the Ma-MIMO terminology refers to the original fully digital Ma-MIMO concept introduced in [22] unless noted otherwise .

CHAPTER 3

POWER CONTROL AND SYNCHRONISATION ENHANCEMENTS OF A REAL-TIME 128-ANTENNA MASSIVE MIMO TESTBED

In this chapter, the University of Bristol Ma-MIMO testbed is introduced and real-time results from several experimental campaigns are presented. The main results and conclusions of this chapter have been published in [29], [32], [34], [33], [39] and [38] . Below, we summarize the main contributions in this work.

- Operational Enhancements to the University of Bristol Ma-MIMO testbed.
- Characterisation of the channel hardening for Ma-MIMO in an indoor LOS with static users environment and an outdoor LOS with mobility environment.
- Proposing and implementing a novel uplink closed loop power control scheme in a single cell for Ma-MIMO. The proposed algorithm increases both the energy efficiency (EE) and single cell SE with reduced transmission overhead, latency and complexity in the receiver.
- Demonstrating an improvement in channel robustness in Ma-MIMO and the possibility of relaxing the transmitter power control (TPC) update rate.
- Enhancing the synchronisation method between user clients by using a single antenna to broadcast the primary synchronisation signal (PSS) in Ma-MIMO instead of using all antennas with a random static pattern.
- Field trial evaluation and optimisation of the above through several indoor, outdoor and mobility Ma-MIMO measurements campaigns with real-time results using a software-defined radio Ma-MIMO testbed.

Table 3.1: Specifications and Features for the University of Bristol Ma-MIMO Testbed

Number of Antennas at BS	128
Maximum Number of Users	25
Maximum Tx Power per chain	15 dBm
Carrier Frequency	Licence at 3.51 GHz
Bandwidth	20 MHz
MCS	256-QAM, 64-QAM, 16-QAM, QPSK
Duplexing Scheme	TDD
MIMO Linear Decoder/Precoder	MMSE, ZF and MF

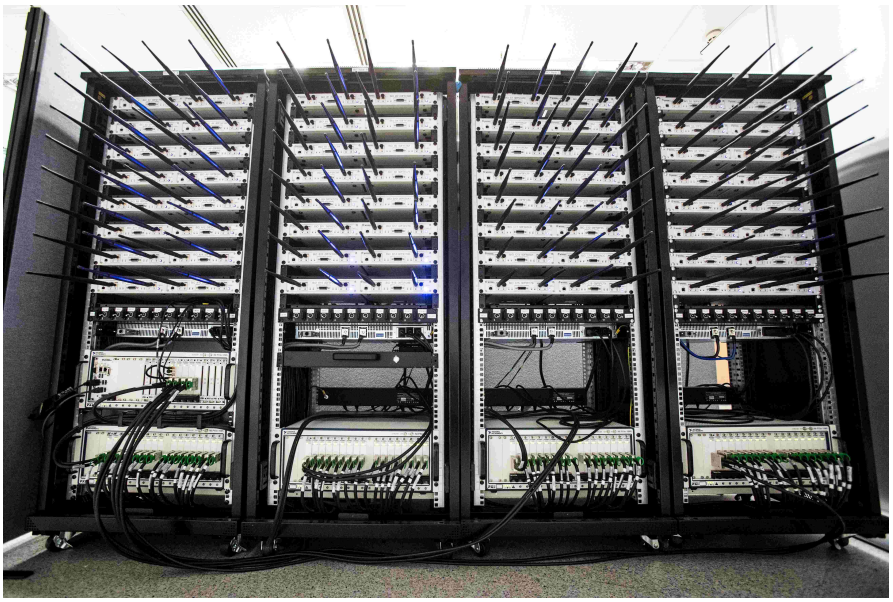

Figure 3.1: 128-antenna Ma-MIMO testbed (BS side)

3.1 Bristol's 128 Massive MIMO Testbed

This section describes the key parts of the 128-antenna Ma-MIMO testbed used to provide the real-time results in this thesis. It also describes all the parts used for implementing the algorithms and the methodologies in this thesis. The testbed was built by the University of Bristol using the NI commercial off-the-shelf (COTS) products which are based on the PCIe platform known as PCIe eXtensions for instrumentation (PXIe). A list of the used components can be seen in Appendix A. Table 3.1 and Figure 3.1 show the key specifications and the BS side of the Ma-MIMO testbed. The monopoles antennas at the BS were replaced with a 128-element patch antenna array for most of the work conducted in this thesis. The array was setup in a 32×4 configuration with alternate H & V polarisations as shown in section 4.1.1 Figure 4.1. The UEs were in LOS and placed in a straight line with 2.5 wavelength spacing at a 3.51 GHz carrier frequency. The system was designed and build to align closely with the TDD LTE air interface with a scalable sub-6 GHz carrier frequency.

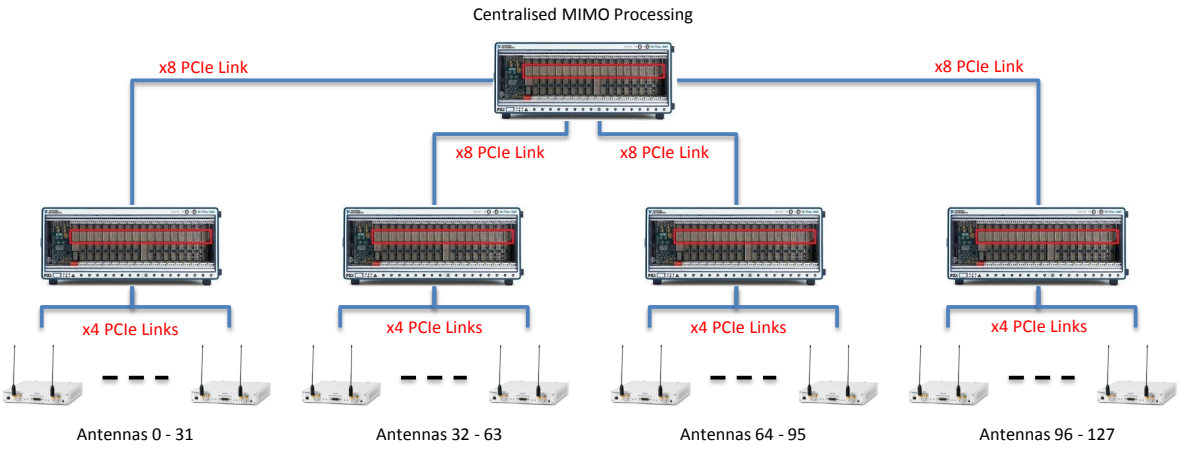

Figure 3.2: Data Plane Architecture at the BS side

3.1.1 System Architecture

The 128 antennas are connected to 64 dual-channel USRPs divided equally into 4 racks as shown in Figure 3.1. These USRPs provide the RF front ends and perform the OFDM modulation/demodulation of each complex subcarrier. The 16 USRPs in each rack linked via x4 PXIe links to a PXIe-1085 chassis with 18 slots acting as a switch. The PXIe-1085 chassis from each rack is then connected via a x8 PXIe link to the main chassis allocated on rack A (first rack from the left in Figure 3.1). The main chassis has 4 FlexRIOs 7976R co-processors performing channel estimation and MIMO detection in UL and reciprocity calibration and precoding in DL. Figure 3.2 shows the chassis structure of the Ma-MIMO testbed. The main chassis also has the 6674T timing card which is used for synchronising the USRPs, as well as the host controller used for configuring and programming the testbed.

3.1.2 Reciprocity Calibration

The Ma-MIMO testbed estimates the calibration coefficients by using the method in [71], which only occurs during the system initialisation. For most research scenarios, this approach is sufficient once the system's temperature has reached the stability mode where no significant drift is happening [92]. The reciprocity calibration is an interesting area for future, where on-the-fly recalibration can be used. The calibration coefficients are stored to be used in constructing the precoding matrix, which is applied prior each DL data transmission [69].

3.1.3 Frame Structure

Figure 3.3 shows the Ma-MIMO testbed frame structure which is closely aligned with TDD LTE physical layer. The switching periodicities of 5 ms and 10 ms used in TDD LTE was changed to suit the reciprocity requirement for the DL in Ma-MIMO [93]. By reducing the switching

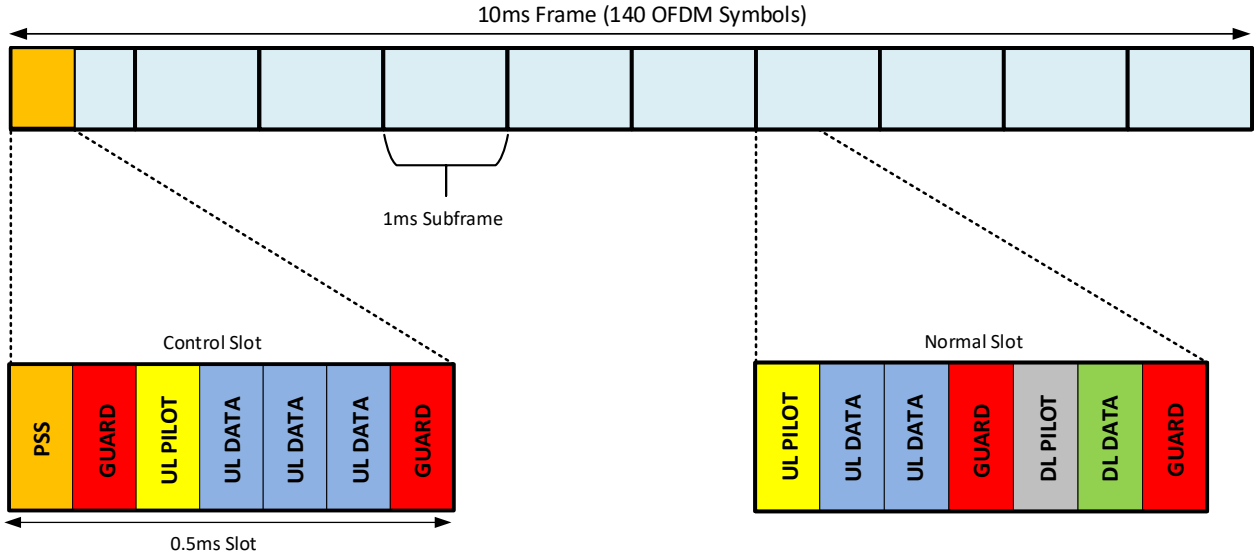

Figure 3.3: physical layer (PHY) frame structure of the Ma-MIMO testbed

periodicities to the half of this, the UL and the DL transmission occur within the coherent time of the channel. The first half subframe is the control slot, where the PSS signal is broadcasted. All modulation and coding scheme (MCS) used in LTE are supported by the Ma-MIMO testbed [94].

3.1.4 Timing and Synchronisation at the BS Side

To ensure synchronized sample acquisition and coherent RF chains between all the USRPs, frequency and trigger sources were distributed as illustrated in Figure 3.4. The NI 6674T PXIe timing card [95] located in the master chassis was used to provide 10 MHz frequency source through an oven-controlled crystal oscillator (OCXO) . It is an extremely stable frequency source with an accuracy of < 5 parts-per-billion (ppb). Nine pieces of Octoclock hardware [96] were used to distribute the frequency source between all the USRPs through an equal length cables. Each Octoclock amplifies the 10 MHz source then divides it between eight USRPs. The start trigger pulse is generated from the first USRP, which is linked to the 6674T. Then the pulse is distributed between all the USRPs using the same Octoclock network for distributing the frequency.

3.1.5 Synchronisation Between Users

The 2953R USRP model is used for the UE implementation. This USRP model was chosen to add the global positioning system (GPS) option for improving OTA synchronisation. Two users with a single antenna or one user with two antennas can be obtained from one USRP. A laptop is used as an equivalent to the PXIe8135 controller in the BS, which is connected via x1 PCIe link. Time alignment and frequency offset correction between the BS side and each UE are achieved

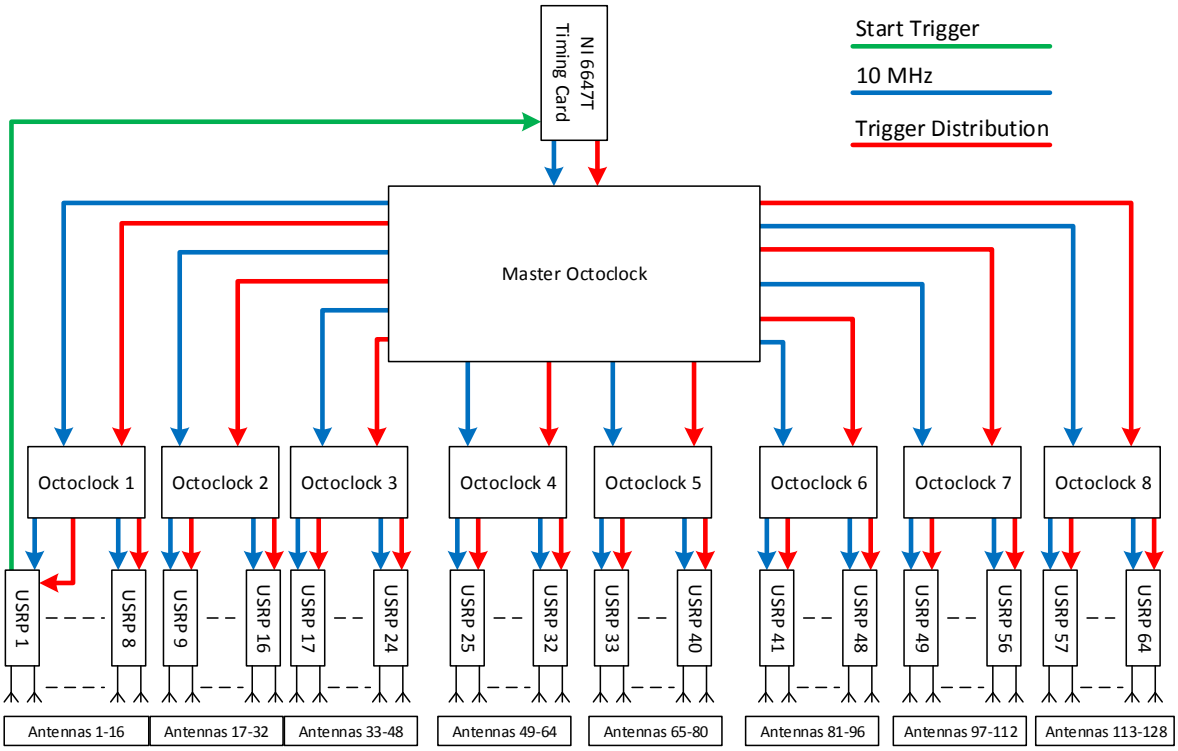

Distribution of frequency and trigger sources to all USRPs

Figure 3.4

by using three different methods. This section outlines these methods such that they can be referenced as required when viewing the results and comparisons that follow.

3.1.5.1 Extending the BS Octoclock Network Using Cables

In this method, the Octoclock network used at the BS side was extended to link all the UEs. The extended Octoclock network was established by using additional Octoclocks and cables. One Octoclock is linked to the 6674T located in the master chassis. This Octoclock can serve up to sixteen UEs from eight USRPs. To increase number of UEs, the output of the Octoclock was linked into two additional Octoclocks. This covers the maximum number of 25 users the Ma-MIMO testbed can serve. Equal length cables were used between the UEs and the Octoclocks, while a manual sample offset was introduced at the BS to account for the propagation delay introduced by the cables.

3.1.5.2 Broadcasting PSS Using Random Static Pattern From all Antennas

This method enables OTA synchronisation using the LTE PSS, which is Zadoff-Chu (ZC) sequence [97]. The PSS is broadcasted at the first OFDM symbol as shown in Figure 3.3. This signal is broadcasted from each antenna at the BS forming a static pattern, which doesn't take into account

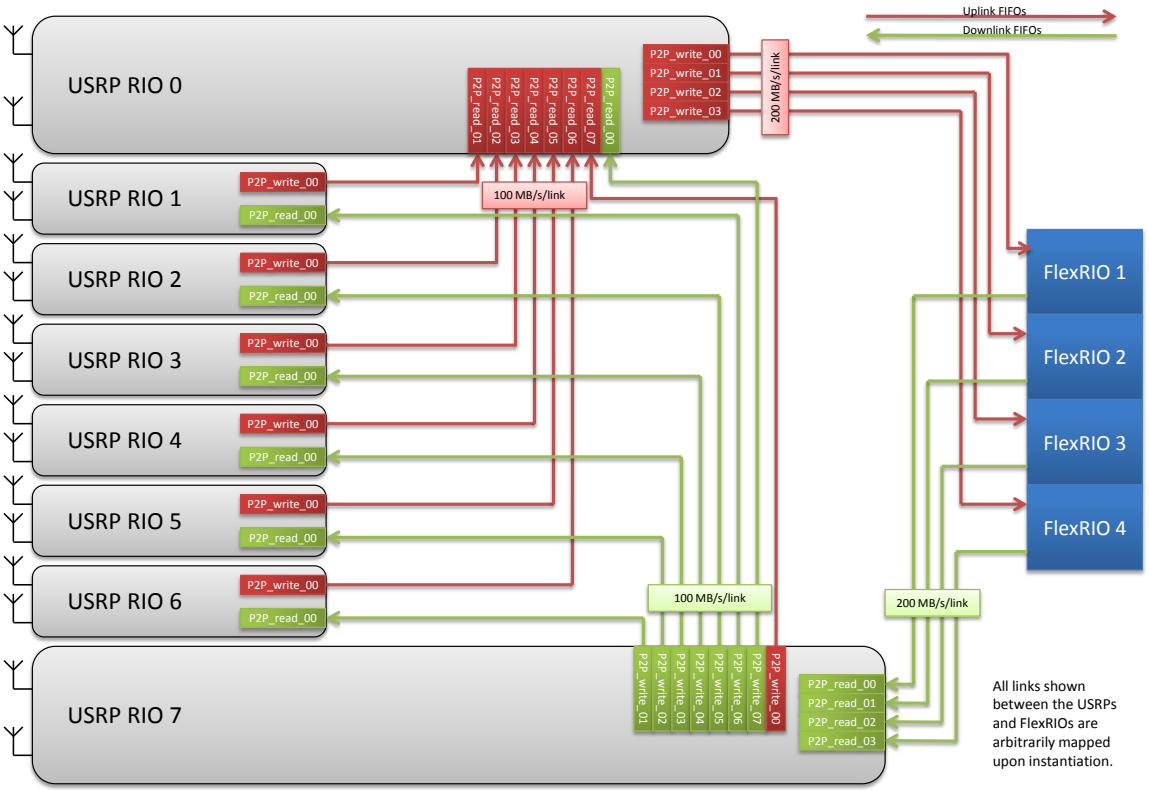

Figure 3.5: USRP subsystem mapping to the FlexRIOs.

the users' locations. The random static pattern might not maintain a stable synchronisation due to the poor PSS received signal at the user side. This is caused by coherently combining all the PSS signals without considering the user's location. The GPS at the user side can be used to improve the synchronisation stability for this method.

3.1.5.3 Broadcasting PSS From Single Antenna[1]

An external antenna and one USRP are used to broadcast the PSS in this method. The external USRP is timed and synchronised with all the USRPs located in the four racks. This is achieved by extracting the frequency and the trigger sources from the 6674T located in the master chassis. On the RRH FPGA of the external USRP, ZC sequence and the LTE PSS were implemented. On the other hand, the PSS was removed from all the RRH of the 64 USRPs. The output of the external USRP is connected to an amplifier to compensate the loss of the antenna array gain, caused by using a single antenna. During the first OFDM symbol duration in the PHY frame structure, the external antenna broadcasts the PSS. A comparison between this method and broadcasting PSS using random static pattern from all antennas is presented in section 3.3.

[1]The author designed and implemented this method to further enhance OTA synchronisation of the Ma-MIMO testbed

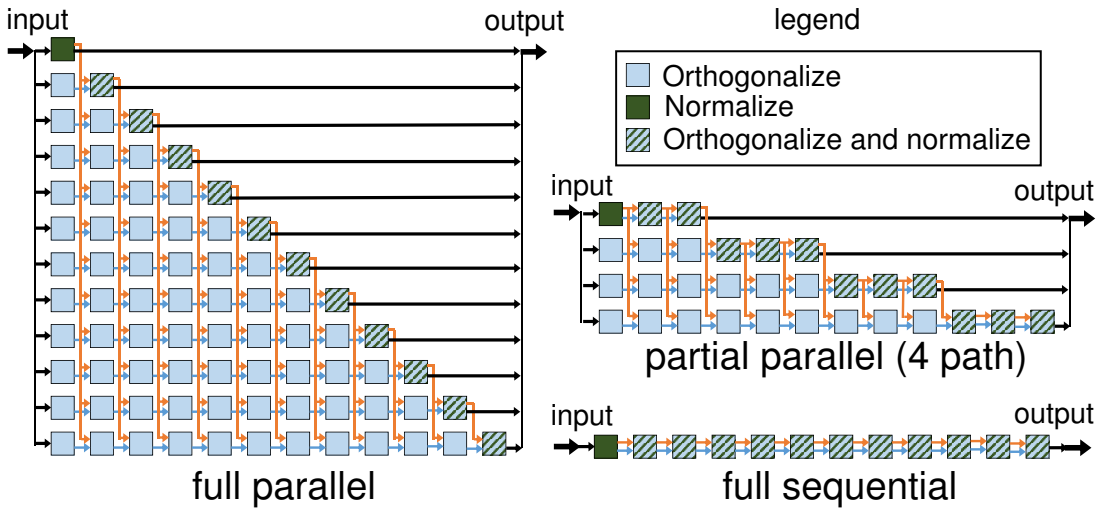

Figure 3.6: Formulating systolic array based on the QR decomposition

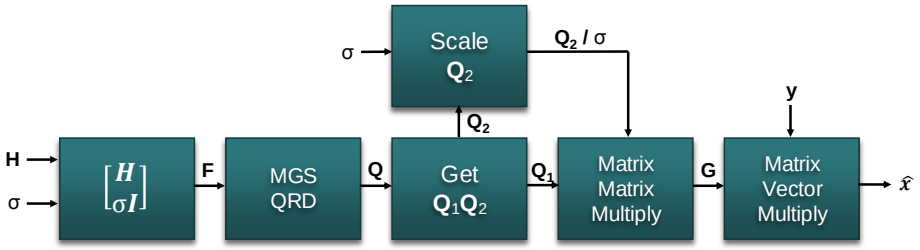

Figure 3.7: The QR Decomposition for MMSE used in the Ma-MIMO testbed

3.1.5.4 MIMO Processorsa[2]

Each UE has a constant identity (ID) i.e., UE0, UE1, ... UE24. The RB size of twelve subcarriers and the 15 kHz subcarriers spacing for the Ma-MIMO testbed aligns with the LTE, where one pilot per RB can be assigned for each UE. A pilot is transmitted in the beginning of the K^{th} subcarrier, where K is equal to the users ID. Although this method doesn't calculate a full detector/precoder for each subcarrier, the performance isn't highly affected as it was shown in [98]. The advantage of this method is to reduce the required memory for storing the CSI by a factor of K. A Least-square algorithm and zeroth-order hold across subcarriers are used for channel estimation, while interpolating between subcarriers will be considered as a future enhancement. This approach decreases the overall processing rate from 16.8 MS/s to 16.8 MS/s/12 = 1.4 Mmatrices/s, since only one 128×12 detection matrix is needed per twelve subcarrier RB.

A partially parallel 4-path QR decomposition based on the modified gram schmidt (MGS) described in [99, 100] was used to build the detection matrix. Four FlexRIOs were used for the implementation with a clock rate of 200 MHz as shown in Figure 3.5. The systolic array QR

[2]This method was designed and built by National Instruments. The work conducted in this thesis is based on this MIMO processing method.

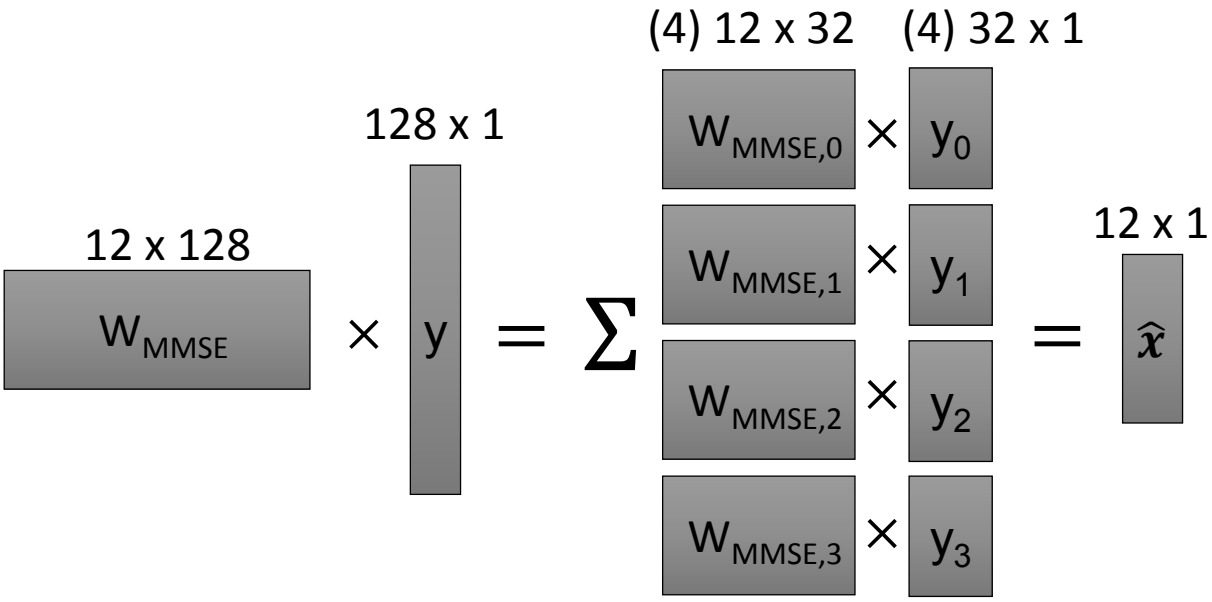

Figure 3.8: 128 × 12 Ma-MIMO detection

decomposition shown in Figure 3.6 creates a balance between the throughput requirement and resource utilization. This can be achieved by exploiting the MGS property to calculate $\boldsymbol{R}$. The FPGA resource usage can be decreased by using the same circuitry that derives $\boldsymbol{Q}$. The following equation shows the MMSE detection method:

$$\boldsymbol{W}_{MMSE}\boldsymbol{y} = \left(\boldsymbol{H}^H\boldsymbol{H} + \sigma_n\boldsymbol{I}\right)^{-1}\boldsymbol{H}^H\boldsymbol{y} \tag{3.1}$$

The above equation can be rearranged as follows:

$$\boldsymbol{W}_{MMSE} = \boldsymbol{R}^{-1}\boldsymbol{Q}_1^H = \frac{\boldsymbol{Q}_2\boldsymbol{Q}_1^H}{\sigma_n} \tag{3.2}$$

Where:

$$\boldsymbol{F} = \begin{bmatrix}\boldsymbol{H}\\ \sigma_n\boldsymbol{I}\end{bmatrix};\ QRD(\boldsymbol{F}) = \begin{bmatrix}\boldsymbol{Q}_1\\ \boldsymbol{Q}_2\end{bmatrix}\boldsymbol{R};\boldsymbol{R}^{-1} = \frac{\boldsymbol{Q}_2}{\sigma_n} \tag{3.3}$$

Figure 3.7 summaries the MMSE process using QR decomposition. ZF and MF can be performed by setting sigma to a very small value and by skipping the orthogonalisation steps of the MGS procedure respectively. Formulating $\boldsymbol{W}_{MMSE}$ and $\boldsymbol{W}_{MMSE}^H$ are followed by the full bandwidth computation for all the 100 RB, where UL subcarriers and DL data symbols are decoded and precoded respectively. The partial parallel computation is shown in Figure 3.8, which is carried out in thirty two 200 MHz clock cycles.

3.1.6 Host Processing

The 64 USRPs and the 4 FlexRIOs are configured through the PXIe8135 controller in the master chassis located in rack A. All the hardware pieces of the BS and their locations' are known to

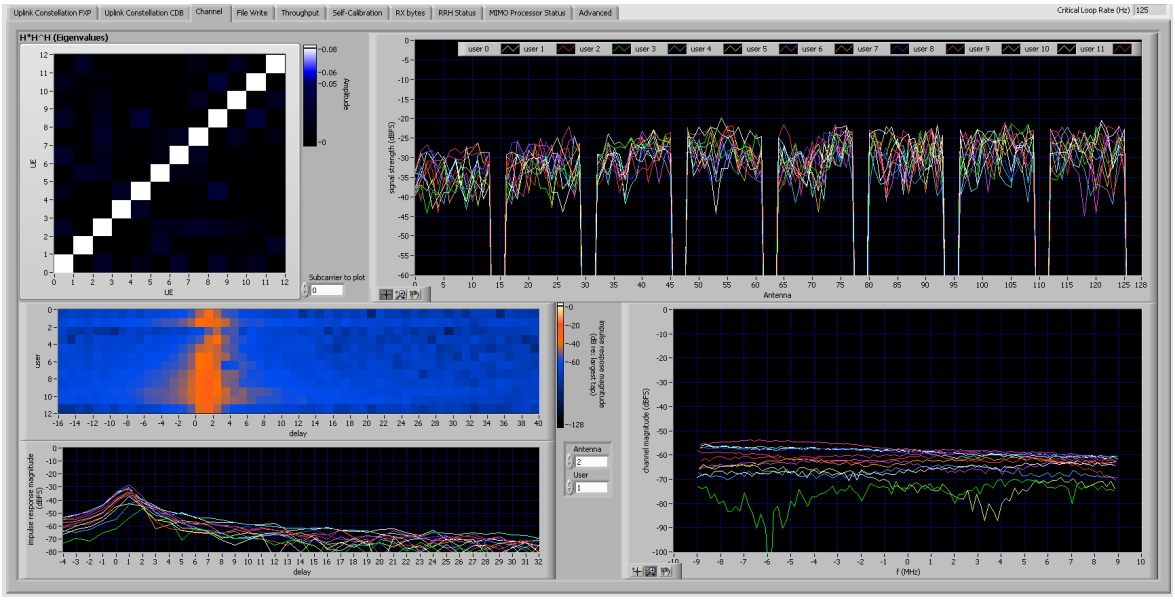

Figure 3.9: Displaying real-time results by the Host.

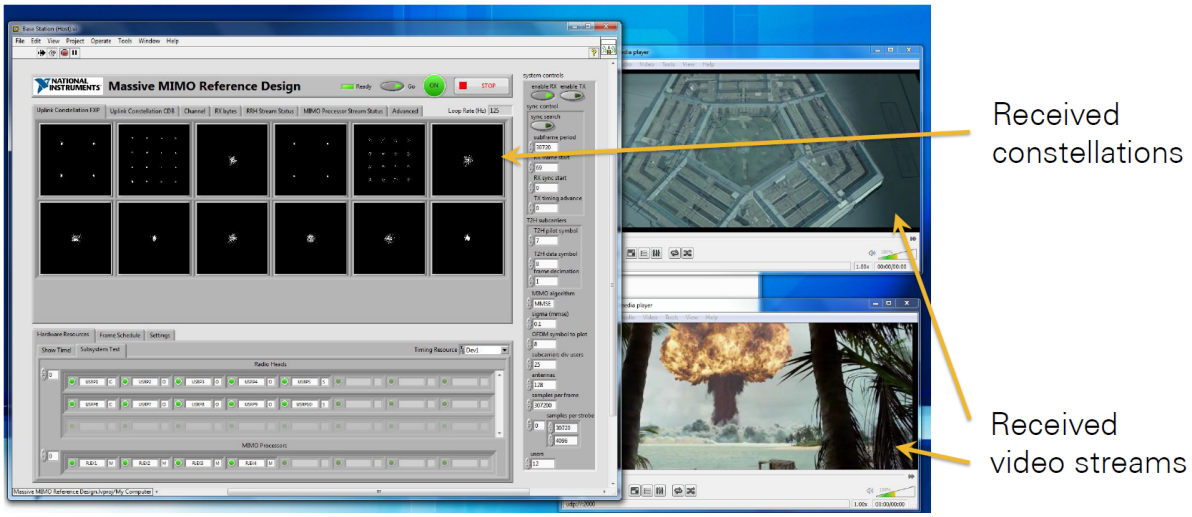

Figure 3.10: Visualising the received constellations and displaying video streams

the host software. By executing the software, peer-to-peer (P2P) routing are established for all the subsystems (subsystem is a group of USRPs). As described in section 3.1.2, the reciprocity calibration is established during the system initialisation. The memory on-board each of the 64 USRP is used to store the calibration coefficients, which are used for DL. After initializing the system, all the bit-files are loaded and the P2P routes are established. Once the system is ready to run, the graphical user interface (GUI) informs the user to click the run button. Then all the USRPs are triggered and synchronized as described in section 3.1.4 to enable the flow of samples.

After that, the host controller become the primary interface between the system and the user. Real-time results can be visualised on the connected screen as shown in Figure 3.9, allowing

the user to monitor the system's performance. The host can also changes different variables while the system is ruining such as power level, synchronisation method, power gain, number of active users, etc. The option for controlling new variables while the system is running should be carefully programmed and added to the framework. Furthermore, the host can acts as a data source and receiver. For example, it can transmit and receive video streams through User Datagram Protocol (UDP) interface as shown in Figure 3.10

3.2 Uplink Power Control

The large number of antennas at the BS has a great impact on the system's performance. Many potential advantages are expected and numerous implementation challenges are addressed in [77]. The channel hardening synonymous with Ma-MIMO technology [57] could be exploited to increase the link EE if UL power control is considered. In LTE, open loop and closed loop algorithms are used for power and signaling control. The minimum signaling rate depends on operational conditions (environment and dynamics). The open loop algorithm is used when the UE joins the system or when the channel conditions vary, while the closed loop algorithm is used when the channel conditions are more stable. In the open loop mode, the UE derives the desired UL power level by importing different values, sent from the BS, into a predetermined equation [101]. While in the closed loop mode, the UE adjusts the UL power according to the TPC command sent by the BS. The TPC command is interpreted according to a predetermined lookup table which increases or decreases the UL power level with constant values [102]. A simple receiver with a basic UL power control design is desirable for Ma-MIMO [103], yet little research has been experimentally conducted on this topic. The UL power control algorithm in [104] is based on a MMSE receiver, which brings with it significant complexity. The UL power control presented here has two stages: the average UL SINR is determined, which is considered as the lower bound, followed by a joint iterative pilot and data power control algorithm. The work in [105] has considered power control for a single cell. It maximizes the minimum SE by converting it into a geometric program (GP) and finds the local maximum points. A joint power and data allocation algorithm is proposed in [106] which tends to improve the uplink EE based MMSE channel estimation followed by MRC receive processing. The UL power control algorithms proposed so far for Ma-MIMO are based on pilot and data power allocations amongst users, either within the same or adjacent cells. To the best of the author's knowledge, no power control technique designed for Ma-MIMO has yet been tested in a field trial.

This section introduces a simple closed loop UL power control algorithm in a single cell for Ma-MIMO based only upon the pilot channel estimation. Simple open loop UL power control is still needed prior to the proposed closed loop UL power control. The channel hardening phenomenon in Ma-MIMO provides an improved channel robustness, as it is shown later in section 3.2.3.2 and section 3.2.6.2, which allows for fewer UL power control adjustments. A novel TPC mapping and

de-mapping algorithm is proposed to obtain a high EE by transmitting only the minimum power required. Furthermore, the single cell SE is increased by decreasing the interference level caused by the spatial correlation between UEs.

3.2.1 System Model

A single-cell Ma-MIMO architecture is considered in this work. The BS is equipped with M antennas serves K single-antenna users simultaneously where (M ≫ K). The system operates in TDD mode and uses the same time-frequency resources for all users. The UE transmits an UL pilot for the channel estimation. The estimated channel matrix between the UEs and the BS is denoted by $\hat{\boldsymbol{H}}_{ul} \in \mathbb{C}^{\mathrm{M}\times\mathrm{K}}$. The BS derives the user-side Gram matrix, which is given by:

$$\boldsymbol{G} = \hat{\boldsymbol{H}}_{ul}^{H}\hat{\boldsymbol{H}}_{ul} \tag{3.4}$$

where the value of each complex element taken as its absolute $|g_{i,j}|$ for all i and j. It then approximates the SINR for each UE using the approximation method introduced in section 5.1. The maximum and minimum accepted SINR are predetermined and saved at the BS as a threshold based on the MCS in use. For the field trial described in this chapter, the maximum SINR threshold ($SINR_{max}$) is the lowest SINR value required for a sufficient transmission by using 256-quadrature amplitude modulation (QAM). Similarly, the minimum SINR threshold ($SINR_{min}$) is the lowest SINR value required for a sufficient transmission using binary phase-shift keying (BPSK) based access.

3.2.2 Spatial Closed Loop UL PC Algorithm

The proposed algorithm exploits the spatial degrees of freedom provided by Ma-MIMO to achieve the highest SINR for each user by considering the mutual spatial correlation arising from other users. It also minimizes the required UL transmit power to achieve the highest possible UL SINR per user without increasing the complexity at the user equipment. It is based only on the physical layer parameters. The BS controls the user transmit power using only two bits in a TPC command and the introduced algorithm increases both the EE and single cell SE with reduced transmission overhead, latency and complexity in the receiver. The proposed algorithm supports several popular linear MIMO decoders and precoders including MMSE, ZF and MF. A simple UL open loop power control is needed prior applying the adjustment mechanism.

The BS has an acceptable inter-user spatial correlation threshold (I_{Th}) which represents the acceptable ratio between g_{ii} and g_{ij}. The UEs with high spatial correlation are paired according to the following equation:

$$\mathbf{CU}_n = \{\mathbf{UE}_i, \mathbf{UE}_j\} \tag{3.5}$$

where $i, j \in [1, K]$ and $n \in [1, K-1]$.

As **CU** denotes the correlated users, the BS then derives the SINR range for each pair as follows:

$$SINR\ \ Range_n = |SINR_i - SINR_j| \tag{3.6}$$

The adjustment mechanism at the BS divides the UEs into three groups based on SINR and I_{Th} values. Each group targets a desired SINR value, denoted as DSINR. The groups are illustrated in Figure 3.11, and are divided as follows:

1. Group 1 (red arrows): UE SINR value $\notin [SINR_{min}, SINR_{max}]$. The BS tells the UE to increase or decrease its power so that the received SINR reaches the acceptable range.

2. Group 2 (Green arrows): The UE SINR is within the acceptable range and the SINR range value is greater than 0.5 dB (in this work, a 0.5 dB step-size has been adopted as the minimum resolution. But an adaptive method for changing this value based on the real-time results is an interesting area for further work.). The BS assigns a desirable SINR for both UEs as $DSINR_n = \min_n SINR_n$. The BS then tells each UE either or not to decrease its transmit power so that the received SINR for both users equals $DSINR\ \pm 0.5$ dB.

3. Group 3 (blue arrows): Either the interference is low between the UEs or the SINR range is less than 0.5 dB. In both cases, the BS will tell the UEs to increase their transmit power if it does not reach the maximum threshold, or it will tell them to keep using the same transmit power.

The SINR values in group 2 are adjusted into DSINR. This is going to reduce the spatial correlation between the UEs. In group 3 the spatial correlation will already be low, so the BS starts to increase the SINR for both UEs by increasing their transmitting power. This step will ensure that the SINR growth for the UEs won't affect the others, and thus, the BS ensures the SINR converges between the correlated UEs into the maximum harmless level between them, where any additional increment would affect other UEs. The UEs in our design do not estimate the SINR or the distance; they only apply the power adjustment according to the received TPC command. This will reduce the complexity of the receiver as well as the overheads sent by the BS. Open loop power control is still required when the users join the system, but can then be followed by the proposed UL power control in this section.

3.2.3 Investigating Channel Hardening for Ma-MIMO

The proposed UL power control algorithm is based upon the assumption that Ma-MIMO achieves highly improved channel robustness, where fewer UL power control adjustments are needed. The lower atrium in the University of Bristol's Merchant Venturers Building was used to evaluate the channel hardening in real-time. The synchronisation between each UE and the BS was

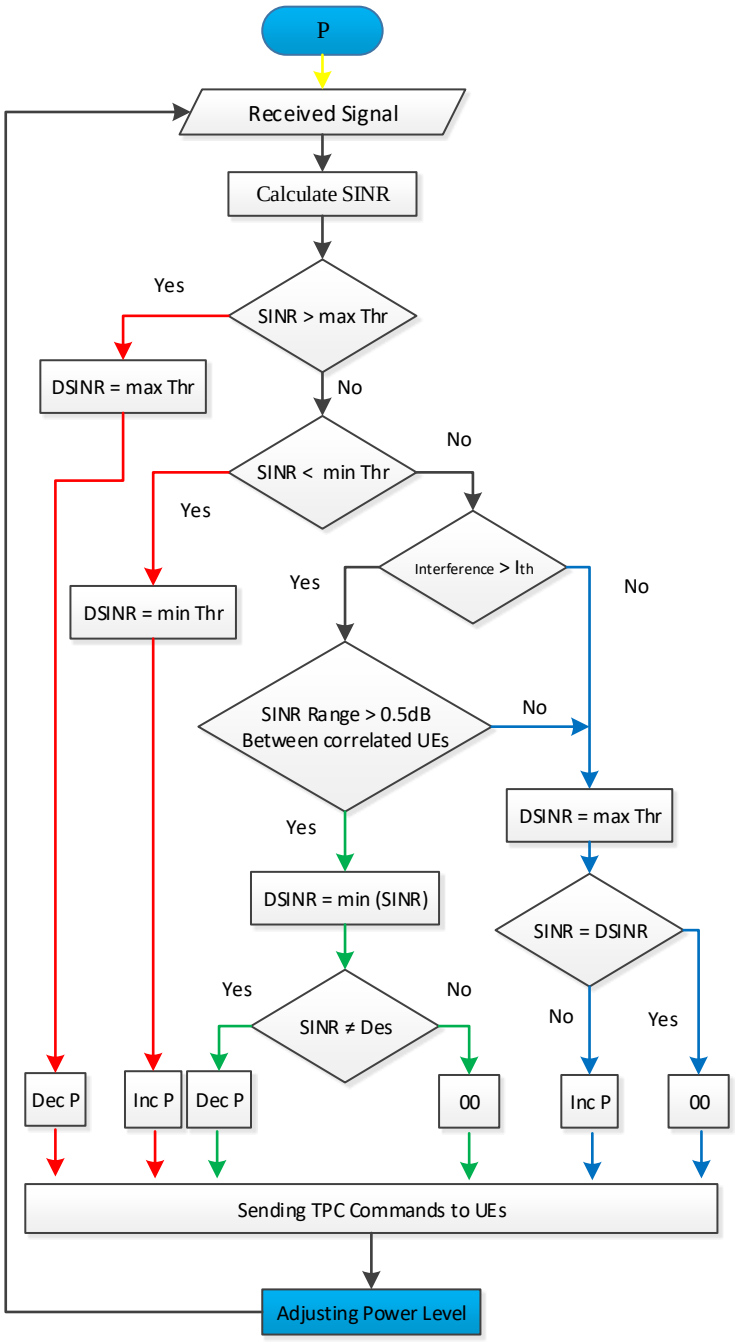

Figure 3.11: Spatial uplink power control algorithm for Ma-MIMO. Red arrows are group 1. Green arrows are group 2. Blue arrows are group 3. Shapes filled in blue are at the UE while others are at the BS.

achieved via cables as described in section 3.1.5. Figure 3.12 and Figure 3.13 show the LOS indoor environment and the user side of this trial respectively .

Figure 3.12: Measurements environment for the indoor supporting experiments.

Figure 3.13: User side for the indoor supporting experiments.

3.2.3.1 MU-MIMO Channel Robustness with 32 Antennas in LOS Indoor Environment

The MU-MIMO channel was measured by the Ma-MIMO testbed with 32 active BS antennas. The distance between the BS and the 12 single antenna clients was 20.81m and a static environment was maintained. Figure 3.14 left shows the $\boldsymbol{G}$ matrix, which was averaged over 100 captures of the channel measurement data.

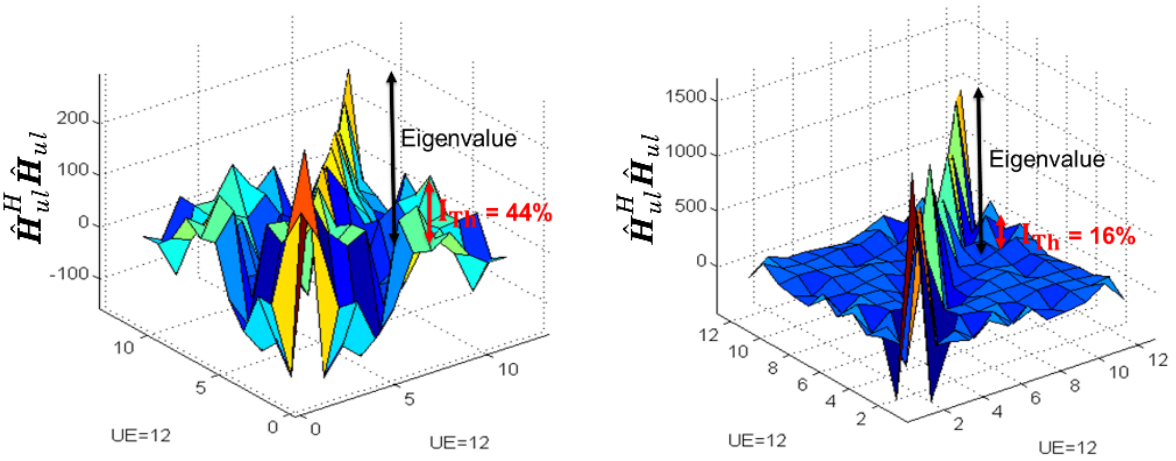

Figure 3.14: User side Gramian matrix for 12 UEs with single antenna (not normalized). Left, MU-MIMO with 32 antennas at the BS. Right, Ma-MIMO with 112 antennas at the BS.

3.2.3.2 Ma-MIMO Improved Channel Robustness in LOS Indoor Environment

Here, the channel was measured by the Ma-MIMO testbed with 112 active antennas at the BS. The distance between the BS and the 12 single antenna clients was 11.6 m. Three people walked pseudo-randomly during the channel measurements. One person walked right next to the client antennas, while the others were walking between the BS and the clients. The client transmit power was adjusted before the channel measurements, but power control was not used during this set of measurements. Figure 3.14 right illustrates the greatly improved channel robustness averaged over 400 captures of the channel measurement data, and the channel hardening phenomenon can be clearly seen. These conditions would allow our proposed algorithm to work effectively. By comparing the results from Figure 3.14, the ratio between g_{ii} and the max g_{ij} was decreased from 44% to 16%. Therefore, less UEs require the paring process in equation 3.5, which means less UEs are considered in group 2. Most of the UEs will be assigned into group 3 which only requires an increment on the UE transmit power till it reaches the $SINR_{max}$. Once $g_{ij} > I_{Th}$ occurs (where $i \neq j$), the UEs will be assigned into group 2, which reduces the spatial correlation between them. This process allows the UEs to achieve the highest possible SINR with the minimum transmit power. If the proposed algorithm is used for the case of 32 antenna MU-MIMO, the SINR convergence process in group 2 requires more time and may not converge due to the channel conditions.

3.2.4 Indoor LOS Power Control Evaluation with Static Users

The proposed closed-loop power control (PC) algorithm was implemented on the Ma-MIMO testbed. The TPC update rate was 2 per second for this evaluation using quadrature phase-shift keying (QPSK) with 2-subcarrier redundancy. The upper level of the Merchant Venturers Building atrium at the University of Bristol was used as the test environment with a patch panel

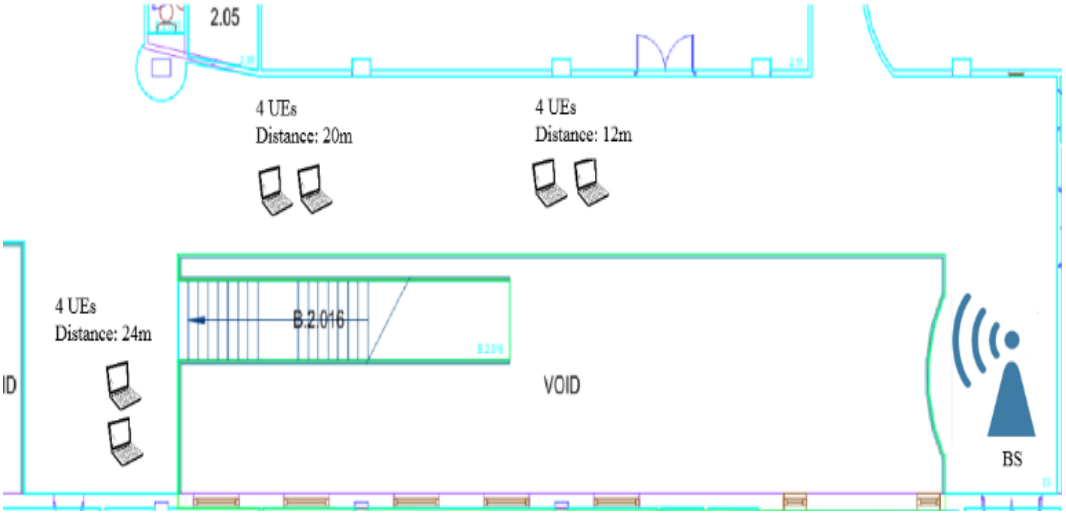

Figure 3.15: UE Distribution within the indoor atrium measurements at Merchant Venturers Building (floor-plan).

antenna array to serve 12 UEs. The array was setup in a 32×4 configuration with alternate H & V polarisations for all 128 antennas. The UEs were in LOS and placed in a straight line with 2.5 wavelength spacing at a 3.51 GHz carrier frequency. However, this environment was not completely static, as it was a normal working day with students and staff present. The UEs were divided into three groups with different distances as shown in Figure 3.15 and Figure 3.16. Each group has 4 UEs and the BS has a 128 element patch antenna array. The environment was changing during channel measurements, although the client devices remained static, and three different PC algorithms were tested. The first and the second PC algorithms are based on a fixed SNR\SINR value, where the BS adjusts the UEs power level to a certain SNR\SINR value. The third PC is the one proposed in section 3.2.2 to maximize the SINR per user and the overall SINR. 800 captures of the channel measurement data were taken. The channel conditions when the fixed SNR PC algorithm was used are illustrated in Figure 3.17 left.

Although the TPC update rate is only 2 times per second, the channel conditions are stable since the ratio between the g_{ii} and g_{ij} is below 20% (where $i \neq j$). When the proposed PC algorithm was used, the UEs increased their power level. The power increment was controlled by the spatial correlation threshold as explained in the adjustment mechanism 3.11. Figure 3.17 right shows the channel conditions associated with the proposed PC algorithm.

The results obtained from the experiment are illustrated in Table 3.2 and Figure 3.17. The average SINR per user and the overall average SINR were saved for the three different PC algorithms. When the BS adjusts the UEs power level to a fixed SNR value, the aggregate average SINR for all the UEs was 5.4 dB. This value was increased by 0.4 dB when the adjustment was based on the SINR. The maximum SINR was achieved when the UEs' power adjustments were based on the proposed PC algorithm. It enhanced the total average SINR by 0.5 dB compared to

Figure 3.16: UE Distribution within the indoor atrium measurements at Merchant Venturers Building.

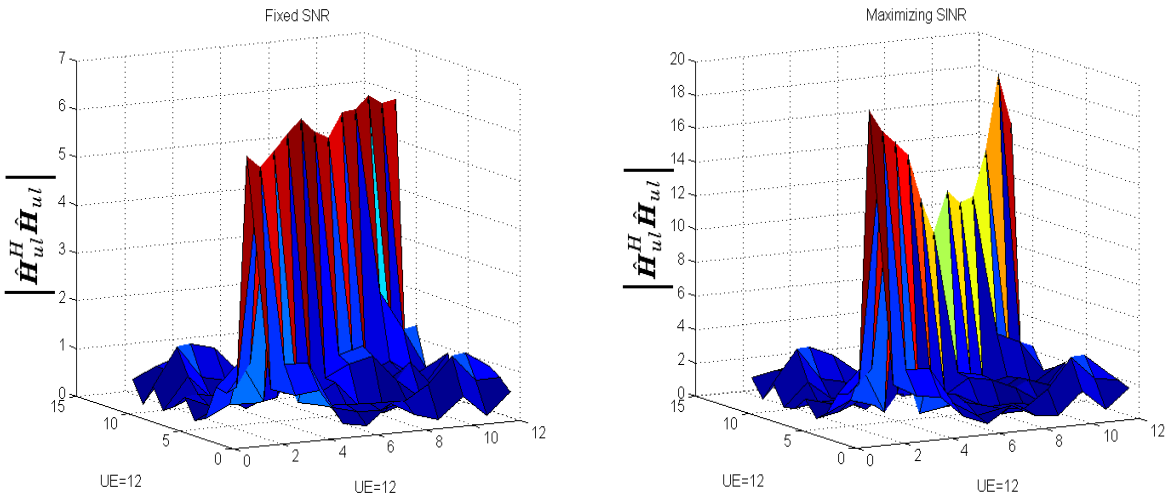

Figure 3.17: Plot $\left|\boldsymbol{H}^H \times \boldsymbol{H}\right|$ for Ma-MIMO, where M=128 and K=12. left, the fixed SNR PC algorithm was used. Right, the proposed PC algorithm was used.

when a fixed SINR was used.

Table 3.2: Aggregate average SINR based on three different PC algorithms.

	Aggregate Average SINR (dB)
PC with fixed SNR	5.4
PC with fixed SINR	5.8
Spatial UL PC for Ma-MIMO	6.3

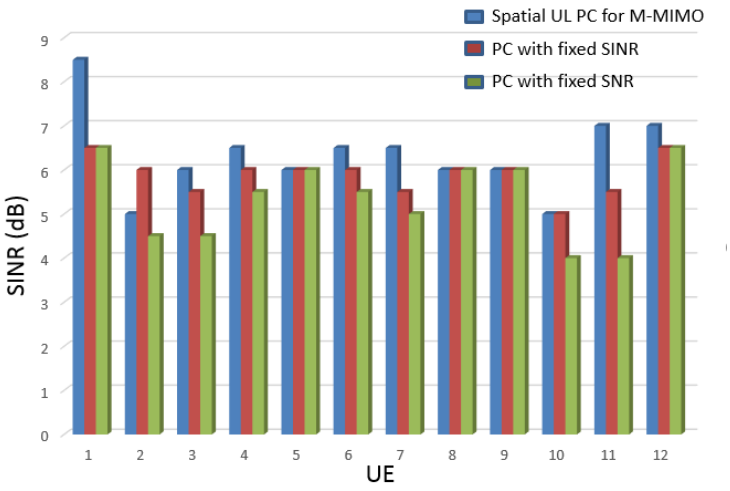

Figure 3.18: The average SINR per user based on three different PC algorithms (Indoor Trial).

3.2.5 LOS Outdoor Power Control Evaluation with Static Users

Following the previous trials, an outdoor experiment took place in the University of Bristol's Merchant Venturers Building Courtyard. Two scenarios were measured in this trial. In the first scenario, 6 USRPs were divided into three groups and the BS has a 128-element patch antenna array as shown Figure 3.19. Only one UE was active from each USRP. In the second scenario, the 6 USRPs were reallocated to group 2 and two UEs were active from each USRP. Starting from this evaluation, the TPC update rate was increased to 10 times per second.

Two different UL PC algorithms were tested in this experiment for both scenarios. The first is the one proposed in section 3.2.2, whilst the second is based on a fixed SNR value (where the BS adjusts the UEs power level to a certain SNR value). The average SINR values per user are illustrated in Figure 3.20 left for the first scenario and in Figure 3.21 for the second scenario. In the first scenario, the aggregate average SINR for all the users achieved by the proposed spatial UL PC algorithm was 12.5 dB and the aggregate average SNR was 14 dB as it is shown in Table 3.3. With a 13 dB SNR UL PC, the aggregate average SINR was 11.6 dB and the aggregate average SNR was 13 dB. Since the aggregate average SNR value from the proposed spatial UL PC was larger than the one obtained from the PC with 13 dB fixed SNR, the SNR reference value was increased to 16.5 dB which increased the aggregate average SNR by 3.5 dB and the aggregate average SINR by 0.9 dB. The average SNRs per user are illustrated in Figure 3.20 right. Since the UEs remained static during the three measurements, the path loss should be the same. Which means the proposed spatial UL PC algorithm decreased the required UL power level by 2.5 dB to achieve an aggregate average SINR of 12.5 dB.

In the second scenario, the aggregate average SINR for the twelve UEs was 5.6 dB when the proposed spatial UL PC was used. This value was decreased by 0.6 dB when the UL power level adjustment was based on an SNR reference level of 11.5 dB. The SNR reference level was

Figure 3.19: Panoramic view of massive MIMO outdoor trial set-up (Merchant Venturers Building Courtyard).

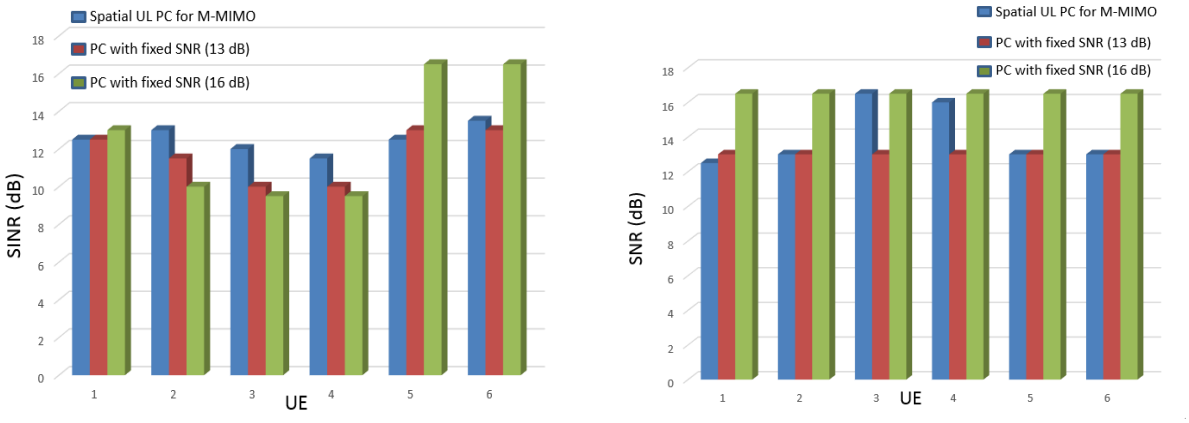

Figure 3.20: Measurements' results based on two different PC algorithms (The 1^{st} scenario of the LOS outdoor trial). Left, the average SINR per user. Right, the average SNR per user.

then increased to 15.5 dB to increase the average SINR. Although the adjustment level was increased by 4 dB, the aggregate average SINR was decreased by 0.2 dB. The reason behind this decrement is the interference added to each user from the other eleven users. The separation distance between the USRPs in the second scenario is small compared to the first one, which led to higher spatial correlation between the 12 UEs. That is, increasing the UL power level might lead to a point where the increment of the aggregate inter-user spatial correlation from all the users would be more than the increment for the received signal power.

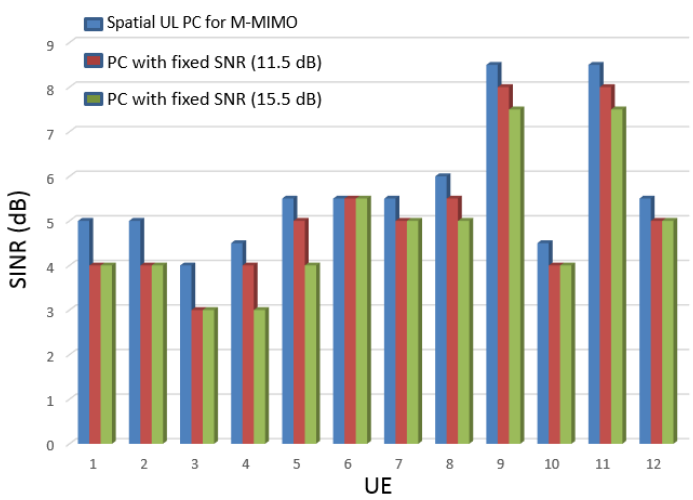

Figure 3.21: The average SINR per user based on two different PC algorithms (The 2^{nd} scenario of the LOS outdoor trial).

Table 3.3: Aggregate average SINR based on two different PC algorithms.

	Aggregate Average SINR (1^{st} scenario)	Aggregate Average SNR (1^{st} scenario)	Aggregate Average SINR (2^{nd} scenario)
Spatial UL PC	12.5 dB	14 dB	5.6 dB
PC with fixed SNR (1^{st} scenario 13 dB, 2^{nd} scenario 11.5)	11.6 dB	13 dB	5 dB
PC with fixed SNR (1^{st} scenario 16 dB, 2^{nd} scenario 15.5)	12.5 dB	16.5 dB	4.8 dB

3.2.6 LOS Outdoor Power Control Evaluation with Mobility

The Lund University Ma-MIMO testbed pictured in Figure 3.22 was used in this evaluation. It is similar to the University of Bristol Ma-MIMO testbed, but with 50 USRPs at the BS providing 100 RF chains. The antenna array shown in Figure 3.22 consists of half-wavelength spaced patch-antennas each with alternate H & V polarisations for all 100 antennas at a 3.7 GHz carrier frequency [3].

3.2.6.1 User Equipment and Synchronisation

As described in section 3.1.5, each USRP provides two users. Three USRPs were mounted on three carts providing six spatial streams (emulating pedestrian behaviour). The dipole antennas

[3]A video of the mobility measurement campaigns at Lund University is available at https://bit.ly/2Ayiikj.

Figure 3.22: Lund Ma-MIMO BS

were attached directly to both RF chains in each USRP with vertical polarization. Additional two USRPs were mounted in two cars for higher levels of mobility, where the antennas were roof mounted with vertical polarization on either side of the car as shown in Figure 3.23. The synchronisation between each UE and the BS was achieved by broadcasting the PSS with static pattern from all antennas as described in section 3.1.5 and the GPS was used to improve the sync stability. The Ma-MIMO BS was setup at the roof of the Faculty of Engineering building. An overview of the setup is shown in Figure 3.24 and Figure 3.25

3.2.6.2 Channel Hardening Evaluation

Theoretical works show that fast-fading disappears by increasing number of antennas at the BS to infinity [22] and [59]. To evaluate the Ma-MIMO channel over time in a dynamic situation and the possibility of relaxing the update rate of power control, a mixture of both pedestrian and vehicular UEs were introduced. The two cars are shown as $C1$ and $C2$ in Figure 3.24 circulating below the maximum $\lambda/2$ measurement speed of 29 km/h. While the two pedestrian carts were static, shown as $P1$ and $P2$. The UL transmission power level was the same from all the UEs.

The arrow in Figure 3.26 shows the movement of one of the cars during 3 seconds duration.

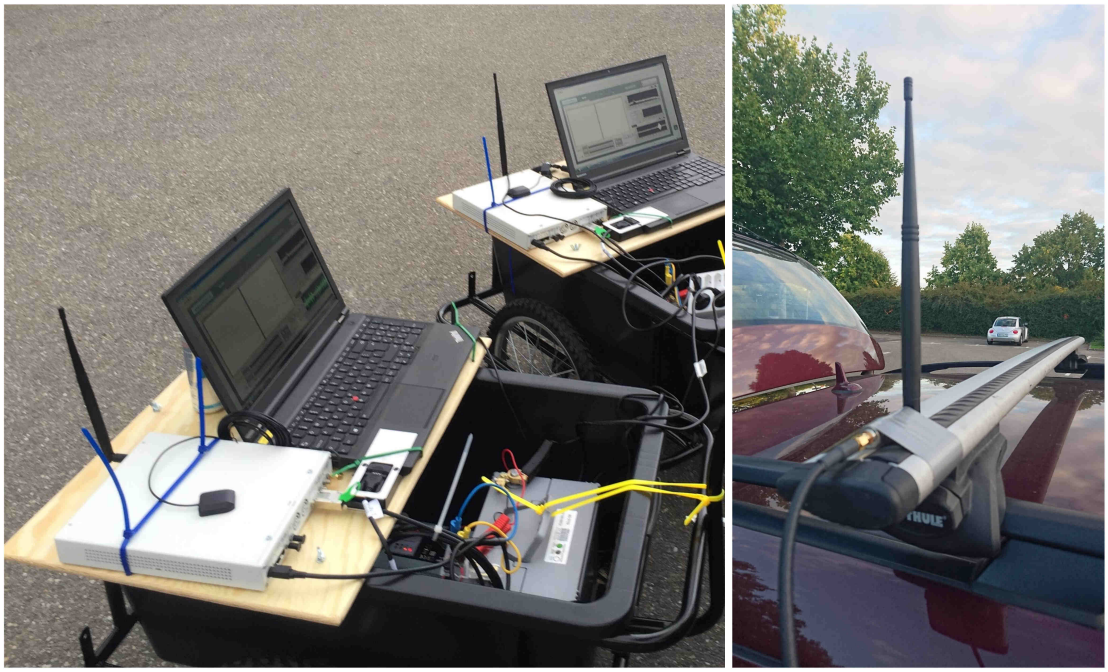

Figure 3.23: User side. Left: pedestrian carts. Right: car mounting.

Figure 3.24: Overview of the mobility trial at the Lund University.

Two different number of antennas at the BS were considered. At first, all the channels were captured from all the 100 antennas. Then the channels of a single vertically polarised antenna was extracted. The relative channel magnitude between one UE in the car and the BS can be

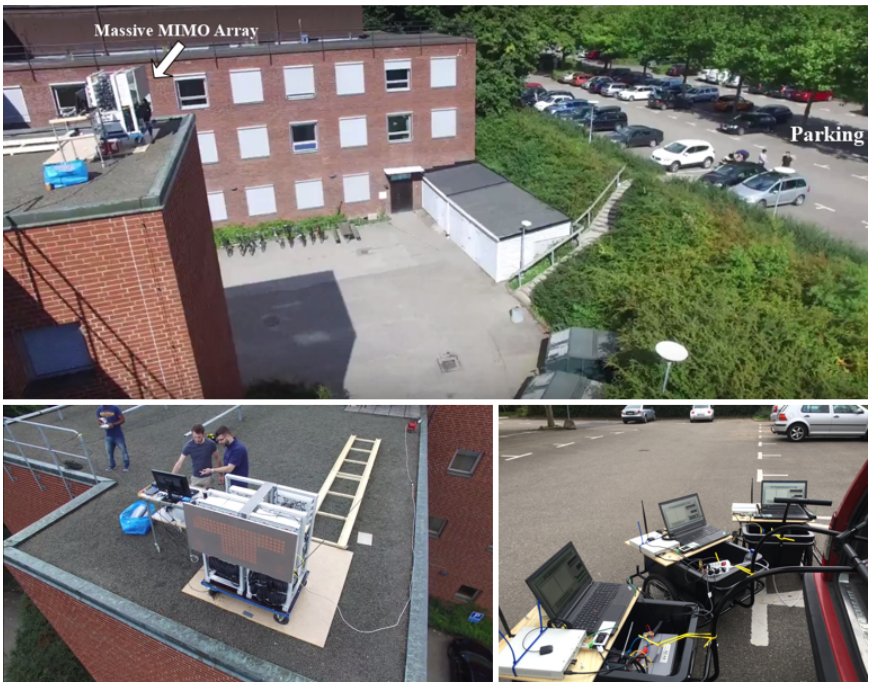

Figure 3.25: Scenario overview: BS position and pedestrian carts

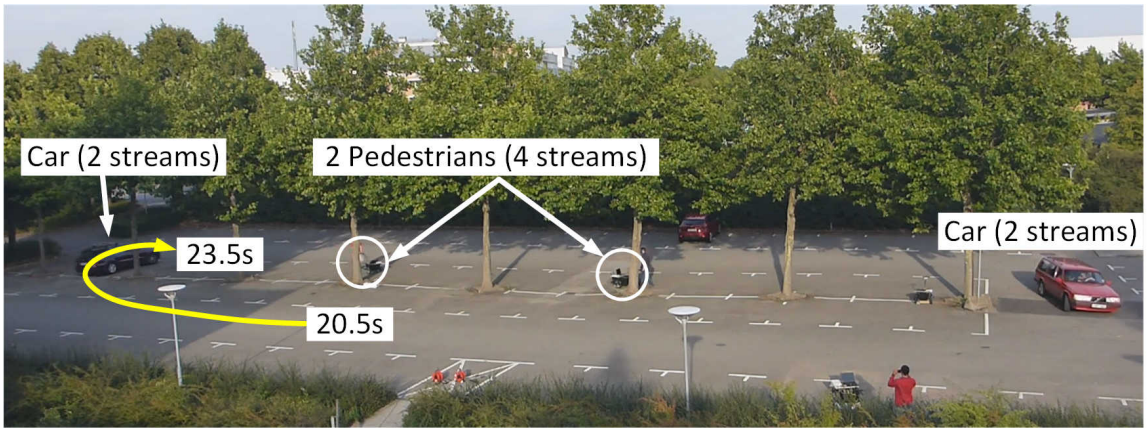

Figure 3.26: View from BS with 3 s car-based user path indicated.

seen in the right of Figure 3.27. The fast fading is clearly seen when a single antenna was used at the BS. By using 100 antennas, the fast fading was smoothed out and large variations were happening over the course of seconds in stead of milliseconds. The power correlation over the time offset is shown in the left of Figure 3.27. By increasing number of antennas to 100, the stability of the power levels was increased so that the power control can be done at least 5 times slower compared to a single antenna. These results demonstrate an improvement in channel robustness for Ma-MIMO and the possibility of relaxing the TPC update rate.

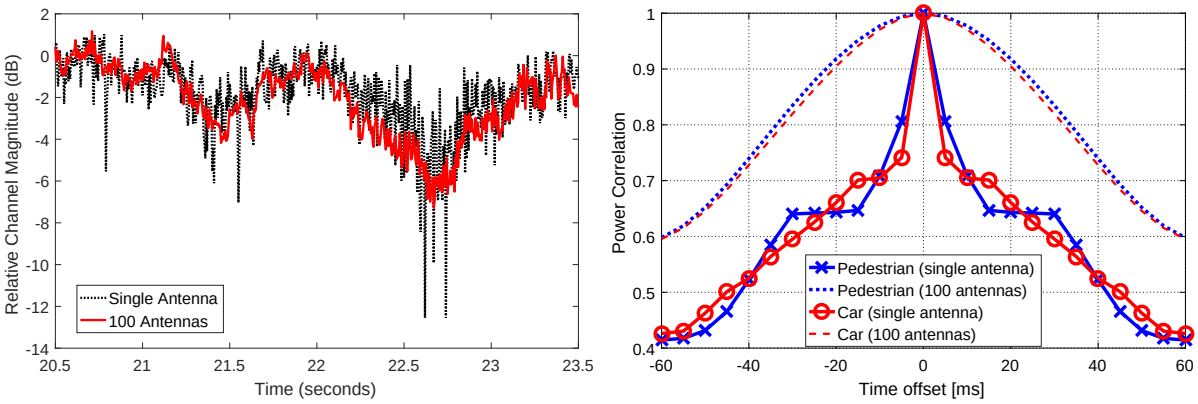

Figure 3.27: Left: relative channel magnitude over the three second period in Figure 3.26. Right: correlation of the power over the same period in Figure 3.26.

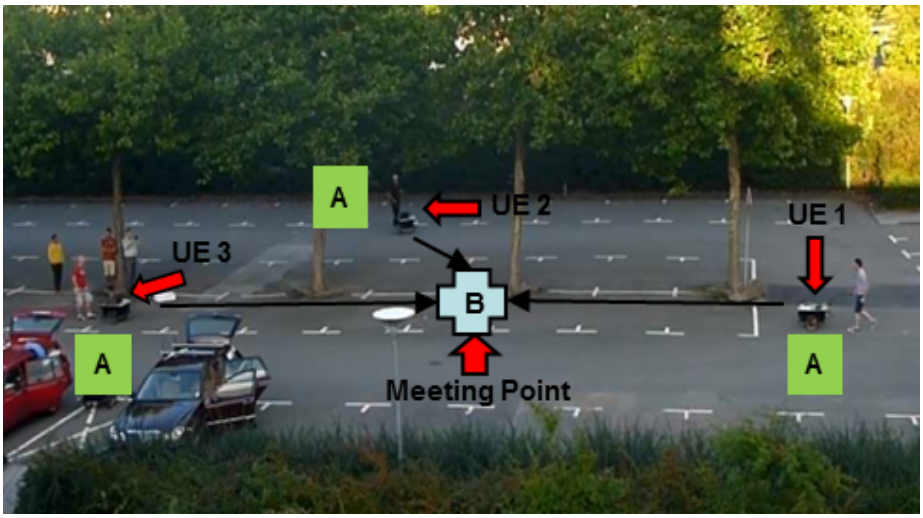

Figure 3.28: View from BS indicating pedestrian movement of equipment

3.2.6.3 PC and Real-time Results

For the results in this section, one user was used from each pedestrian (one active RF chain from each USRP). Three users moved from the starting point A heading towards the meeting point B as illustrated in Figure 3.28. At the starting point A, the aggregate average SINR achieved by the proposed spatial UL PC was equal to the one from the UL PC with a fixed SNR and the aggregate average UL power level was also the same for both as shown in Table 3.4. Figure 3.29 shows the average SINR and the average UL power per user at the starting point A. When the UEs were heading towards the meeting point B, the UL power level was changing according to the TPC commands, with the end results shown in Figure 3.30. At the meeting point B, the aggregate average SINR achieved by the PC with fixed SNR was 3 dB. This value was increased by 2 dB when the proposed spatial UL PC was used to adjust the UL power level. The proposed PC algorithm had also decreased the average UL power by 2.2 dB.

Table 3.4: Aggregate average SINR and UL Gain Level for the trial

	Average SINR		**Average UL Power**	
Location	A	B	A	B
Spatial UL PC	9 dB	5 dB	27 dB	26.8 dB
Spatial PC with fixed SNR (9 dB)	9 dB	3 dB	27 dB	29 dB

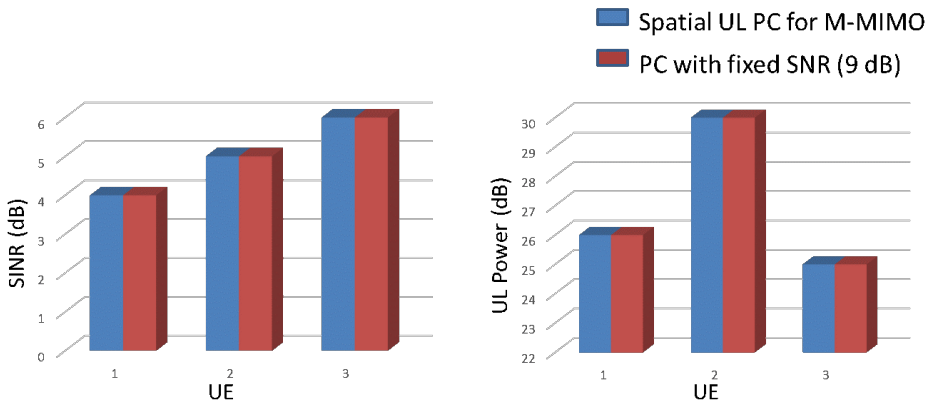

Figure 3.29: Average SINR per user at starting point A for two different PC algorithms

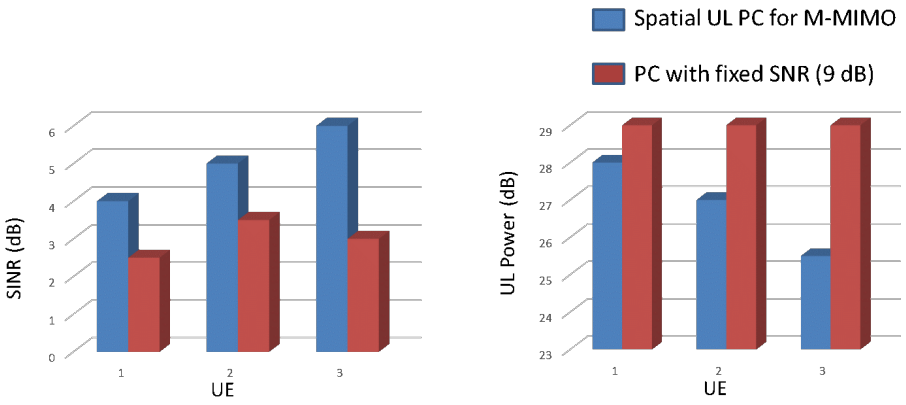

Figure 3.30: Average SINR per user at meeting point B for two different PC algorithms

3.3 Real-time Evaluation for OTA Synchronisation

By broadcasting the PSS using a random static pattern from all antennas as described in section 3.1.5, the phase of the sync signal is generated randomly from each antenna at the BS creating nulls in different locations. This has caused sync losses for the users based on their locations and the sync signal phases from the antennas at the BS. The GPS was used to improve the synchronisation stability for the measurements described in section 3.2.6. To overcome this

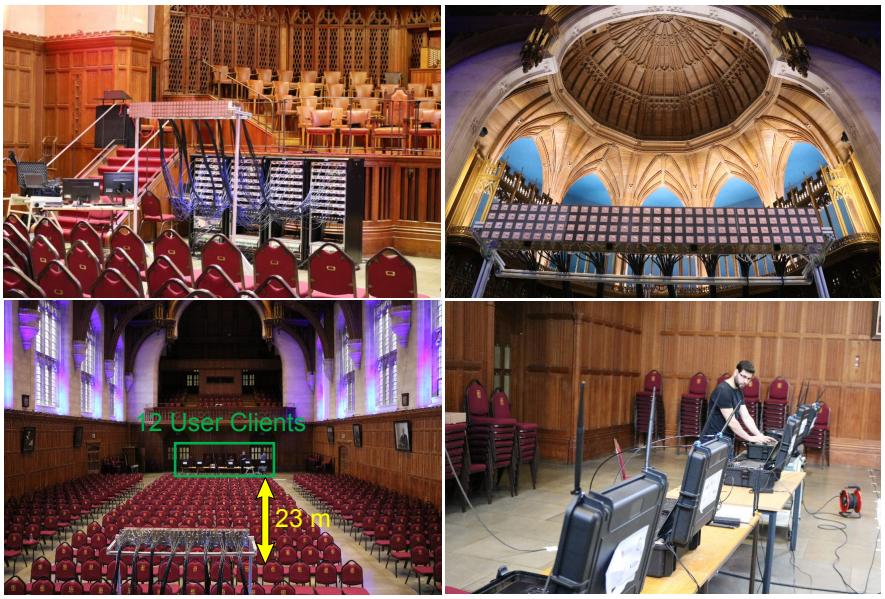

Figure 3.31: Trial environment in the Great Hall of the Wills Memorial Building.

problem, the PSS can be transmitted from a single antenna as described in section 3.1.5. To evaluate the proposed solution, the Ma-MIMO testbed was deployed in the Great Hall of the Wills Memorial Building at the University of Bristol to serve 12 clients places 23 m away on the opposite side of the BS. The array was setup in a 4 × 32 configuration with vertical polarisations for all 128 antenna. The user clients were in LOS and place in a straight line as shown in Figure 3.31. Sync loss counter was added to the system's framework to evaluate the modified synchronisation method. At first, a dipole antenna was used to broadcast the PSS. Then it was replaced by a single patch antenna to focus the energy towards the users as it is shown in Figure 3.32. Two people walked pseudo-randomly during the evaluation, next to the UEs, for 5 minutes duration. This experiment was repeated twelve times (six times for broadcasting the PSS from the single patch antenna and six times for broadcasting the PSS from all the 128 antennas). When the PSS was broadcasted from the single patch antenna, there was no sync loss. But when the PSS was broadcasted from all the 128 antennas, the average sync loss was 9 per second.

The success of using single antenna for synchronisation in this section has led the Ma-MIMO team at the University of Bristol to adopt this method for all the experimental campaigns including the the world's first urban 5G showcase[4].

3.4 Summary

In this chapter, the University of Bristol Ma-MIMO testbed was presented. By using this testbed and the one Lund University has, the channel hardening for Ma-MIMO was evaluated in different

[4]A video about the world's first urban 5G showcase is available at https://www.youtube.com/watch?v=7Qzv_TtyKMU

Figure 3.32: Using an external single antenna for OTA synchronisation.

LOS environments. A spatial UL power control algorithm for Ma-MIMO was proposed which can increase both the EE and the single cell SE. Only a small overhead is required to adjust the transmit power level at the UEs since only two bits are required for the TPC command. By carefully considering the spatial correlation levels provided by the user-side Gram matrix, a maximum SINR can be safely achieved for each UE in the system. It was shown that the sum SINR value was improved, where the majority of the users' SINR value was increased by 1 to 2 dB. However, the SINR value for few users was decreased by 1 dB.

Furthermore, the synchronisation method between user clients and the BS was enhanced by using a single antenna to broadcast the PSS in Ma-MIMO instead of using all antennas with a random static pattern. All the points in this chapter were illustrated experimentally through several indoor, outdoor and mobility Ma-MIMO measurements campaigns with real-time results.

CHAPTER 4

MAXIMIZING SE FOR MASSIVE MIMO AND ITS LIMITS

This chapter evaluates the impact of spatially multiplexing an increasing number of users within a single-cell Ma-MIMO system having real-world practical impairments. The results and conclusions of this chapter have been published in [27], [28] and [31]. The following summarize the main contributions in this chapter:

- Presenting per-cell SE of 145.6 bits/s/Hz achieved with a 128-antenna Ma-MIMO testbed and introducing the challenges and the limiting factors when increasing the SE value in that trial.
- Showing and illustrating that for realistic performance the sum SE should be calculated based on the EVM performance of the composite transceiver (TRX) equipment and each spatial channel instead of using Shannon capacity calculations. As opposed to the results obtained using Shannon capacity, it is shown that the maximum sum SE with practical number of antennas could be achieved by decreasing the number of users before the sum SE reached its peak value.
- Showing that the inaccurate UL CSI has greater impact on the DL data transmission than it is on the UL data transmission due to the error amplification caused by the reciprocity calibration matrix.
- Showing that by using ZF or MMSE, a lower number of antennas at the BS with high hardware quality could be better than increasing the number of antennas and reducing the hardware quality.
- Validating all the above points experimentally with real-time results using a software-defined radio Ma-MIMO testbed.

Accurate CSI is crucial for correct MU MIMO operation [22]. Numerous academic papers have investigated the effect of inaccurate CSI in Ma-MIMO. The work in [107] illustrates the impact of hardware impairments for the DL of a single cell with different channel conditions. It shows how the number of BS antenna elements and their spacings can affect the EVM at the UE side. The hardware impairment impact for a single-cell scenario was addressed in [108]. This paper shows how the number of antennas affects the average sum rate with different channel models. The effect of imperfect channel reciprocity and CSI error was also covered in [109] for DL transmissions. The paper introduced a model that considers the impact of RF mismatches on the linear precoding for a TDD Ma-MIMO system. The relationship between the output SINR and the amplitude error variance were illustrated for ZF and MF. The impact of inaccurate CSI in a single-cell for both UL and DL was covered in [68]. The impact of non-ideal hardware on the capacity limits was covered in [110] for both UL and DL in a multi-cell scenario. It shows how the pilot length and the number of antennas at the BS are affected by the relative estimation error per antenna. The multi-cell scenario was then covered in [111] for both UL and DL. It shows how the number of antennas, pilot allocation and hardware impairments affects the spectral efficiency.

Although some research has investigated the impact of inaccurate CSI in Ma-MIMO performance, some topics need further investigation. Firstly, the approaches used to calculate the sum SE are based on Shannon capacity calculations and by using a very large number of antennas at the BS. These approaches show that there is a peak value for sum SE achieved by serving a certain number of users. Here, until the sum SE reaches its peak value, the maximum sum SE is achieved by serving all users simultaneously. However in a real-time Ma-MIMO system, these approaches are not applicable and do not consider using different MCS orders. Although the Truncated Shannon Bound method considers using different MCS [112], it won't be applicable to use this method in real-time Ma-MIMO system since it relies on the SINR values as shown later is section 5.1.1. Secondly, most of the imperfect channel reciprocity work assumes accurate UL CSI which can't be acquired in reality. Thirdly, most available results are based on IID channels and do not cover SE comparison between different decoders/precoders for UL and DL data transmission with a practical number of antennas at the BS. Lastly, there is no publicly available work on experientially validating the impact of inaccurate CSI on Ma-MIMO performance. As the theoretical work proposed that increasing number of antennas at the BS decreases the interference caused by inaccurate CSI and from the channel itself, no validation has been published. Several Ma-MIMO trials have conducted as a proof of concept. Thus, the need for validation is high, as the industry needs to fully understand the trade-off between number of antennas (cost) and system performance.

This chapter is structured as follows. Section 4.1 presents the highest spectral efficiency achieved for any wireless system to date and introduces the challenges and the limiting factors. Section 4.2 presents the system models. Section 4.3 shows the impact of adding more users on

Ma-MIMO performance with inaccurate CSI in UL data transmission by using MF, ZF and MMSE. Section 4.4 shows how the reciprocity calibration error is affected by the UL CSI accuracy and the impact of adding more users in DL data transmission. Section 4.5 shows the difference between using Shannon capacity calculations and the EVM performance on maximizing the sum SE with IID and real-channel. Section 4.6 provides a comparison between adding more antennas at the BS and building hardware with better quality. Section 4.7 validates all the points raised in sections 4.3, 4.4, 4.5 and 4.6 experimentally. Lastly, Section 4.8 summarizes the key results from this work.

4.1 Serving 22 Users in Real-Time with Massive MIMO and its limits

4.1.1 Measurement Environment

The upper level of the Merchant Venturers Building atrium at the University of Bristol was used as the test environment with a patch panel antenna array to serve 22 user clients placed 24.8m away on the opposite balcony. The array was setup in a 32×4 configuration with alternate H & V polarisations for all 128 antennas. The UEs were in LOS and placed in a straight line with 2.5 wavelength spacing at a 3.51 GHz carrier frequency. However, this environment was not completely static, as it was a normal working day with students and staff present. An overview of the setup can be seen in Figure 4.1.

4.1.2 System Configuration

The system was configured using the frame schedule described in section 3.1.3 and the synchronisation between each UE and the BS was achieved via cables as described in section 3.1.5. The channel estimation was performed in 5ms intervals, and all remaining slots were assigned for UL data with a 256-QAM modulation scheme (MS). ZF detection was used for all throughput measurements and equal transmit power was applied for all UEs. 100 channel data captures were recorded to disk at an interval of approximately 200ms, resulting in a total measurement period of approximately 3 minutes.

4.1.3 Outcomes and Limitations

In real-time it was possible to connect 22 users with 256-QAM and obtain the decoded UL constellations shown in Figure 4.2 using 128 bit complex floating point processing. The absolute throughput could not be measured for 22 users as only decimated host detection was performed, but by observing the clarity of the constellations and the degree of spatial orthogonality achieved, an appropriate estimation could be made. 22 UEs were successfully served, which would equate to 145.6 bits/s/Hz using the frame schedule in [31]. This is a record reported result for spectral

Figure 4.1: Measurement trial with the UEs 24.8m away (the upper level of the Merchant Venturers Building atrium at the University of Bristol).

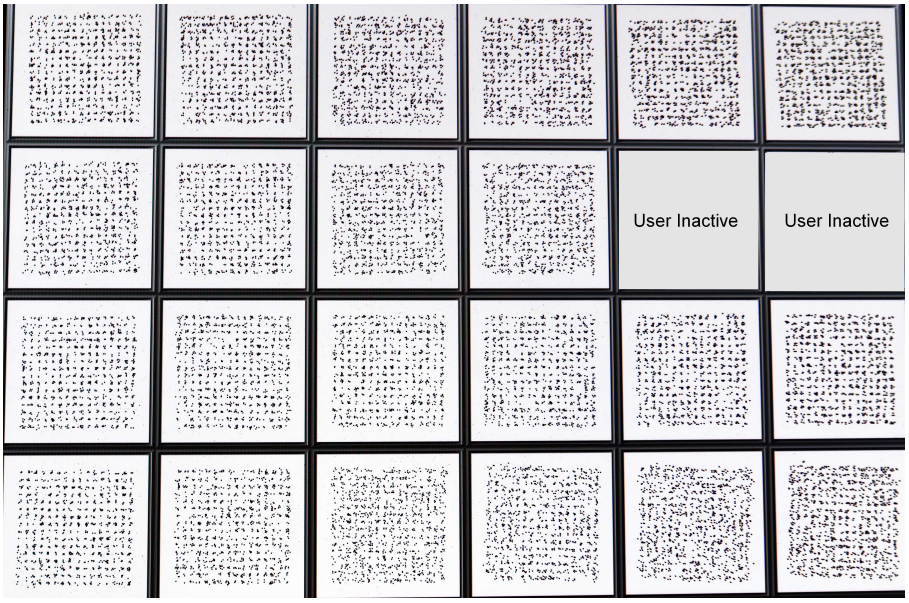

Figure 4.2: 256-QAM UL constellations from 22 UEs with 50cm client separation (the upper level of the Merchant Venturers Building atrium at the University of Bristol).

efficiency [113] and truly demonstrates the tremendous potential of Ma-MIMO technology for improving system throughput without bandwidth expansion [41].

Connecting a 23^{rd} user caused significant degradation in the constellation quality and the physical location of this additional user within the line of 24 UEs (see Figure 4.2) had no impact. This is because all users were clustered as shown in Figure 4.1 and have the same SNR value. Therefore, it is believed this could be related to the CSI accuracy introduced in [68]. Further analysis through trials and simulations is now provided in this chapter to investigate the impact of inaccurate CSI and number of UEs on Ma-MIMO performance. Different users distribution is covered in Appendix C.

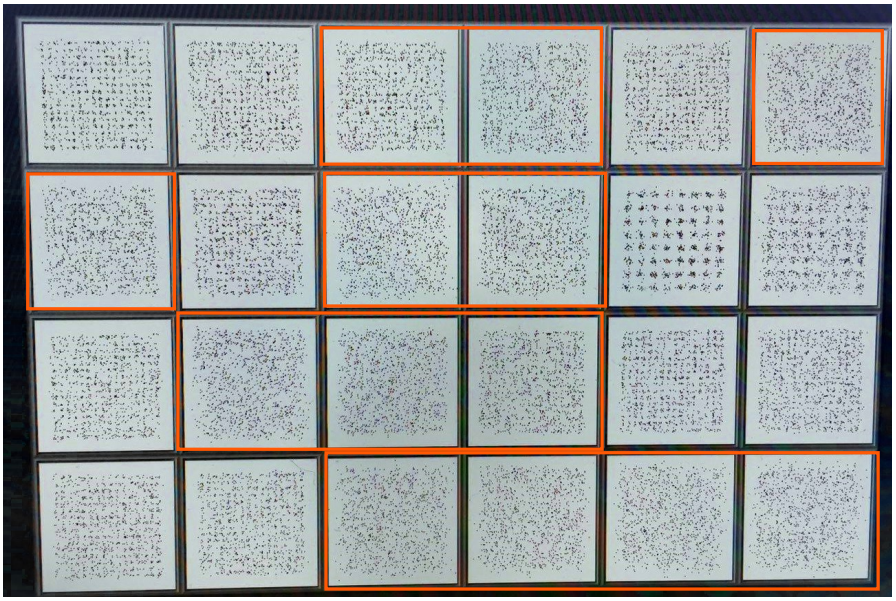

Figure 4.3: 256-QAM UL constellations from 24 UEs with 50cm client separation. High EVM values can be observed from the constellations in the orange collared rectangular compared to the one in the Figure 4.2.

4.2 System Model

A single-cell Ma-MIMO architecture with imperfect CSI is considered in this chapter. Each UE transmits a frequency-orthogonal UL pilot for the channel estimation. The actual UL channel matrix during the uplink data transmission is denoted by $\boldsymbol{H}_{ul} \in \mathbb{C}^{M \times K}$, which is given by

$$\boldsymbol{H}_{ul} = \hat{\boldsymbol{H}}_{ul} + \boldsymbol{E}_{ul} \tag{4.1}$$

where $\boldsymbol{E}_{ul} \in \mathbb{C}^{M \times K}$ is the difference between the estimated channel and the actual channel during the uplink data transmission. This error could be caused by hardware impairments, interpolation across frequency, large-scale channel attenuation and any other potential sources. In this chapter the error in the UL channel estimation between the UE and the BS is modeled as a complex Gaussian distribution $\sim \mathscr{CN}\left(\mathbf{0}, \sigma_e^2 \boldsymbol{I}_M\right)$, where σ_e^2 is the error variance [114]. Whilst this model may not be so accurate in reality, it serves to illustrate the potential effects of UL CSI inaccuracies in Ma-MIMO. The equalized UL signal $\hat{\boldsymbol{x}} \in \mathbb{C}^{\mathbb{K}}$ can be expressed as

$$\hat{\boldsymbol{x}} = \boldsymbol{W}\left(\sqrt{\rho_{ul}}\boldsymbol{H}_{ul}\boldsymbol{x} + \boldsymbol{n}_{BS}\right) \tag{4.2}$$

where ρ_{ul} is the corresponding UL transmit power. Simple UL power control is assumed in this chapter. The UL transmit power is adjusted so the received SNR from all users is the same. The additive noise vector in UL is denoted by $\boldsymbol{n}_{BS}$. The noise variance from the antennas at the BS is modeled as $\sim \mathscr{CN}\left(\mathbf{0}, \sigma_{n_{BS}}^2 \boldsymbol{I}_M\right)$, where $\sigma_{n_{BS}}^2$ is the noise variance.

While it is generally agreed that the propagation channel is reciprocal in time [115], the transceiver radio frequency (RF) chains at both ends of the link are generally not [72]. Therefore,

the actual DL channel matrix during the DL data transmission is denoted by $\boldsymbol{H}_{dl} \in \mathbb{C}^{K \times M}$. The estimated DL channel matrix $\hat{\boldsymbol{H}}_{dl} \in \mathbb{C}^{K \times M}$ and how it is affected by $\hat{\boldsymbol{H}}_{ul}$ are covered in section 4.4. The received downlink signal $\hat{\boldsymbol{s}} \in \mathbb{C}^{\mathbb{K}}$ can be written as

$$\hat{\boldsymbol{s}} = \sqrt{\rho_{dl}} \boldsymbol{H}_{dl} \boldsymbol{P} \boldsymbol{s} + \boldsymbol{n}_{UE} \tag{4.3}$$

where $\boldsymbol{s}$ represents the transmitted symbol vector from the BS to users in the same cell, normalized as $\mathbb{E}\{|s_k|^2\} = 1$. The corresponding DL transmit power is denoted by ρ_{dl}. $\boldsymbol{P} \in \mathbb{C}^{M \times K}$ is the linear precoder matrix, formed by using MMSE, ZF or MF. $\boldsymbol{n}_{UE}$ is the additive noise vector in DL. The noise variance from the users' antenna is modeled as $\sim \mathscr{CN}\left(\boldsymbol{0}, \sigma^2_{n_{UE}} \boldsymbol{I}_K\right)$, where $\sigma^2_{n_{UE}}$ is the noise variance.

4.3 Accumulation of Error Amplification in UL

With imperfect channel estimation the error in equation 4.1 will always be added to the estimated channel. In sections 4.3.1, 4.3.2 and 4.3.3, the impact of adding users with inaccurate CSI is explained for MF, ZF and MMSE respectively in the UL. From equation(4.2), the equalized signal vector can be written as follows:

$$\begin{aligned} \hat{\boldsymbol{x}} &= \sqrt{\rho_{ul}} \boldsymbol{W} \boldsymbol{H}_{ul} \boldsymbol{x} + \boldsymbol{W} \boldsymbol{n}_{BS} \\ &= \sqrt{\rho_{ul}} \left(\boldsymbol{W} \boldsymbol{E}_{ul} + \boldsymbol{W} \hat{\boldsymbol{H}}_{ul} \right) \boldsymbol{x} + \boldsymbol{W} \boldsymbol{n}_{BS} \\ &= \sqrt{\rho_{ul}} \boldsymbol{W} \boldsymbol{E}_{ul} \boldsymbol{x} + \sqrt{\rho_{ul}} \boldsymbol{W} \hat{\boldsymbol{H}}_{ul} \boldsymbol{x} + \boldsymbol{W} \boldsymbol{n}_{BS} \end{aligned} \tag{4.4}$$

The number of users affect the actual equalized signal for the target user k. This can be shown by rearranging equation (4.4) as follows

$$\hat{x}_k = \underbrace{\sqrt{\rho_{ul_k}} \sum_{i=1}^{K} (\boldsymbol{W} \boldsymbol{E}_{ul})_{k,i} x_i}_{\text{Cumulative Error}} + \overbrace{\sqrt{\rho_{ul_k}} \sum_{i=1}^{K} \left(\boldsymbol{W} \hat{\boldsymbol{H}}_{ul} \right)_{k,i} x_i + z_k}^{\text{Desired Signal+Interference}} \tag{4.5}$$

where z_k is the amplified noise for user k caused by the decoder. The "Cumulative Error" part represents the interference introduced by CSI estimation inaccuracies. The "Desired Signal + Interference" part consists of the UL transmitted symbol from user k and the interference caused by the inter-user spatial correlation.

4.3.1 Match Filter Receiver

To cover the impact of inaccurate CSI, the MF decoder used in section 2.2.3.1 can be rewritten as $\boldsymbol{W} = \hat{\boldsymbol{H}}^H_{ul}$. The equalized received signal from user k can be written as follows:

$$\hat{x}_k = \underbrace{\sqrt{\rho_{ul}} \sum_{i=1}^{K} \left(\hat{\boldsymbol{H}}^H_{ul} \boldsymbol{E}_{ul} \right)_{k,i} x_i}_{\text{Cumulative Error}} + \overbrace{\sqrt{\rho_{ul}} \sum_{i=1}^{K} \left(\hat{\boldsymbol{H}}^H_{ul} \hat{\boldsymbol{H}}_{ul} \right)_{k,i} x_i + z_k}^{\text{Desired Signal + Interference}} \tag{4.6}$$

By increasing the number of antennas at the BS, the ratio between diagonal elements and non-diagonal elements of the Gram matrix $\boldsymbol{G} = \hat{\boldsymbol{H}}_{ul}^{H}\hat{\boldsymbol{H}}_{ul}$ will also increase. This is known as the channel hardening effect as previously explained in chapter 2 and demonstrated in chapter 3. The "Desired Signal + Interference" part is extremely sensitive upon the number of antennas at the BS. The "Cumulative Error" part is less impacted by the number of antennas since the matrix elements resulting from the matrix multiplication of $\left(\hat{\boldsymbol{H}}_{ul}^{H}\boldsymbol{E}_{ul}\right)$ are far smaller than the channel Gram matrix when UL power control is applied. The interference from both parts is increased by increasing the number of users.

4.3.2 Zero Forcing Receiver

To cover the impact of inaccurate CSI, the ZF decoder used in section 2.2.3.2 can be rewritten as $\boldsymbol{W} = \left(\hat{\boldsymbol{H}}_{ul}^{H}\hat{\boldsymbol{H}}_{ul}\right)^{-1}\hat{\boldsymbol{H}}_{ul}^{H}$. The equalized received signal from user k can be written as follows:

$$\hat{x}_k = \underbrace{\sqrt{\rho_{ul_k}}\sum_{i=1}^{K}\left(\left(\left(\hat{\boldsymbol{H}}_{ul}^{H}\hat{\boldsymbol{H}}_{ul}\right)^{-1}\hat{\boldsymbol{H}}_{ul}^{H}\boldsymbol{E}_{ul}\right)_{k,i}x_i\right)}_{\text{Cumulative Error}} + \sqrt{\rho_{ul_k}}x_i + z_k \tag{4.7}$$

Unlike MF, the interference is only caused from the "Cumulative Error" part which is introduced by CSI estimation inaccuracies. This interference is increased by increasing number of users. Similar to MF, the channel Gram matrix impacts the interference value. Although ZF suppresses the interference from the estimated channel between users, it amplifies the interference introduced by the inaccurate CSI. This interference is caused by the inverse of the channel Gram matrix in the "Cumulative Error" part. Although the value of this part in ZF is larger than the one in MF, the overall interference in MF is still higher than that of ZF.

4.3.3 Minimum Mean Square Error Receiver

To cover the impact of inaccurate CSI, the MMSE decoder used in section 2.2.3.3 can be rewritten as $\boldsymbol{W} = \left(\hat{\boldsymbol{H}}_{ul}^{H}\hat{\boldsymbol{H}}_{ul} + \frac{1}{\gamma}\boldsymbol{I}\right)^{-1}\hat{\boldsymbol{H}}_{ul}^{H}$. The equalized received signal from user k can be written as follows:

$$\hat{x}_k = \overbrace{\sqrt{\rho_{ul_k}}\sum_{i=1}^{K}\left(\left(\left(\hat{\boldsymbol{H}}_{ul}^{H}\hat{\boldsymbol{H}}_{ul} + \frac{1}{\gamma}\boldsymbol{I}\right)^{-1}\hat{\boldsymbol{H}}_{ul}^{H}\boldsymbol{E}_{ul}\right)_{k,i}x_i\right)}^{\text{Cumulative Error}} + \underbrace{\sqrt{\rho_{ul}}\sum_{i=1}^{K}\left(\left(\hat{\boldsymbol{H}}_{ul}^{H}\hat{\boldsymbol{H}}_{ul} + \frac{1}{\gamma}\boldsymbol{I}\right)^{-1}\hat{\boldsymbol{H}}_{ul}^{H}\hat{\boldsymbol{H}}_{ul}\right)_{k,i}x_i}_{\text{Desired Signal + Interference}} + z_k \tag{4.8}$$

The interference and the cumulative error parts are highly affected by the SNR value and the number of users. With a low SNR value, MMSE is less affected by the CSI accuracy as it operates similar to MF. While with a high SNR value, MMSE becomes more sensitive to CSI accuracy as it operates similar to ZF.

4.4 Imperfect Channel Reciprocity and Accumulation of Error Amplification in DL

Channel reciprocity is essential for DL data transmission in a Ma-MIMO TDD system. Not only propagation conditions determine the radio channel, but also the transceiver front-ends at both sides of the radio link. Since different transceiver chains are used at the BS and the UE, the actual downlink channel $\boldsymbol{h}_{dl} \in \mathbb{C}^{1\times \mathrm{M}}$ between the BS and one user can be written as follows:

$$\boldsymbol{h}_{dl} = \boldsymbol{h}_{ul}^{T}\boldsymbol{D}_b \tag{4.9}$$

Where $\boldsymbol{D}_b = diag(cb_1,...,cb_M)$ is the calibration matrix and b_i is the calibration coefficient [110]. The estimated calibrated version of the downlink channel $\hat{\boldsymbol{h}}_{dl} \in \mathbb{C}^{1\times M}$ between one user and the BS can be written as follows:

$$\hat{\boldsymbol{h}}_{dl} = \hat{\boldsymbol{h}}_{ul}^{T}\hat{\boldsymbol{D}}_b \tag{4.10}$$

Where $\hat{\boldsymbol{D}}_b = diag\left(\hat{b}_1,...,\hat{b}_M\right)$ is the estimated calibration matrix. $\hat{b}_i = c(b_i + e_i)$ is the estimated calibration coefficient where e_i is an IID random process representing the calibration error and c is the unknown common scaling factor. From equations (4.1), (4.9) and (4.10), the actual downlink channel $\boldsymbol{h}_{dl}$ between the BS and one user can be written as follows:

$$\begin{aligned}
\boldsymbol{h}_{dl} - \hat{\boldsymbol{h}}_{dl} &= \boldsymbol{h}_{ul}^{T}\boldsymbol{D}_b - \hat{\boldsymbol{h}}_{ul}^{T}\hat{\boldsymbol{D}}_b \\
\boldsymbol{h}_{dl} &= \hat{\boldsymbol{h}}_{dl} + \left(\hat{\boldsymbol{h}}_{ul}^{T} + \boldsymbol{e}_{ul}^{T}\right)\boldsymbol{D}_b - \hat{\boldsymbol{h}}_{ul}^{T}\hat{\boldsymbol{D}}_b \\
\boldsymbol{h}_{dl} &= \hat{\boldsymbol{h}}_{dl} + \hat{\boldsymbol{h}}_{ul}^{T}\left(\boldsymbol{D}_b - \hat{\boldsymbol{D}}_b\right) + \boldsymbol{e}_{ul}^{T}\boldsymbol{D}_b \\
\boldsymbol{h}_{dl} &= \hat{\boldsymbol{h}}_{dl} + \hat{\boldsymbol{h}}_{ul}^{T}\boldsymbol{E}_b + \boldsymbol{e}_{ul}^{T}\boldsymbol{D}_b \\
\boldsymbol{h}_{dl} &= \hat{\boldsymbol{h}}_{dl} + \boldsymbol{e}_{dl}
\end{aligned} \tag{4.11}$$

where

$$\boldsymbol{e}_{dl} = \hat{\boldsymbol{h}}_{ul}^{T}\boldsymbol{E}_b + \boldsymbol{e}_{ul}^{T}\boldsymbol{D}_b \tag{4.12}$$

$\boldsymbol{E}_b = diag(-ce_1,...,-ce_M)$ is the calibration error matrix. From equation (4.11), the downlink channel matrix $\boldsymbol{H}_{dl} \in \mathbb{C}^{K\times M}$ between the BS and the UEs can be decomposed as follows:

$$\boldsymbol{H}_{dl} = \hat{\boldsymbol{H}}_{dl} + \boldsymbol{E}_{dl} \tag{4.13}$$

where $\hat{\boldsymbol{H}}_{dl} \in \mathbb{C}^{K\times M}$ is the estimated calibrated version of the downlink channel matrix between the UEs and the BS, while $\boldsymbol{E}_{dl} \in \mathbb{C}^{K\times M}$ is the difference between the estimated calibrated channel and the actual channel during the downlink transmission.

The UL CSI accuracy has greater impact on increasing the difference between the estimated calibrated channel and the actual channel during the downlink transmission than it has on increasing the difference between the estimated channel and the actual channel during the uplink

data transmission. This can be seen in equation (4.12) where the error introduced by inaccurate UL CSI ($\boldsymbol{e}_{ul}$) is multiplied by the calibration matrix ($\boldsymbol{D}_b$). That means the difference between the estimated calibrated channel and the actual channel during the downlink transmission could vary with different Ma-MIMO hardware using the same reciprocity calibration algorithm and the same radio prorogation environment due to varying the hardware impairment. This was experimentally validated in section 4.7. The hardware impairment error value in DL data transmission is greater than that in UL data transmission. This can be seen in equation (4.12) where the calibrated DL CSI error is composed from multiplying the UL CSI error to the calibration matrix then adding the multiplication result of the estimated UL CSI to the calibration error matrix. The received signal in DL can be written from equations (4.3) and (4.13) as follows:

$$\begin{aligned}\hat{\boldsymbol{s}} &= \sqrt{\rho_{dl}}\boldsymbol{H}_{dl}\boldsymbol{P}\boldsymbol{s} + \boldsymbol{n}_{UE} \\ &= \sqrt{\rho_{dl}}\left(\boldsymbol{E}_{dl}\boldsymbol{P} + \hat{\boldsymbol{H}}_{dl}\boldsymbol{P}\right)\boldsymbol{s} + \boldsymbol{n}_{UE} \\ &= \sqrt{\rho_{dl}}\boldsymbol{E}_{dl}\boldsymbol{P}\boldsymbol{s} + \sqrt{\rho_{dl}}\hat{\boldsymbol{H}}_{dl}\boldsymbol{P}\boldsymbol{s} + \boldsymbol{n}_{UE}\end{aligned} \tag{4.14}$$

By rearranging the above equation, the received signal for user k can be written as follows:

$$\hat{s}_k = \underbrace{\sqrt{\rho_{dl_k}}\sum_{i=1}^{K}\left(\boldsymbol{E}_{dl}\boldsymbol{P}\right)_{k,i}s_i}_{\text{Cumulative Error}} + \overbrace{\sqrt{\rho_{dl_k}}\sum_{i=1}^{K}\left(\hat{\boldsymbol{H}}_{dl}\boldsymbol{P}\right)_{k,i}\boldsymbol{s}_i}^{\text{Desired Signal+Interference}} + n_{UE_k} \tag{4.15}$$

$$where \qquad \boldsymbol{P} = \begin{cases} \hat{\boldsymbol{H}}_{dl} & MF \\ \left(\hat{\boldsymbol{H}}_{dl}\hat{\boldsymbol{H}}_{dl}^{H}\right)^{-1}\hat{\boldsymbol{H}}_{dl} & ZF \\ \left(\hat{\boldsymbol{H}}_{dl}\hat{\boldsymbol{H}}_{dl}^{H} + \frac{1}{\gamma}\boldsymbol{I}\right)^{-1}\hat{\boldsymbol{H}}_{dl} & MMSE \end{cases}$$

Since $\boldsymbol{E}_{dl} > \boldsymbol{E}_{ul}$, the interference caused by the "Cumulative Error" part in DL data transmission from equation (4.14) is greater than the one caused in UL data transmission from equation (4.4). Therefore, adding more users increases the interference between users in DL data transmission more than for UL data transmission. So the sum SE achieved in UL data transmission is greater than that in DL data transmission. This was experimentally validated in section 4.7.

4.5 Spectral Efficiency Evaluation

Two different scenarios were considered to evaluate the Ma-MIMO performance for differing numbers of users when CSI errors are present. An IID Rayleigh channel is used in the first scenario, where M=128 and K is an even number $\in [2, 22]$. In the second scenario, the real channel captured from the trial described in section 4.1 was used. These scenarios were run through an UL Ma-MIMO simulator developed at the University of Bristol. In addition to randomly generated channels, new vectors can be transmitted through channels previously captured by the physical system for more extensive analysis. For both scenarios in this section, the error in the

channel estimation between the UEs and the BS is modeled as a complex Gaussian distribution $\sim \mathscr{CN}\left(\mathbf{0}, \sigma_e^2 \boldsymbol{I}_M\right)$ [114] where an error variance of 0.01 (1%) was used for the simulations shown. Whilst this value may be higher or lower and the model could not be so accurate in reality, it serves to illustrate the potential effects of CSI inaccuracies in Ma-MIMO. Simulation results with different error variance are covered in section 4.6 while real-time results are covered in section 4.7.

4.5.1 Minimising Inter-User Correlation

In this chapter, the users were introduced in an order where the least overall correlation is considered first to minimize the IUI damage with each step. This provides a fair comparison between the theoretical evaluation method in section 4.5.2 and the practical evaluation method in section 4.5.3. Algorithm 1 describes the full procedure which operates in two stages upon the absolute values of the user side Gramian matrix calculated in equation 3.4. $\mathscr{L}$ is a vector of size K which contains the user IDs, where $\mathscr{L}_1$ and $\mathscr{L}_K$ are the first and last users respectively introduced to the system. In the first stage, users with the lowest spatial correlation are added to the system. This can be found by searching for the minimum value of the off-diagonal elements in $\boldsymbol{G}$. Following this, the second stage considers the mean correlation between the currently ordered users in $\mathscr{L}_1$ and the remaining users that have not yet been added to $\mathscr{L}$.

4.5.2 Theoretical Evaluation

Figure 4.4 shows SE comparison between the 1st and the 2nd scenario as the number of active users increases across an SNR range of $0-50$ dB for both ZF and MF algorithms. The sub-plots in the first row show the median achievable SE per user by using ZF and MF for both scenarios. Their equivalent sum SE are the sub-plots in the second row. The median per user SE is always 16.59 bits/s/Hz at 50 dB SNR in case of one active user since there is no interference source. For ZF it can be seen in (a) and (b) that a median per user spectral efficiency of greater than 4 bits/s/Hz can always be maintained at 30 dB SNR. Increasing the SNR beyond 30 dB improves lower numbers of active users, but plateaus at 4.89 bits/s/Hz in (a) and 4.219 bits/s/Hz in (b) for 22 users at 40 dB SNR. Sub-plot (e) and (f) in Figure 4.4 show the sum SE for 1st and 2nd scenario respectively. With ZF, the median per user SE difference between 1st and 2nd scenario is small since the interference is only caused by the cumulative error part in equation (4.7) where the off-diagonal values of the Gram matrix for 1st scenario is less than the ones from 2nd scenario. Despite the small difference in per user SE, the maximum sum SE in 1st scenario outperform the one from 2nd scenario by 14.89 bits/s/Hz since 22 users are served simultaneously.

With MF, the median per user SE is greatly affected by adding more users as shown in Figure 4.4, sub-plots (c) and (d). The maximum sum SE is achieved when only two users are selected in both scenarios. For 22 users, the sum SE in 1st scenario is greater by 6.98 bits/s/Hz at 50 dB SNR.

Algorithm 1: Sorting users by minimising spatial correlation

set $K = 22$
$min = \boldsymbol{G}_{1,1}$ ▷ Initialise min
for $m = 1 : K$ **do**
    ▷ Searching for the lowest spatial correlation between 2 users
    for $n = l : (m-1)$ **do**
        if $\boldsymbol{G}_{m,n} < min$ **then**
            $min = \boldsymbol{G}_{m,n}$.
            $\mathscr{L}_1 = m$
            $\mathscr{L}_2 = n$ ▷ Updating the first two indexes of $\mathscr{L}$ vector
        end
    end
end
$k = 2$
while k<K **do**
    $\mathscr{D} = \mathscr{L}$ ▷ where$\mathscr{L} \in [1, k]$
    $min = \boldsymbol{G}_{1,1}$
    for $a = l : size(\mathscr{D})$ **do**
        $sum = 0$
        for $b = l : k$ **do**
            ▷ Calculating mean spatial correlation
            $sum = sum + \boldsymbol{G}_{a,b}$
        end
        $meanCOR = sum/k$
        if $meanCOR < min$ **then**
            $elected = \mathscr{D}_a$.
        end
    end
    $k = k + 1$
    $\mathscr{L}_k = elected$ ▷ Add elected user to $\mathscr{L}$ vector
end

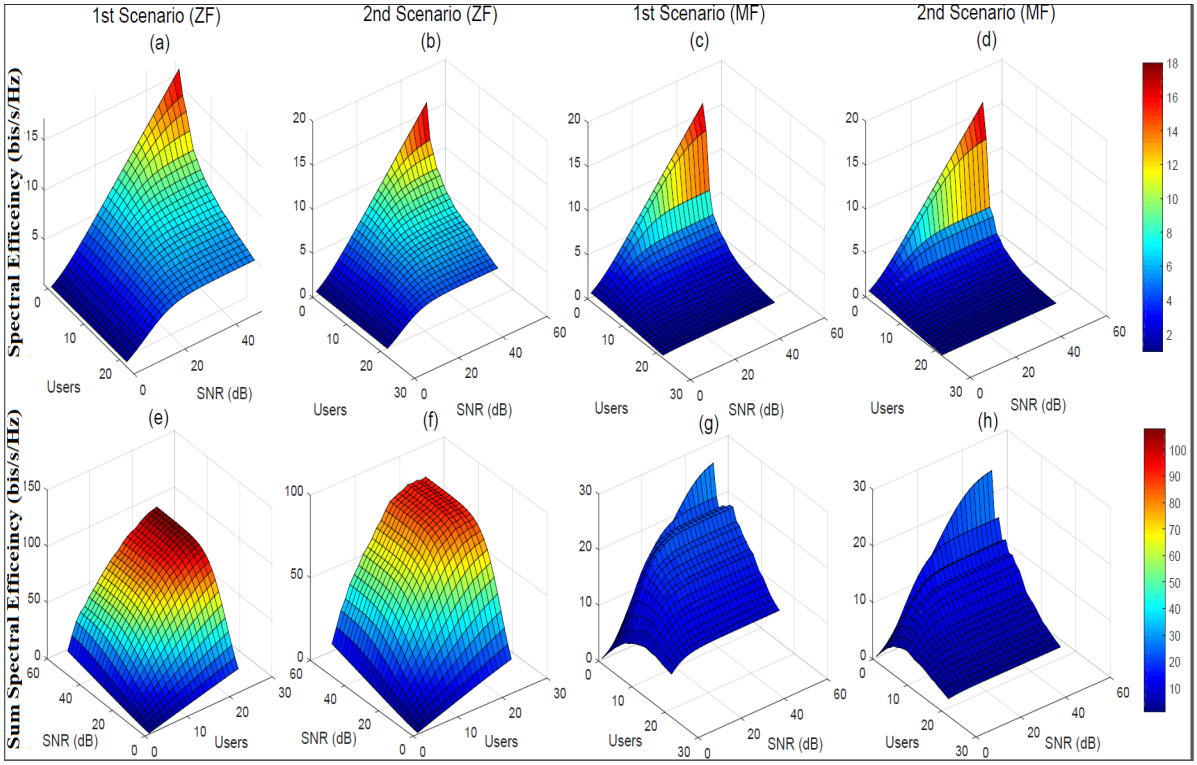

Figure 4.4: SE (1st row) and sum SE (2nd row) comparison between IID Rayleigh channel and measured indoor channel with ZF and MF.

4.5.3 Practical Evaluation

A common measurement of signal quality used in 3GPP LTE standards is the EVM. It is a comprehensive metric which embraces all impairments on the transmitted signal as seen by the receiver. Higher MCS are supported when the EVM is smaller [94]. From [116] and [94], the EVM can be given as

$$\text{EVM}\%_k = \sqrt{\frac{\frac{1}{N}\sum_{n=1}^{N}|S_r(n)-S_t(n)|^2}{\frac{1}{N}\sum_{n=1}^{N}|S_t(n)|^2}} \times 100\% \tag{4.16}$$

where N is the number of symbols the EVM was measured over. $S_r(n)$ is the nth normalized received symbol and $S_t(n)$ is the ideal value of the nth symbol. For comprehensive analysis, the EVM was plotted for the 1st and the 2nd scenarios by using ZF and MF. At the time of conducting the work in this chapter, the required EVM for 64 QAM was 9% based on the 3GPP LTE standards [117]. While the required EVM for 256 QAM was being considered and simulation campaigns shown it might be in the range of 1.5%−4% [118]. Therefore, these EVM requirement[1]

[1]The required EVM for 64 QAM and 256 QAM were later changed in the 3GPP TS 34.104 V12.10.0 to 8% and 3.5% respectively [94] which were used for the work in chapter 5.

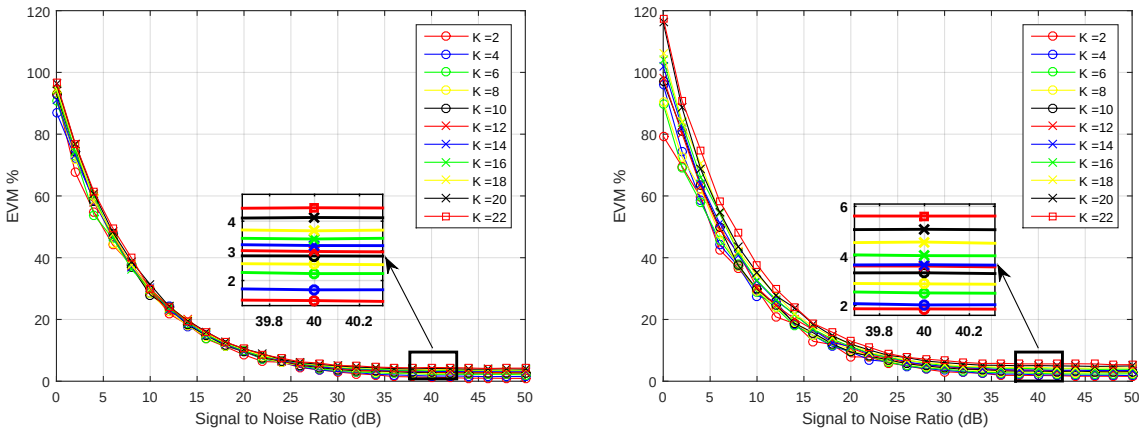

(a) IID Rayleigh channel

(b) Measured indoor channel

Figure 4.5: EVM performance range with inaccurate CSI by using ZF. Total number of users is gradually increased from 2 into 22 by two users.

Table 4.1: Realistic Performance (IID Rayleigh Scenario with ZF).

	Serving all Users		Maximizing Sum SE
K	22	25	19
MS	64-QAM	64-QAM	256-QAM
Sum SE	72.864 b/s/Hz	82.8 b/s/Hz	83.9 b/s/Hz

Table 4.2: Realistic Performance (Measured indoor scenario with ZF).

	Serving all Users		Maximizing Sum SE
K	17	21	16
MS	64-QAM	64-QAM	256-QAM
Sum SE	56.3 b/s/Hz	69.55 b/s/Hz	70.656 b/s/Hz

were chosen for the work in this chapter. (a) and (b) in Figure 4.5 show the EVM results with ZF for the 1st and the 2nd scenarios respectively. For the 1st scenario, the EVM range was between 1.5% and 4.5% which corresponds to K from 2 till 22 with 40 dB SNR. In the 2nd scenario, the EVM performance was slightly degraded and its range becomes between 1.9% and 5.8%. The increment in the EVM range is caused by the high spatial correlation in the 2nd scenario which amplifies the impact of inaccurate CSI. Table 4.1 and Table 4.2 show the sum SE results at 40 dB SNR for the 1st and 2nd scenarios respectively. In the 1st scenario, the maximum sum SE is achieved by serving 19 users simultaneously with 256-QAM. When adding more users, 64-QAM is used in order to provide reliable communications. Here the SE will only be increased when 26 or more users are served. In the 2nd scenario, the maximum sum SE is achieved by serving 16 users simultaneously with 256-QAM. This value can only be increased by adding more than five users if 64-QAM is applied. As it is shown in both scenarios, by adding more users the EVM performance becomes worse and the sum SE could be decreased. The degradation in the EVM

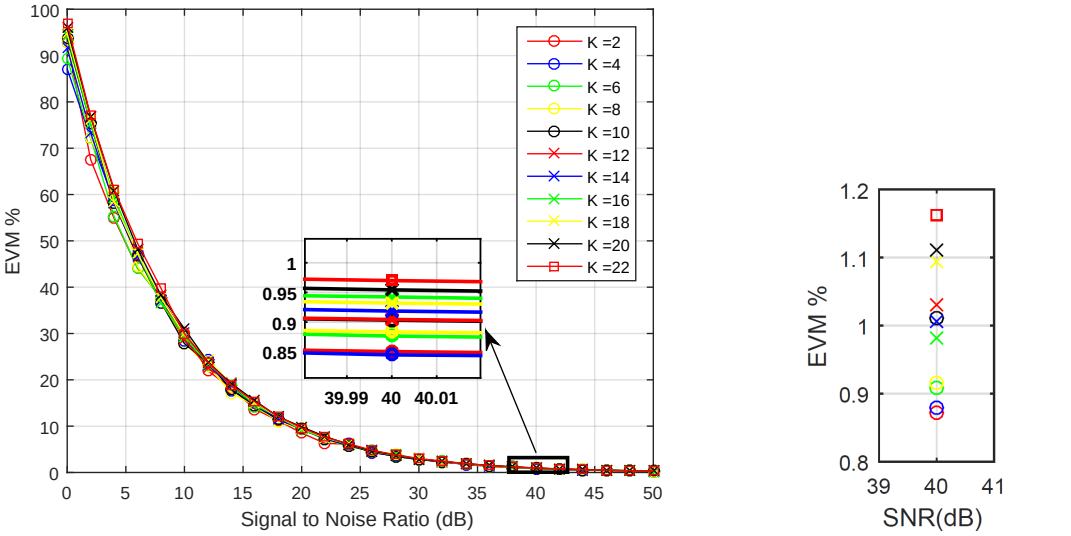

(a) IID Rayleigh channel

(b) Measured indoor channel

Figure 4.6: EVM performance range with perfect CSI by using ZF. Total number of users is gradually increased from 2 into 22 by adding two users.

Figure 4.7: Impact of user number on the observed EVM. 64-QAM with ZF for 24 users on the left and 22 users on the right.

performance can be seen in Figure 4.7, which shows a a realistic 64-QAM constellations captured from the trial in [119]. Details about this trial can be found in Appendix C. The constellations on the left were captured with 24 active users. The constellations on the right were captured after removing two users randomly. The observed EVM was enhanced just by removing two users since the "Cumulative Error" part in (4.7) was reduced by two users. The EVM performance with perfect CSI is shown in Figure 4.6 where (a) is for the 1st scenario and (b) is for the 2nd scenario. The EVM performance was enhanced and its range found to lie between 0.85% and 0.97% in 1st scenario and between 0.89% and 1.18% in 2nd scenario which corresponds to K from 2 up to 22 with 40 dB SNR. With perfect CSI, the EVM performance is slightly affected by the number of users since it only amplifies the noise. Figure 4.8 shows the EVM results with MF for 1st and 2nd scenarios with 40 dB SNR. The sub-plot (a) and (b) are for the 1st scenario with perfect and inaccurate CSI respectively. The sub-plot (c) and (d) are for the 2nd scenario with perfect and inaccurate CSI respectively. The impact of inaccurate CSI can be ignored in both scenarios. The

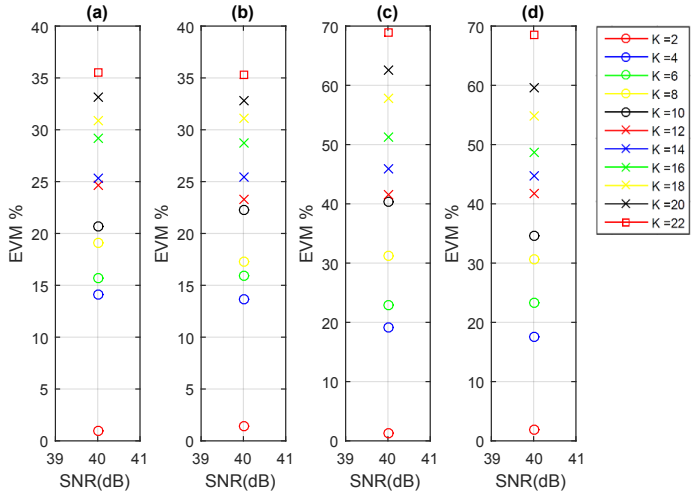

Figure 4.8: EVM performance comparison with MF between 1st (a&b) and 2nd (c&d) scenario.

EVM performance is highly affected by the number of users. Compared to ZF, the EVM value corresponds to 22 users is increased by 30.5% in the 1st scenario and 64% in the 2nd scenario. In the 1st scenario, the maximum number of users that can be served is 8 using QPSK. In the second scenario, the maximum number of users is reduced by two using the same MS. Maximum sum SE of 8.832 bits/s/Hz is achieved by serving two users with 256-QAM in both scenarios.

4.6 Number of Antennas at BS Compared to Hardware Quality

By further inspecting the results obtained in section 4.1 and applying the practical evaluation method in section 4.5.3, some insight can be gained on the trend of maximizing the sum SE with the relation to the number of BS antennas, spatial correlation between users and CSI accuracy. Figure 4.10 shows the intensity plot results for the user-side Gramian matrix for 32 and 128 elements of the 32×4 patch array. For the 32 antenna case, the results were obtained using the second 8×4 panel in from the left when facing the array. In order to obtain accurate results that solely represent the achievable spatial separation, it is important to remove path-loss differences among UEs by applying a form of normalisation to the raw captured channel matrix, denoted as $\boldsymbol{H}_b^{\text{raw}}$. To achieve this, the first normalisation described in [120] was applied. This normalisation ensures that the average energy across all B frequency resource blocks (12 subcarriers per RB) and M antennas for a given user vector in $\boldsymbol{H}_b^{\text{raw}}$, denoted as $\boldsymbol{h}_{i,b}^{\text{raw}}$ for user i, is equal to one. In this sense, the variations across frequency are retained to provide better statistics. This is calculated as

$$\boldsymbol{h}_{i,b}^{\text{norm}} = \sqrt{\frac{MB}{\sum_{b=1}^{B} \|\boldsymbol{h}_{i,b}^{\text{raw}}\|^2}}\, \boldsymbol{h}_{i,b}^{\text{raw}} \tag{4.17}$$

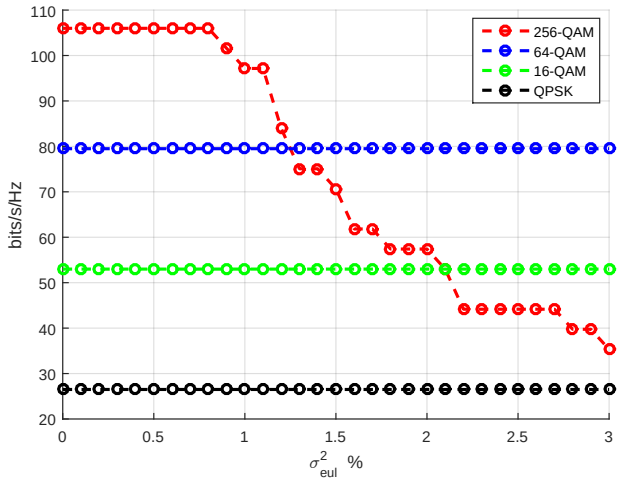

Figure 4.9: Maximum sum SE with ZF and MMSE in UL by different MS.

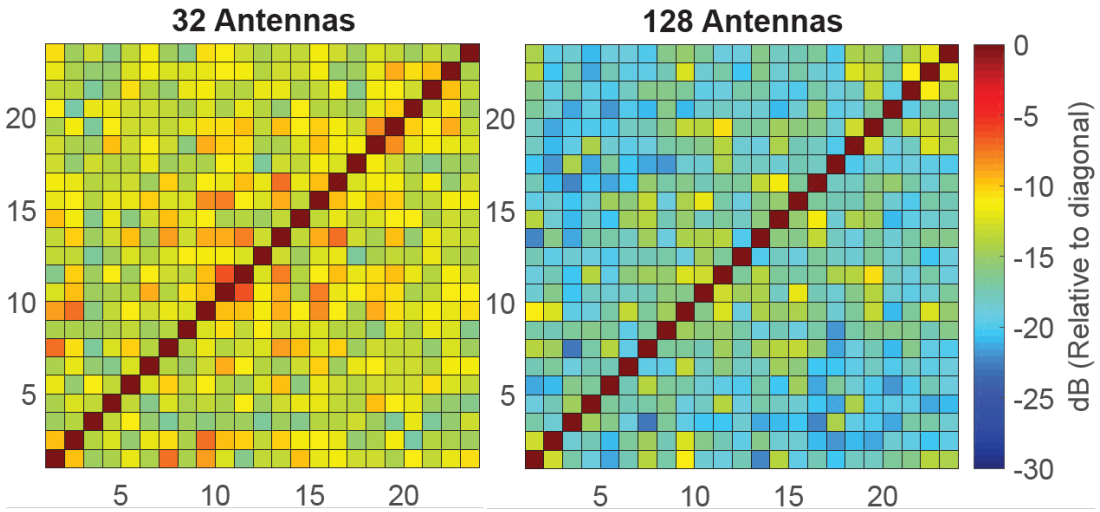

Figure 4.10: User-side Gramian intensity plots for 24 UEs for the measured indoor scenario.

where $\boldsymbol{h}_{i,b}^{\text{norm}}$ is the ith row of the normalised channel matrix $\boldsymbol{H}_{b}^{\text{norm}}$. The first thing that can be seen is that the correlation level between UEs with 128 BS antennas is lower than the one with only 32 BS antennas due to the channel hardening effect. By using ZF and MMSE decoders in the UL Ma-MIMO simulator mentioned earlier with rate 3/4 low-density parity-check (LDPC) code as described in [121] , the sum SE that can be achieved with each MS and $\sigma^2_{e_{ul}} \in [0,3\%]$ can be seen in Figure 4.9. An IID Rayleigh channel is used, where M=128 and K=24. The maximum sum SE is achieved by serving all the 24 UEs with 256-QAM when $\sigma^2_{e_{ul}} \in [0,0.8\%]$. When the UL error variance value is greater than 0.8%, the sum SE starts decreasing due to the lower number of UEs that can be served simultaneously in order to fulfil the EVM requirements for the 256-QAM. When $\sigma^2_{e_{ul}} \in [1.3\%,3\%]$, the maximum sum SE is achieved by serving all the 24 UEs

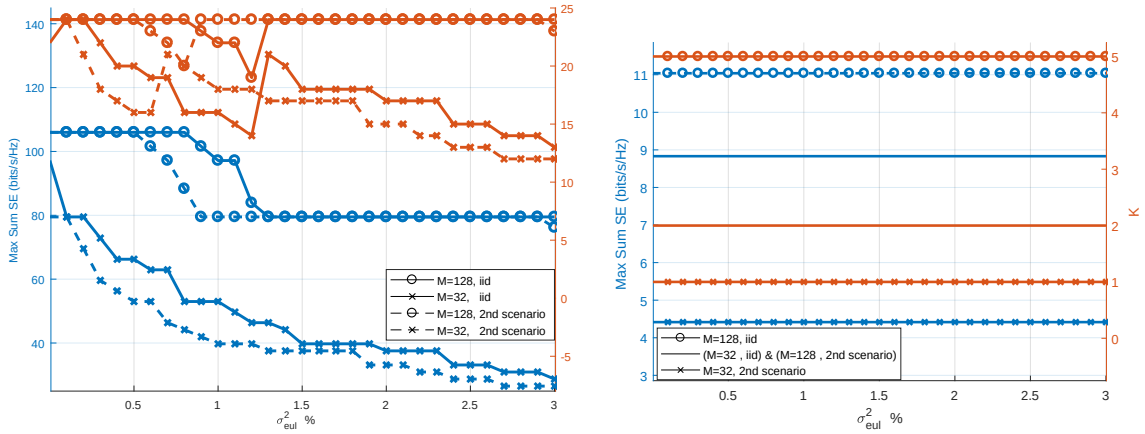

(a) With ZF and MMSE decoders

(b) With MF decoder

Figure 4.11: Maximizing sum SE in the UL data transmission. Blue: maximum sum SE. Red: number of simultaneous users.

with 64-QAM. The blue colour in Figure 4.11 shows the maximum sum SE that can be achieved by using ZF or MMSE in (a) and MF in (b) . For comparison purposes, the correspondent number of UEs have been plotted in red colour on a second axis. Lower MS order is being used each time the number of UEs is increased by increasing the value of $\sigma^2_{e_{ul}}$. An IID Rayleigh channel is used for the 1^{st} scenario, where K=24 and M=128. Then number of antennas at the BS was decreased to 32 to increase the spatial correlation value between users. Both real-channels used to produce the results in Figure 4.10 were used in the 2^{nd} scenario. With perfect CSI and ZF, 256-QAM is used in both scenarios with M=128 and M=32 in Figure 4.11 sub-plot (a). When M=128 and $\sigma^2_{e_{ul}} \in [0, 0.5\%]$, the maximum sum SE with the real-channel in the 2^{nd} scenario was similar to the one achieved by the IID channel where 24 UEs are served simultaneously. When $\sigma^2_{e_{ul}} \in [0.6\%, 0.8\%]$ and $\sigma^2_{e_{ul}} \in [0.9\%, 1.2\%]$, number of UEs is decreased for the real-channel and IID channel respectively in order to fulfil the 256-QAM requirements. But when $\sigma^2_{e_{ul}} \geq 0.9\%$ and $\sigma^2_{e_{ul}} \geq 1.3\%$, the maximum sum SE is achieved by serving all the 24 UEs with 64QAM except when $\sigma^2_{e_{ul}} = 3$ with the real-channel scenario. By decreasing number of antennas at the BS to 32, the maximum sum SE become more sensitive to the accuracy of CSI. The maximum sum SE dropped by 58 bits/s/Hz when $\sigma^2_{e_{ul}}$ is increased from 0 to 3% with real-channel in 2^{nd} scenario. While it was only decreased by 34 bits/s/Hz with 128 antennas at the BS. Besides, the same maximum sum SE is achieved by using real-channel or IID channel with most of the CSI accuracy when M=128. While the maximum sum SE is always achieved by using IID channel when M=32.

These results can be explained from the "Cumulative Error" part in (4.7) and (4.8). When M=128, the matrix elements resulting from inverting the Gram matrix $\left(\hat{\boldsymbol{H}}^H_{ul}\hat{\boldsymbol{H}}_{ul}\right)^{-1}$ are small because of the channel hardening effect. Therefore, the interference resulting in this part will be small as well and more UEs can be served simultaneously with higher MS. While when M=32,

the matrix elements resulting from inverting the Gram matrix $\left(\hat{\boldsymbol{H}}_{ul}^{H}\hat{\boldsymbol{H}}_{ul}\right)^{-1}$ are high. Therefore lower MS with less number of UEs are used.

When MF decoder is used, the maximum sum SE is not affected by the CSI accuracy when $\sigma_{e_{ul}}^2 \in [0,3\%]$ as shown in Figure 4.11 sub-plot (b). The maximum sum SE is achieved by serving five UEs with 16-QAM using an IID channel with M=128. While by using the same number of antennas with real-channel, the maximum sum SE is decreased by 2.1 bits/s/Hz which is the same results obtained from 32 antennas with an IID channel. This is achieved by serving two UEs with 256-QAM. The lowest maximum sum SE is achieved by serving only one user with 256-QAM using real-channel with M=32. Although MF decoder has very low sensitivity to CSI accuracy, it is highly sensitive to number of antennas and spatial correlation values between UEs.

Increasing number of antennas at the BS could be expensive because of the additional hardware requirements. Ma-MIMO with high CSI accuracy and low number of antennas could be a better investment if it costs less and has similar performance. This can be achieved by using hardware with high quality, such as better ADCs and LNAs, to reduce the hardware impairment error and the noise floor value. Sub-plot (a) in Figure 4.11 shows that with 32 antennas at the BS and $\sigma_{e_{ul}}^2 = 0.1\%$, the same maximum sum SE can be achieved when the number of antennas is increased to 128 with $\sigma_{e_{ul}}^2 \geq 0.9\%$. This was experimentally validated in the next section. Further results with different channel conditions can be found in Appendix B including DL data transmission.

4.7 Real-Time Evaluation Using Massive MIMO Test-bed

In this section, real-time results are presented using the Ma-MIMO testbed in section 3.1. These results demonstrate the impact of inaccurate CSI on the SE and show that increasing number of antennas at the BS can decrease this impact. It also validates the following:

- The maximum sum SE with practical number of antennas could be achieved by decreasing the number of users.
- Inaccurate UL CSI has greater impact on the DL data transmission than it has on the UL data transmission due to the error amplification caused by the reciprocity calibration matrix.
- By using ZF or MMSE, a lower number of antennas at the BS with high hardware quality could be better than increasing number of antennas and reducing the hardware quality.

MF, ZF and MMSE were used for UL and DL data transmission by using the exact same static environment but with two different UL CSI accuracy values.

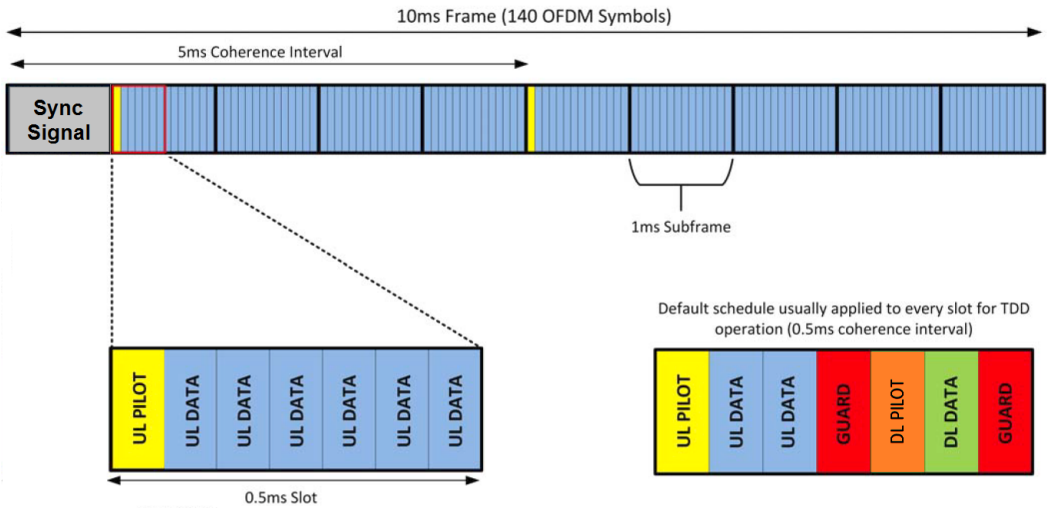

Figure 4.12: The frame schedule used in the Ma-MIMO test-bed for real-time evaluation.

4.7.1 Frame Schedule

For the SE results shown in this real-time evaluation, two different frame schedules were configured for two different scenarios. For the UL scenario, the PHY frame schedule used in section 3.1.3 was modified so that only UL data with two UL pilots per radio frame were used which can be seen in Figure 4.12. While in the DL scenario, only DL data with two UL pilots and two DL pilots per radio frame were used. The first OFDM subframe is for synchronization in both scenarios to achieve sample alignment.

4.7.2 Low CSI Accuracy

For low CSI accuracy, OTA synchronisation was used based on Zadoff-Chu sequence. The phase of the sync signal was generated randomly from each antenna at the BS which created nulls in different locations. This caused sync losses for the users based on their locations and the sync signal phases from the antennas at the BS. The synchronization error causes inter-carrier interference (ICI), inter-symbol interference (ISI) and interference between data streams due to the inaccurate CSI. The BS and the users save the sequence number of each transmitted radio frame. When the user doesn't detect the sync signal, it saves the radio frame number. The sum SE calculation doesn't consider the data transmission between the user who lost the sync signal and the BS. This can be done by removing the data transmitted during saved radio frame number in both UL and DL for that user. By doing that, the impact of ICI and ISI was removed before calculating the sum SE while the interference caused by the inaccurate CSI is only considered in this scenario.

Figure 4.13: Measurement Environment (CSN Research Laboratory).

4.7.3 High CSI Accuracy

To increase the CSI accuracy, cabled synchronisation was used with an Octoclock module [96]. To achieve sample alignment, a start trigger that signals the start of the first radio frame is fanned out to all radios by equal length cables. The user clients were connected to the Octoclock by extended cable and the timing offsets were corrected for. For fair comparison, when the data transmitted between the UE and the BS was removed from the sum SE calculation in the low CSI accuracy scenario, it was also removed from the high CSI accuracy scenario.

4.7.4 Measurement Environment

The CSN lab was used for LOS measurements between the BS and 12 UEs from 6 USRPs. Measurements were performed outside of university hours and the Ma-MIMO test-bed was controlled remotely to ensure the same static environment was applied in all scenarios. An overview of the setup can be seen in Figure 4.13. At the BS side, 64 element array was used providing half-wavelength spacing at 3.5 GHz. A floor plan of the experiment is shown in Figure 4.14 with the UE locations.

4.7.5 Validation Results

Table 4.3 and Table 4.4 show the maximum uncoded sum SE results for the UL scenario with high and low CSI accuracy respectively. Maximum sum SE of 56.59 bits/s/Hz is achieved by using ZF or MMSE with M=64 and high CSI accuracy serving all the 12 UEs with 64-QAM.

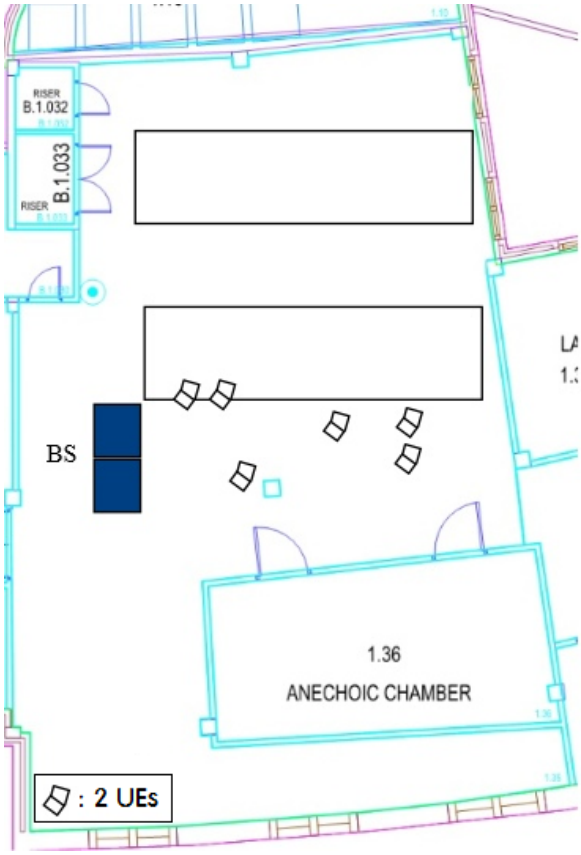

Figure 4.14: CSN Lab floor plan showing the BS and UEs locations.

Although no error correction was used, this value is equal to the error free version using the same frame schedule, number of UEs and MS. By reducing the number of antennas to 32, the maximum sum SE is decreased by 6.39 bits/s/Hz due to the higher interference level although the same number of UEs and MS are used. The interference caused by "Cumulative Error" part in (4.7) and (4.8) when M=64 is less than the one when M=32 due to the channel hardening effect. With low CSI accuracy, the maximum sum SE with ZF or MMSE is decreased by 7.49 bits/s/Hz and 13.2 bits/s/Hz for M=64 and M=32 respectively. Decreasing the CSI accuracy has greater impact when M=32 with ZF and MMSE. These results validate the theoretical work on massive MIMO showing that by increasing number of antennas at the BS, the interference caused by inaccurate CSI with ZF and MMSE will decrease. With MF, the CSI accuracy has no impact on the maximum sum SE. Only the number of antennas affect the maximum sum SE achieved by MF in the UL scenario. This can be explained from (4.6) where the interference caused by the "Desired Signal + Interference" part, that is sensitive upon the number of antennas, is very large compared to the one caused by the "Cumulative Error" part which is affected by the CSI accuracy.

Table 4.5 and Table 4.6 show the maximum uncoded sum SE results for the DL scenario with high and low CSI accuracy respectively. The maximum sum SE results are decreased in the DL

scenario due to the difference between the estimated calibrated channel and the actual channel during DL transmission. With high CSI accuracy and ZF or MMSE precoders, the maximum sum SE is decreased by 22.19 bits/s/Hz and 19.2 bits/s/Hz with M=64 and M=32 respectively compared to the UL scenario with high CSI accuracy. While by applying the same comparison for the low CSI accuracy, the maximum sum SE is decreased by 34.1 bits/s/Hz and 29 bits/s/Hz with M=64 and M=32 respectively. By comparing the SE degradation between UL and DL scenarios with high and low CSI accuracy, the maximum sum SE with low CSI accuracy was shown to be affected more. The additional maximum sum SE degradation due to low CSI accuracy was 11.91 bits/s/Hz and 9.81 bits/s/Hz with M=64 and M=32 respectively, despite using the same reciprocity calibration algorithm. This can be explained in (4.12) where the error introduced by inaccurate UL CSI ($\boldsymbol{e}_{ul}$) is multiplied by the calibration matrix ($\boldsymbol{D}_b$). These results validate that UL CSI accuracy has greater impact on the DL data transmission than it has on the UL data transmission. By comparing the results between high CSI accuracy and low CSI accuracy in UL and DL scenarios, it can be seen that the maximum sum SE with 32 antennas and high CSI accuracy always outperforms the one from 64 antennas with low CSI accuracy when ZF or MMSE is used. This validates the simulation results in section 4.6 and concludes that increasing number of antennas at the BS might not be efficient as much as increasing the hardware quality to acquire more accurate CSI. By serving all the 12 UEs, the maximum sum SE was only achieved in the UL scenario with ZF and MMSE using high CSI accuracy. While to achieve the maximum sum SE for the remaining scenarios, the number of UEs was decreased. These results validate that the maximum sum SE with practical number of antennas could be achieved by decreasing number of users. From the results obtained in this section and section 4.6 using ZF and MMSE, the maximum sum SE and number of UEs keep changing. That should emphasise the need for a user grouping algorithm not only at the cell edges, but also within the cell itself in order to maximize the sum SE.

Table 4.3: Real-time Results for UL Scenario (High CSI Accuracy).

	K / MS		Sum SE (b/s/Hz)	
	M=32	M=64	M=32	M=64
MF	K=3, b=2	K=2, b=4	4.4	6.2
ZF& MMSE	K=12, b=6	K=12, b=6	50.2	56.59

Table 4.4: Real-time Results for UL Scenario (Low CSI Accuracy).

	K / MS		Sum SE (b/s/Hz)	
	M=32	M=64	M=32	M=64
MF	K=3, b=2	K=2, b=4	4.4	6.2
ZF& MMSE	K=9, b=6	K=11, b=6	37	49.1

Table 4.5: Real-time Results for DL Scenario (High CSI Accuracy).

	K / MS		Sum SE (b/s/Hz)	
	M=32	M=64	M=32	M=64
MF	K=3, b=2	K=3, b=2	3.8	4.5
ZF& MMSE	K=10, b=4	K=11, b=4	31	34.4

Table 4.6: Real-time Results for DL Scenario (Low CSI Accuracy).

	MS / K		Sum SE (b/s/Hz)	
	M=32	M=64	M=32	M=64
MF	K=3, b=2	K=2, b=4	3.2	4.2
ZF& MMSE	K=6, b=2	K=10, b=2	8	15

4.8 Summary

In this chapter, the highest SE of 145.6 bits/s/Hz achieved for any wireless system to date and its limiting factors were presented. The impact of the number of users upon maximizing sum SE in a TDD single-cell Ma-MIMO system was illustrated and experimentally validated. Common linear decoders/precoders, MF, ZF and MMSE, were used in UL and DL data transmission cases. A practical method based on EVM performance for realistic SE calculation was compared with the theoretical method based on Shannon capacity. By using both IID Rayleigh and measured Ma-MIMO channels with 1% CSI estimation error, it was shown that the maximum theoretical sum SE is achieved by increasing the number of users. Unlike the conventional method for theoretical SE calculation or assuming perfect CSI, it was shown and experimentally validated that the maximum sum SE could be achieved by decreasing the number of users with practical number of antennas at the BS.

Furthermore, it was shown and experimentally validated that the inaccurate UL CSI has greater impact on the DL data transmission than it was on the UL data transmission due to the reciprocity calibration error amplification. Besides, by using ZF or MMSE, a lower number of antennas at the BS with high hardware quality could be better than increasing the number of antennas and reducing the hardware quality.

The work in this chapter was based on the EVM performance with static users environment. Some interesting points were not covered, such as the EVM performance with mobility environment and how the EVM corresponds to the bit error rate (BER) in different scenarios. Although the BER metric requires additional overheads, it is still more accurate metric than the EVM. The Ma-MIMO mobility evaluation in [34] could be extended for future work to cover the impact of inaccurate CSI, where both the EVM and the BER metrics are used.

CHAPTER 5

ADAPTIVE USER GROUPING BASED ON EVM PREDICTION FOR EFFICIENT AND ROBUST MASSIVE MIMO IN TDD

This chapter proposes novel user grouping algorithms to further enhance the Ma-MIMO advantages for different wireless applications. The results and conclusions of this chapter have been published in [36] and submitted to [35]. The following summarize the main contributions in this chapter:

- Introduce an estimation method with high accuracy associating EVM to SINR values for massive MIMO with ZF and MMSE.
- Introducing an EVM prediction method for a subset of user spatial bearers taken from the original set of simultaneous users in a single cell Ma-MIMO.
- Illustrating the need for a user grouping algorithm for single cell Ma-MIMO.
- Presenting an adaptive user grouping algorithm for maximizing the SE, which is more desirable for cellular networks.
- Presenting an adaptive user grouping algorithm for maximizing the number of simultaneous users for low data rate bearers which is suitable for the IoT.
- Presenting an adaptive user grouping algorithm for a specific quality per user for applications such as wireless cameras at major cultural or sporting events.
- For the first time, a methodology which addresses the interference caused by the user channel vectors as well as hardware impairments for a single cell Ma-MIMO.
- Validate three adaptive user grouping algorithms proposed by the author experimentally using a real-time trial as part of the world's first urban 5G showcase using a software-defined radio Ma-MIMO testbed [122].

Theoretical Ma-MIMO work indicates that the user channel vectors become pairwise orthogonal as the number of BS antennas is increased, facilitating the effective use of MF [22]. However, the level of spatial orthogonality achieved when using a practical number of antennas in real channels may not be ideal as shown in chapter 3. When the individual user channels become correlated, ZF or MMSE become necessary for reliable data transmission as shown in chapter 4. For real system deployments the BS has a fixed number of antennas, whilst the number of active users can vary with time. Number of users could equal or surpass the number of BS antennas, particularly during rush hour or at major cultural or sporting event. User grouping is an essential solution for this problem, where each group is served by different radio resources [123]. This could be the only need for user grouping algorithms in an ideal scenario. However, there are some challenges that need to be addressed in Ma-MIMO system architectures.

Linear techniques, such as ZF and MMSE can suppress the interference between users, but this requires perfect CSI. Errors in CSI can occur for many reasons such as local oscillator (LO) phase noise, errors in reciprocity calibration and quantization errors [110]. Although ZF and MMSE algorithms can suppress interference caused by the channel between users and the BS, they are unable to suppress interference caused by inaccuracy in CSI. In addition, high spatial correlation between users will amplify the interference caused by inaccurate CSI. Several studies have addressed multi-grouping for Ma-MIMO. In [124] users are grouped according to the severity of inter-beam interference: users which won't cause serious inter-beam interference are allocated into an identical group, whilst users that cause serious inter-beam interference are distributed into different groups. In [125] the separation of users with high spatial correlation into different groups is addressed. The grouping process relies on finding the correlation coefficients greater than a certain threshold and isolating the corresponding users in separate groups. These are then served at different scheduled times. The works in [124] and [125] all assume perfect CSI, whilst in [126], inaccurate CSI is considered for DL due to reciprocity calibration errors of a TDD architecture. This work was extended in [127] and focused on noncooperative transmission for multicell multicast networks using Ma-MIMO. In both of these studies, the focus is primarily on multi-cell and considers the impact of large-scale channel attenuation between the various users and the BS. Most previous research has focused on the DL scenario by separating the users with high spatial correlation based only on the channel between the BS and the users. Importantly, these approaches do not consider the interference caused by inaccurate CSI which limits the application of these results in real-world deployments. This chapter proposes novel adaptive user grouping algorithms for single cell Ma-MIMO for both UL and DL scenarios. The proposed algorithms decrease the interference level between users and mitigates the impact of inaccurate channel estimation. This is achieved by exploiting the novel EVM prediction method introduced in this chapter.

The chapter is structured as follows. In section 5.1, an estimation method between the EVM and the SINR values is presented using ZF and MMSE decoders. An EVM prediction method

for a subset of users taken from the original set of simultaneous users is also introduced for a single cell Ma-MIMO. Section 5.2 illustrates the need for a user grouping algorithm in a single cell Ma-MIMO. Section 5.3 introduces three adaptive user grouping algorithms for a single cell Ma-MIMO covering several performance objectives. Section 5.4 provides results for the proposed adaptive user grouping algorithms from a Ma-MIMO simulator. Section 5.5 validates the proposed adaptive user grouping algorithms experimentally with real-time results in the world's first urban 5G showcase using a software-defined radio Ma-MIMO testbed. Lastly, Section 5.6 summarizes the key results from this chapter.

5.1 EVM Prediction & SINR Estimation for Massive MIMO

In this section, two different scenarios were considered to evaluate the accuracy of the SINR estimation and the EVM prediction. An IID Rayleigh channel was used in the first scenario with perfect and imperfect CSI, where M=128 and $K \in \{2, 12, 22\}$. In the second scenario, the real channels captured from the trial described in section 4.1 were used. These scenarios were run through an uplink Ma-MIMO simulator described in section 4.5. For imperfect CSI in both scenarios, the error in the channel estimation between the UEs and the BS is modeled as a complex Gaussian distribution $\sim \mathscr{CN}\left(\mathbf{0}, \sigma_e^2 \boldsymbol{I}_M\right)$ [114] where an error variance of 0.01 (1%) was used for the simulations shown. Whilst this value may be higher or lower and the model may not be so accurate in reality, it serves to illustrate the potential effects of CSI inaccuracies in Ma-MIMO. Instead of writing the EVM in equation 4.16 in a percentage format , it can be written in an root-mean-squre (RMS) format as follows:

$$\mathrm{EVM}_{RMS} = \sqrt{\frac{\frac{1}{N}\sum_{n=1}^{N} |S_r(n) - S_t(n)|^2}{\frac{1}{N}\sum_{n=1}^{N} |S_t(n)|^2}} \tag{5.1}$$

The relation between the EVM and the SNR in a single cell was addressed in many studies such as [116] and [128] which was estimated as follows:

$$\mathrm{SNR} \approx \frac{1}{\mathrm{EVM}_{RMS}^2} \tag{5.2}$$

The above approximation can be used in SISO and SU-MIMO. While in MU-MIMO and Ma-MIMO, the interference between users highly impacts the accuracy of this approximation. In order to increase the estimation accuracy, the SINR can be used in stead of the SNR as follows:

$$\mathrm{SINR} \approx \frac{1}{\mathrm{EVM}_{RMS}^2} \tag{5.3}$$

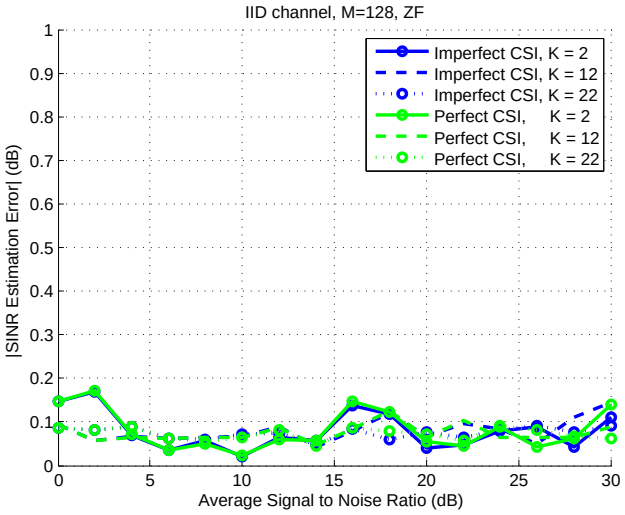

Figure 5.1: SINR estimation error using ZF (IID Rayleigh channels).

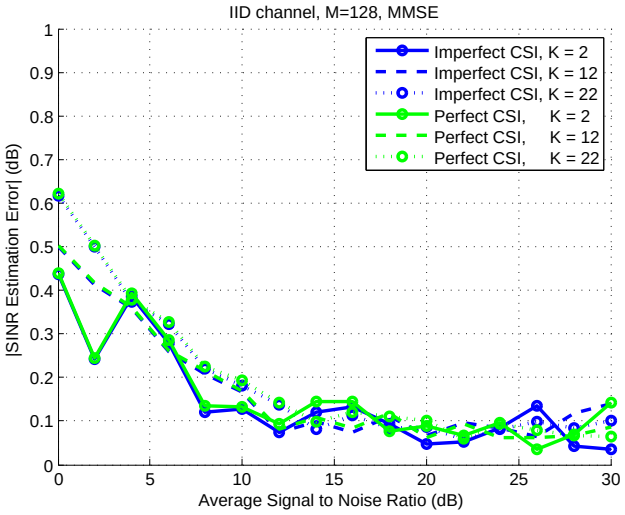

Figure 5.2: SINR estimation error using MMSE (IID Rayleigh channels).

The accuracy of the above equation can be seen in Figure 5.1 and Figure 5.2 for the 1st scenario and Figure 5.3 and Figure 5.4 for the 2nd scenario. The same approximation method was also used in [129]. The UL SINR in (4.4) can be calculated as follows [48]:

$$\mathrm{SINR}_{ul_k} = \frac{\rho_{ul_k} \left| \boldsymbol{w}_k \boldsymbol{h}_{ul_k} \right|^2}{\|\boldsymbol{w}_k\|^2 \sigma_n^2 + \rho_{ul_k} \sum_{i \neq k}^{K} \left| \boldsymbol{w}_k \boldsymbol{h}_{ul_i} \right|^2} \tag{5.4}$$

The errors in the SINR estimation based on the EVM value from (5.3) were plotted in Figure 5.1 and Figure 5.3 using ZF while MMSE was used in Figure 5.2 and Figure 5.4. When MMSE was used, the SINR estimation error is always below 1 dB. By increasing the SNR above 5 dB,

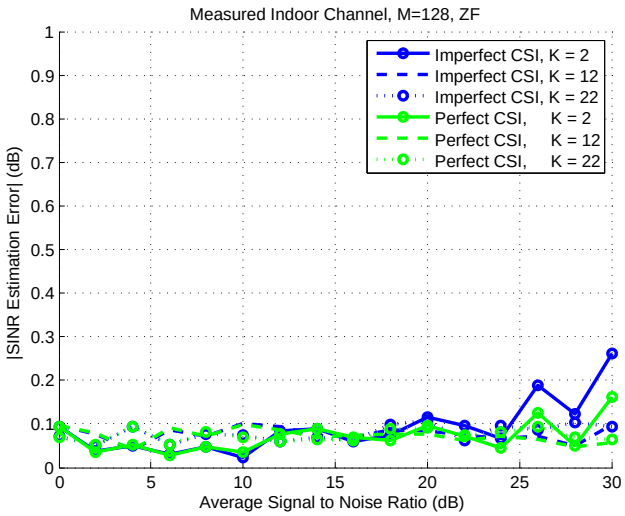

Figure 5.3: SINR estimation error using ZF (Measured indoor channels).

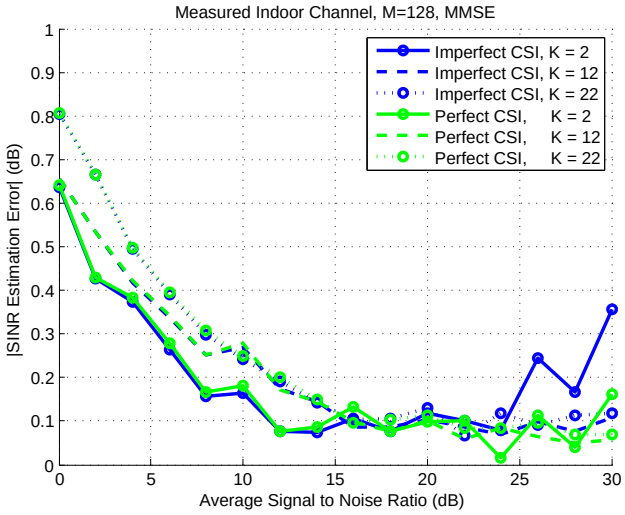

Figure 5.4: SINR estimation error using MMSE (Measured indoor channels).

the error in the SINR estimation falls to below 0.4 dB. When ZF was used in both scenarios, the SINR estimation error is always below 0.3 dB.

By selecting a subset of the available users, the UL SINR can be calculated based on the CSI before the data is transmitted from these users (assuming the channel is coherent across the transmission duration); while the EVM can only be measured after the data is transmitted from these users then received and decoded at the BS side. Hence relying on the measured EVM to predict the MCS order for a subset of users is not applicable. Predicting the highest achievable MCS order for each user is essential for selecting the subset of the available users in order to maximize the SE and provide reliable data transmission. The following two sub-sections 5.1.1 and 5.1.2 show how the EVM value can be predicted.

5.1.1 EVM Prediction Based on SINR Calculation

The UL SINR in (5.4) is calculated based on perfect CSI. Whilst with imperfect CSI, the equation can be modified as follows:

$$\text{SINR}_{ul_k} = \frac{\rho_{ul_k} \left| \boldsymbol{w}_k \hat{\boldsymbol{h}}_{ul_k} \right|^2}{\|\boldsymbol{w}_k\|^2 \sigma_n^2 + \rho_{ul_k} \sum_{i=1}^{K} \left| \boldsymbol{w}_k \boldsymbol{e}_{ul_i} \right|^2 + \rho_{ul_k} \sum_{i \neq k}^{K} \left| \boldsymbol{w}_k \hat{\boldsymbol{h}}_{ul_i} \right|^2} \tag{5.5}$$

Since $\boldsymbol{e}_{ul}$ can't be obtained in real-system, the UL SINR can be estimated by ignoring the error in CSI as follows:

$$\widehat{\text{SINR}}_{ul_{\tilde{k}}} = \frac{\rho_{ul_{\tilde{k}}} \left| \boldsymbol{w}_{\tilde{k}} \hat{\boldsymbol{h}}_{ul_{\tilde{k}}} \right|^2}{\left\| \boldsymbol{w}_{\tilde{k}} \right\|^2 \sigma_n^2 + \rho_{ul_{\tilde{k}}} \sum_{i \neq \tilde{k}}^{\tilde{K}} \left| \boldsymbol{w}_{\tilde{k}} \hat{\boldsymbol{h}}_{ul_i} \right|^2} \tag{5.6}$$

where $\tilde{K}$ is the total number of users in the set that the SINR_{ul_k} is being predicted for $\left(\tilde{K} \leq K\right)$. From (5.3), the EVM value for user k can be predicted as follows:

$$\widetilde{\widetilde{\text{EVM}}}^2_{RMS_{\tilde{k}}} = \frac{1}{\widehat{\text{SINR}}_{ul_{\tilde{k}}}} \tag{5.7}$$

The accuracy of the predicted EVM ($\widetilde{\widetilde{\text{EVM}}}$) square from the above equation is high with perfect CSI. This can be seen in Figure 5.5 and Figure 5.6 for the 1st scenario and Figure 5.7 and Figure 5.8 for the 2nd scenario. The green curves show the error between the predicted EVM from (5.7) before data is transmitted and the actual EVM from (5.1) after the data is received and decoded. When ZF or MMSE is used, the EVM% prediction error is below 1% at 12 dB SNR ($\text{EVM\%} = \text{EVM}_{RMS} \times 100$). By increasing the SNR, the EVM% prediction error is reduced until $\widetilde{\widetilde{\text{EVM}}}_{\tilde{k}} = \text{EVM}_k$ at 20 dB SNR.

The accuracy of the CSI in (5.6) and the number of users can be seen to significantly impact the accuracy of the predicted EVM in (5.7). This can be seen in Figure 5.9 and Figure 5.10 for the 1st scenario and Figure 5.11 and Figure 5.12 for the 2nd scenario. When the SNR is increased above 9 dB and $\tilde{K} = 2$, the EVM% prediction error is always below 1% with ZF and MMSE in both scenarios. When increasing $\tilde{K}$ to 11 $\left(\tilde{K} = K/2\right)$, the EVM% prediction error begins to increase at 20 dB SNR in the 1st scenario and 18 dB SNR in the 2nd scenario. When the SNR value is increased further, the EVM% prediction error is seen to increase as well. The reason for the increment in the EVM% prediction error is the CSI accuracy. The estimated SINR in (5.6) doesn't consider the interference caused by inaccurate CSI as the interference term embeds the CSI error. The CSI accuracy has a greater impact on the EVM% prediction error when the number of users is increased. This can be seen when $\tilde{K}$ is increased to 21 $\left(\tilde{K} = K/2\right)$. Thus, the CSI accuracy plays a major role in the EVM prediction based on the SINR calculation method.

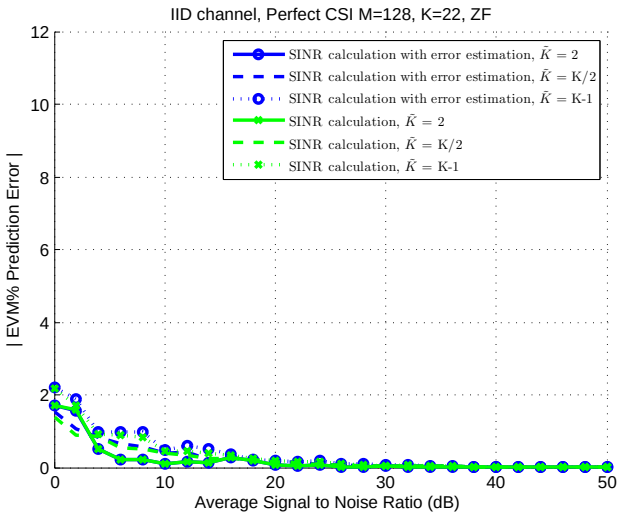

Figure 5.5: EVM prediction error with perfect CSI using ZF (IID Rayleigh channels).

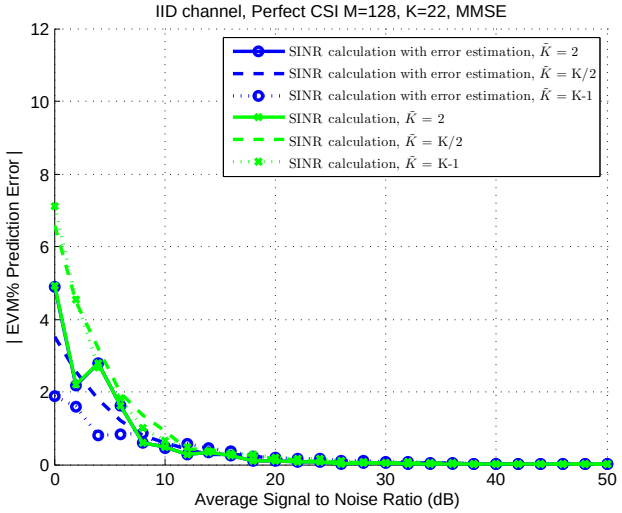

Figure 5.6: EVM prediction error with perfect CSI using MMSE (IID Rayleigh channels).

5.1.2 EVM Prediction Based on SINR Calculation with Error Estimation

The impact of inaccurate CSI is considered in this EVM prediction method. The UL transmit power is adjusted so the received SNR from all users is the same. The EVM value in (5.1) covers the interference caused by inaccurate CSI, whilst the estimated SINR in (5.6) does not. So the error caused by inaccurate CSI can be estimated by calculating the SINR value in (5.6) for user k $\left(\text{when } \tilde{K} = K\right)$ and comparing it with the actual EVM value in (5.1) as follows:

$$\zeta_k = \left| \text{EVM}^2_{RMS_k} - \frac{1}{\widehat{\text{SINR}}_{ul_k}} \right| \tag{5.8}$$

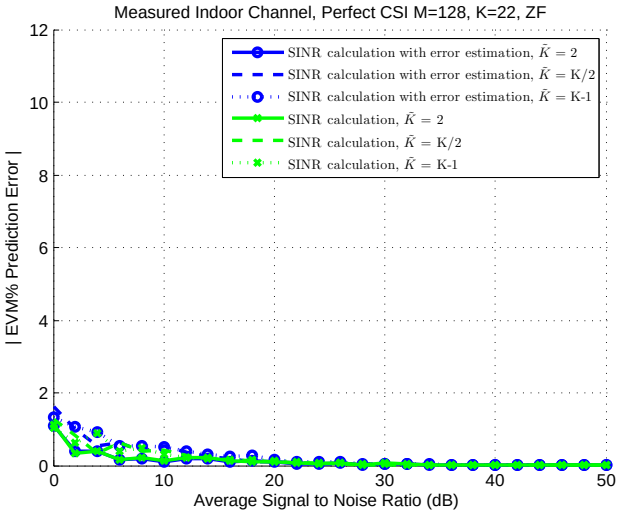

Figure 5.7: EVM prediction error with perfect CSI using ZF (Measured indoor channels).

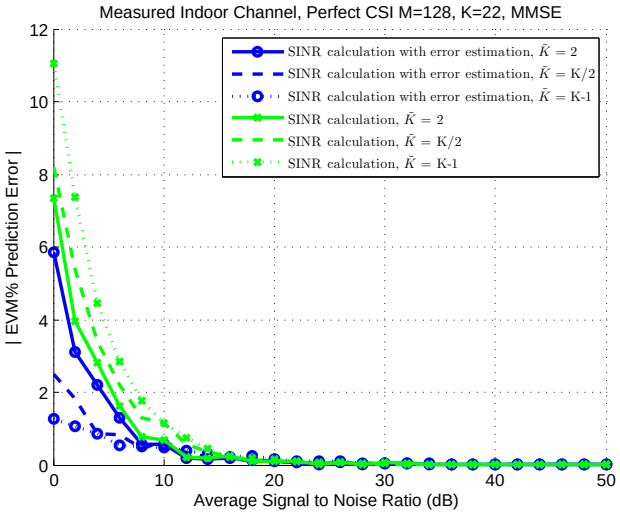

Figure 5.8: EVM prediction error with perfect CSI using MMSE (Measured indoor channels).

The above error is mainly caused by the inaccurate CSI from all the simultaneous users (the error between SINR and EVM estimation is very small as shown earlier in this section). Since the spatial correlation between users has a significant impact on the interference value, the estimated error in the EVM is divided between users based on the spatial correlation ratio in this method. This can be represented in $\boldsymbol{\Upsilon} \in \mathbb{C}^{K \times K}$ where $\Upsilon_{k,l}$ is the partial EVM^2 error estimation value for user k which is caused only by user l.

$$\Upsilon_{k,l} = \begin{cases} \zeta_k \dfrac{\left|\hat{\boldsymbol{h}}_{ul_k}^H \hat{\boldsymbol{h}}_{ul_l}\right|^2}{\sum_{i \neq k}^{K} \left|\hat{\boldsymbol{h}}_{ul_k}^H \hat{\boldsymbol{h}}_{ul_i}\right|^2} & \text{if } k \neq l \\ 0 & otherwise \end{cases} \tag{5.9}$$

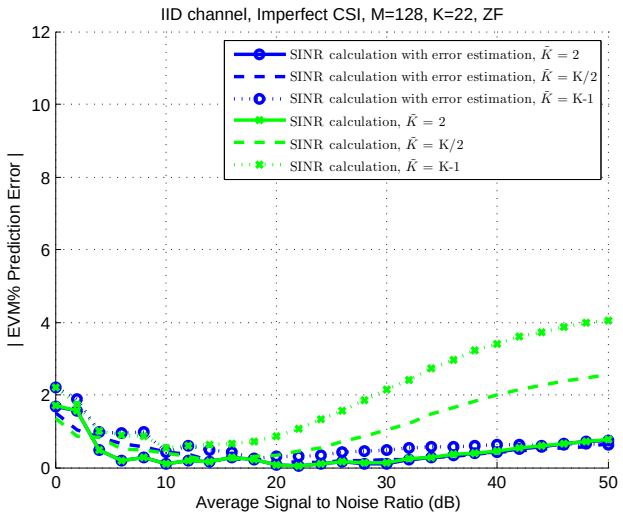

Figure 5.9: EVM prediction error with inaccurate CSI using ZF (IID Rayleigh channels).

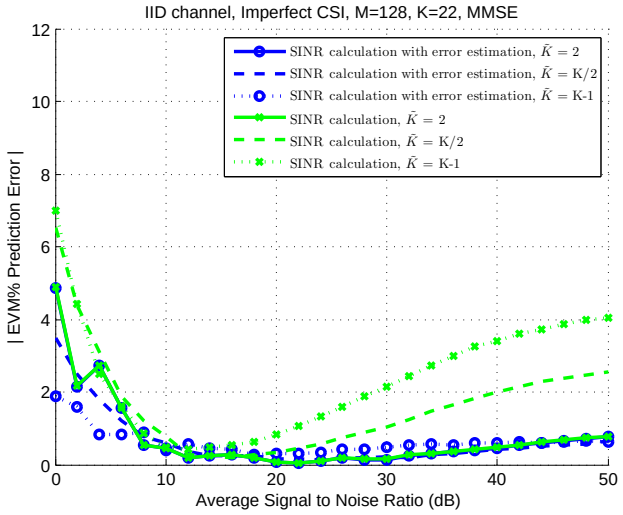

Figure 5.10: EVM prediction error with inaccurate CSI using MMSE (IID Rayleigh channels).

After calculating all the partial EVM^2 error estimation values for all the users, the predicted EVM^2 error value for user $\tilde{k}$ (in the subset of $\tilde{K}$ users) can be written as follows:

$$\widetilde{\widetilde{\zeta k}} = \sum_{i=1}^{\tilde{K}} \Upsilon_{\tilde{k},i} \tag{5.10}$$

By taking into account the above EVM^2 error prediction, equation (5.7) can be modified as follows:

$$\widetilde{\widetilde{\text{EVM}}}^2_{RMS_{\tilde{k}}} = \frac{1}{\widetilde{\text{SINR}}_{ul_{\tilde{k}}}} + \widetilde{\widetilde{\zeta k}} \tag{5.11}$$

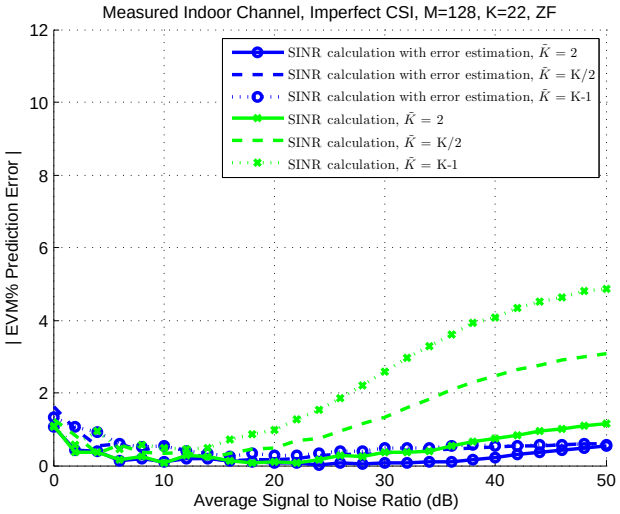

Figure 5.11: EVM prediction error with inaccurate CSI using ZF (Measured indoor channels).

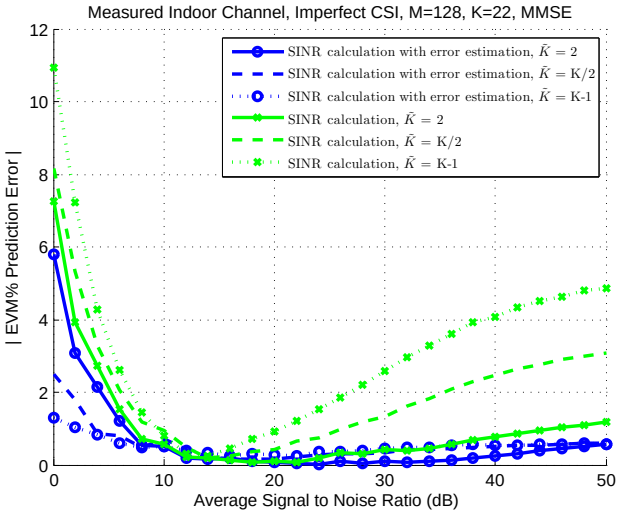

Figure 5.12: EVM prediction error with inaccurate CSI using MMSE (Measured indoor channels).

The accuracy of the $\widetilde{\overline{EVM}}$ from the above equation is evaluated with perfect CSI and inaccurate CSI. With perfect CSI, this method provides the same accuracy as the one in 5.1.1 with ZF as shown in Figure 5.5 and Figure 5.7. When MMSE is used, the proposed method in this section provides higher accuracy compared to the one in 5.1.1. The reason behind this is the low accuracy of the approximation in (5.3) when MMSE is used with low SNR as shown in Figure 5.6 and Figure 5.8. Meanwhile, the proposed method in this section has taken into account the difference between the estimated EVM based on the approximation in (5.3) and the actual EVM from (5.1).

The main advantage of the proposed EVM prediction method in this section is its high accuracy even with inaccurate CSI and large number of users. This can be seen clearly in Figure 5.9 and Figure 5.10 for the 1st scenario and Figure 5.11 and Figure 5.12 for the 2nd

scenario. Unlike the EVM prediction method proposed in 5.1.1, this method maintains the EVM% prediction error below 1% when SNR is greater than 8 dB for both scenarios, with ZF and MMSE, even when $\tilde{K}$ is increased from 2 to $K-1$.

5.2 The Need for User Grouping

5.2.1 Indoor Environment

In this section, three different scenarios were considered to illustrate the need for dividing users into different groups. These scenarios were first run through an UL Ma-MIMO simulator described in section 4.5 using the indoor channel in section 4.1. The EVM is used to evaluate the Ma-MIMO performance for differing numbers of users when CSI errors are present. This metric was used for the three different scenarios where ZF was used to decode the UL received signal. For all scenarios in this section, the error in the channel estimation between the UEs and the BS is modeled as a complex Gaussian distribution $\sim \mathscr{CN}\left(\mathbf{0}, \sigma_e^2 \boldsymbol{I}_M\right)$ [114]. In the first scenario, $\sigma_e^2 = 0.045$ (4.5%) was introduced to the system when M=128 and M=64. Then σ_e^2 was decreased to 0.0128 (1.28%) and 0.0018 (0.18%) for the second and the third scenario respectively.

The EVM performance for the three different scenarios is shown in Figure 5.13 for an increasing number of users, where the SNR value is maintained at 30dB. Based on the 3GPP LTE standards [94], the required EVM for 64 QAM is 8% [94] so the maximum number of users that can be served with 64 QAM simultaneously in the 1st scenario is 13 and 9 when M=128 and M=64 respectively. Because of the channel hardening, 4 additional users were served by increasing M from 64 to 128. In the second scenario, 22 and 16 users can be served simultaneously when M=128 and M=64 respectively. Since σ_e^2 was decreased, the interference from the cumulative error amplification part in (4.5) was decreased as well. This allows the BS to serve more users in the second scenario which increases the sum rate and the SE. In the third scenario, all users were served simultaneously when M=128 and M=64. The overall SE can be increased by adding more users or using a higher MCS when EVM permits. The required EVM to achieve 256 QAM is 3.5% [94].

For a more comprehensive analysis, the EVM was plotted for the three scenarios in Figure 5.14, where 22 users were served simultaneously with an SNR range between 0 to 50 dB. In the first scenario, the BS can't serve all the 22 users simultaneously with 64QAM by simply increasing the SNR. In the second scenario, all users can be served simultaneously only when M=128 and SNR $\geq$ 35 dB. For the third scenario, all users can be served simultaneously when SNR $\geq$ 25 dB and SNR $\geq$ 35 dB for M=128 and M=64 dB respectively. 256 QAM can be achieved only in the third scenario where SNR $\geq$ 35 dB.

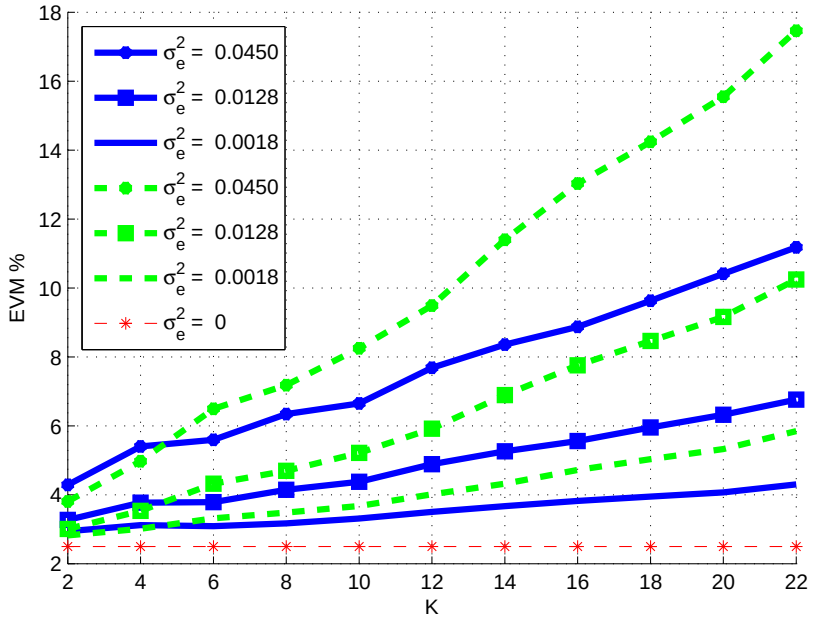

Figure 5.13: EVM vs K when SNR = 30 dB. Blue and green curves are the EVM values when M=128 and M=64 respectively. Red curve is the EVM with perfect channel estimation.

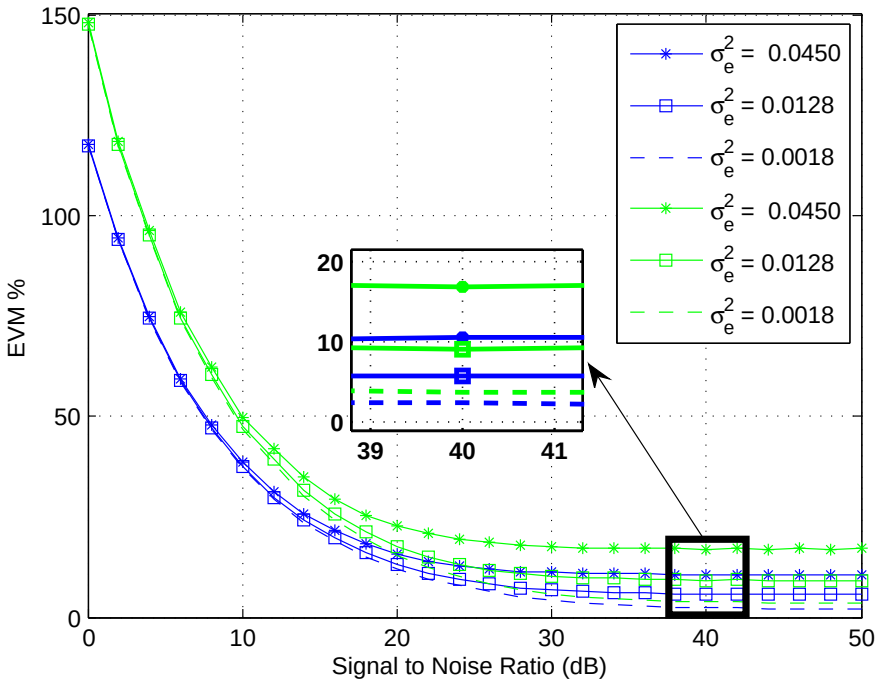

Figure 5.14: EVM performance with 22 users. Blue and green curves are the EVM values when M=128 and M=64 respectively.

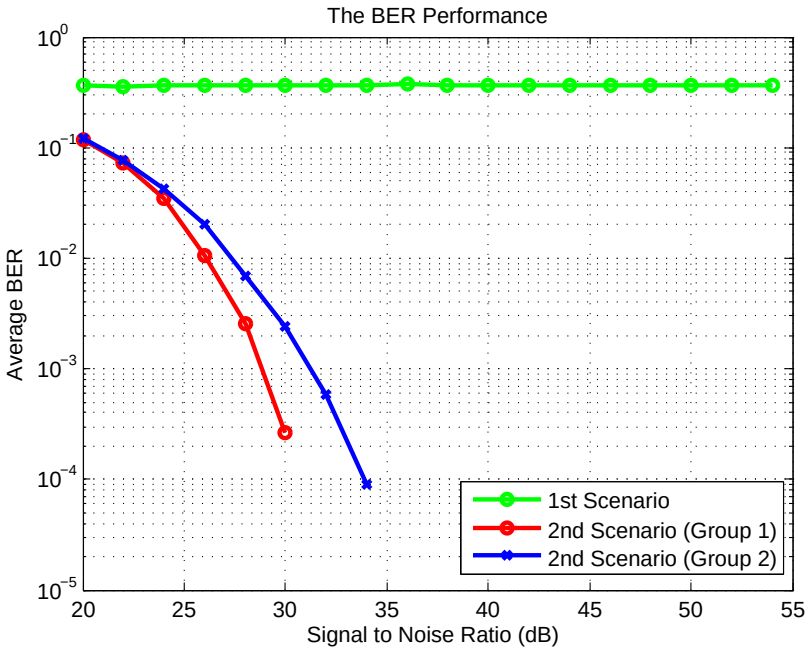

Figure 5.15: Average BER performance using ZF with 64 QAM (LOS outdoor environment).

5.2.2 Outdoor Environment

In a LOS outdoor environment with low scatterers, the need for user grouping is even more substantial as the pairwise orthogonality of the user channel vectors is low compared to an indoor environment as it was shown in section 3.2.6. The outdoor channel from the trial in section 3.2.6.2 was used in the Ma-MIMO simulator with ZF to illustrate the need for dividing users. Two different scenarios were considered, where M=100 and K=8. The error in the channel estimation between the UEs and the BS is modeled as a complex Gaussian distribution $\sim \mathcal{CN}\left(\mathbf{0}, \sigma_e^2 \boldsymbol{I}_M\right)$ where $\sigma_e^2 = 1\%$ was introduced to the system in both scenarios. In the first scenario, all users were served simultaneously. While in the second scenario, users were divided to two groups where each user from the same USRP was assigned into different group to decrease the interference between the users (the highest spatial correlation between any two users was achieved by serving two users from the same USRP due to the narrow separation distance between them compared to other users from different USRPs). Figure 5.15 shows the average BER performance when 64 QAM was used for the both scenarios. The green curves is the average BER performance when all users were served simultaneously. The average BER is always 50% even by increasing the SNR value. The blue and the red curves are the average BER for the second scenario, where each color represents a different group. When the SNR was 20 dB, the average BER for group 1 and 2 was 10%. When theSNR was increased to 35 dB, the average BER becomes zero for both groups. Dividing users into different groups has established a reliable data transmission without the need for using a lower MCS order. Therefore finding a proper way for dividing users is necessary to establish reliable data transmission and choosing the right MCS order.

5.3 User Grouping Algorithms

The need for user grouping in a single cell Ma-MIMO is illustrated in section 5.2 and experimentally demonstrated in chapter 4 for both UL and DL data transmission. The proposed user grouping algorithm in this section mitigates the interference from the estimated channel coefficients between users and also the interference caused by inaccurate CSI. Here, this is uniquely achieved by extracting the EVM, and three different methodologies are applied to address specific wireless connectivity objectives. The user grouping algorithm is based on the spatial correlation between users and the EVM metric. A different number of groups could be assigned for UL and DL data transmission since they have different CSI accuracies. Three approaches to user grouping are presented in this chapter to cover different applications' requirements. In UL, the EVM threshold (EVM^{TH}) value for each MCS order follows the 3GPP requirement in [94]. While in DL, the EVM^{TH} are increased based on feedback from the user side. Since the grouping decision is decided based on the $\widetilde{\widetilde{\text{EVM}}}$ at the BS side, the increment in the EVM^{TH} for DL covers the interference caused by the reciprocity calibration error (ex: EVM^{TH} can be increased from 8% based on [94] to 12% based on user's feedback). The proposed algorithm works according to the fixed frame structure the Ma-MIMO is already using, which aligns with the concept of adopting predefined frame structure in LTE.

Definition 5.3.1. *$\nu(\mathscr{A},k)$ is the average $\widetilde{\widetilde{EVM}}$ for the total number of users $\tilde{K}$, where:*

- *$\mathscr{A}$ is a group of users.*
- *k the candidate user to join the group $\mathscr{A}$.*
- *$\tilde{K}$ is the total number of users in the set ($\mathscr{A} \cup \{k\}$).*
- $\nu(\mathscr{A},k) = \frac{1}{\tilde{K}} \sum_{i=1}^{\tilde{K}} \widetilde{\widetilde{EVM}}_i^2$.

Definition 5.3.2. *The predicted SE ($\widetilde{\widetilde{SE}}$) is the estimated SE for a set of users calculated by using the highest MCS mode the $\widetilde{\widetilde{EVM}}$ allows. This calculations are under an error free assumption considering 3/4 rate LDPC [121].*

Definition 5.3.3. *$\psi(\mathscr{A},k)$ is the $\widetilde{\widetilde{SE}}$ for a set of users in group $\mathscr{A}$ and the candidate user to join the group (k), where the $\widetilde{\widetilde{EVM}}$ for each user is calculated based on new set of users ($\mathscr{A} \cup \{k\}$).*

5.3.1 Maximizing Spectral Efficiency

This approach is suitable for cellular networks, where radio resources need to be used more efficiently. The number of groups is decided based on the $\widetilde{\widetilde{\text{SE}}}$ calculations described in Algorithm 2 where only one group is used. $\mathscr{U}$ is a set of un-assigned UEs waiting to be assigned into group $\mathscr{A}$. At first, the two users with the lowest spatial correlation are assigned to $\mathscr{A}$ then only one

user is added to the group at each user assigning step. Based on the EVM requirements, the highest MCS mode is used to calculate the $\widetilde{\widetilde{\text{SE}}}$ at each user assigning step. The maximum $\widetilde{\widetilde{\text{SE}}}$ for different sets of users is saved in the vector $\widetilde{\widetilde{\boldsymbol{se}}}$ where each index of the vector is equal to the total number of users in the equivalent set of users. $\widetilde{\widetilde{\widetilde{\boldsymbol{evm}}}}$ is a vector of the lowest average $\widetilde{\widetilde{\widetilde{\text{EVM}}}}$ for different sets of users where each index of the vector is equal to the total number of users in the equivalent set. After obtaining the required information from Algorithm 2, the UEs are assigned to different groups based on Algorithm 3. If the maximum $\widetilde{\widetilde{\text{SE}}}$ is achieved by serving all users, then only one group is required. Otherwise, the number of groups is obtained from dividing the total number of users by the number of users which maximized the $\widetilde{\widetilde{\text{SE}}}$. The number of groups is rounded up to the next integer number. $\mathscr{G}$ is the group vector where the index of the vector represents the group number and each group contains a set of users. Users are assigned into one of the groups $\mathscr{G}_n$ where $n \in \{1,...,\text{total number of groups}\}$. Users with the highest spatial correlation are first assigned into different groups. Then the rest of the users are assigned to the group based on maximizing the $\widetilde{\widetilde{\text{SE}}}$ and minimizing the average $\widetilde{\widetilde{\widetilde{\text{EVM}}}}$. As the number of groups is a result of rounding-up, some users might be assigned into more than one group. Users will stop being assigned into a groups when the $\widetilde{\widetilde{\text{SE}}}$ of that group starts decreasing.

5.3.2 Maximizing Number of Simultaneous Users

This approach is more suitable for IoT applications, since it maximizes the number of users and does not require a high throughput value. Here, only QPSK is considered. Initially, only one group is required, with more groups created later as necessary. The number of groups is decided based on the $\widetilde{\widetilde{\widetilde{\text{EVM}}}}$ calculations described in Algorithm 4 where only one group is used. The users are assigned in the order in which the lowest average $\widetilde{\widetilde{\widetilde{\text{EVM}}}}$ is achieved and saved in the $\widetilde{\widetilde{\widetilde{\boldsymbol{evm}}}}$ vector at each user assigning step. In this approach, the number of groups and the users' assigning process is described in Algorithm 5, where the EVM^{TH} is equal to the EVM requirements for QPSK (EVM^{QPSK}). If $\widetilde{\widetilde{\widetilde{\boldsymbol{evm}}}}_K$ is less than the EVM^{QPSK}, then only one group is required. Otherwise, number of groups is obtained from dividing the total number of users by the index number of the highest element's value in the vector $\widetilde{\widetilde{\widetilde{\boldsymbol{evm}}}}$, while taking into account the QPSK EVM requirements. This allows us to serve the largest possible number of users in the same group without exceeding the EVM requirements of the targeted MCS. The number of groups is rounded up to the next integer number. Users with the highest spatial correlation are first assigned into different groups. Then the rest of the users are assigned to the group based on minimizing the average $\widetilde{\widetilde{\widetilde{\text{EVM}}}}$. If all the users' $\widetilde{\widetilde{\widetilde{\text{EVM}}}}$ values are less than the EVM value required for QPSK MCS, then the number of groups won't change. Otherwise, an additional group is created as described in Algorithm 5. As the number of groups is a result of rounding-up, some users might be assigned into more than one group. Users will stop being assigned into a group if the $\widetilde{\widetilde{\widetilde{\text{EVM}}}}$ of any user in that group becomes greater than the EVM^{QPSK}. BPSK can also be used

Algorithm 2: to Perform $\widetilde{\widetilde{SE}}$ Calculations for the Maximizing Spectral Efficiency Algorithm

set $\mathscr{U} = \{1,...,K\}, \mathscr{A} = \{\}, \boldsymbol{G} = \left|\hat{\boldsymbol{H}}_{ul}^{H}\hat{\boldsymbol{H}}_{ul}\right|$
Find the lowest correlation value: $g_{i,j}$
$\widetilde{\widetilde{\boldsymbol{se}}}_1 = \psi(\mathscr{A}, \mathscr{U}_i)$, then $\mathscr{A} = \mathscr{A} \cup \{\mathscr{U}_i\}$.
$\widetilde{\widetilde{\boldsymbol{se}}}_2 = \psi\left(\mathscr{A}, \mathscr{U}_j\right)$, then $\mathscr{A} = \mathscr{A} \cup \{\mathscr{U}_j\}$.
Remove $\mathscr{U}_i$&$\mathscr{U}_j$from $\mathscr{U}$
for $l = 3 : K$ **do**
    set $r = 0, T = \{1,...,K-l+1\}$.
    for $k = l : K$ **do**
        $r = r + 1$.
        $\widetilde{\widetilde{\boldsymbol{se}}}_r^{tmp} = \psi(\mathscr{A}, \mathscr{U}_r)$
        $\widetilde{\widetilde{\boldsymbol{evm}}}_r^{tmp} = \nu(\mathscr{A}, \mathscr{U}_r)$
        $UE_r = \mathscr{U}_r$
    end
    $p \leftarrow \text{argmax}_{p \in T} \widetilde{\widetilde{\boldsymbol{se}}}_p^{tmp}$
    $s \leftarrow \text{argmin}_{s \in T_p} \widetilde{\widetilde{\boldsymbol{evm}}}_s^{tmp}$
    if *p is one element* **then**
        $\widetilde{\widetilde{\boldsymbol{se}}}_l = \widetilde{\widetilde{\boldsymbol{se}}}_p^{tmp}$.
        $\mathscr{A} = \mathscr{A} \cup \{UE_p\}$
        Remove $\mathscr{U}_p$ from $\mathscr{U}$
    else
        $\widetilde{\widetilde{\boldsymbol{se}}}_l = \widetilde{\widetilde{\boldsymbol{se}}}_s^{tmp}$.
        $\mathscr{A} = \mathscr{A} \cup \{UE_s\}$
        Remove $\mathscr{U}_s$ from $\mathscr{U}$
    end
    clear $\widetilde{\widetilde{\boldsymbol{se}}}^{tmp}, \widetilde{\widetilde{\boldsymbol{evm}}}^{tmp}$.
end

Algorithm 3: User Grouping for Maximizing SE

$\mathscr{U} = \{1,...,K\}, \mathscr{G} = \{\}, \boldsymbol{G} = \left|\hat{\boldsymbol{H}}_{ul}^{H}\hat{\boldsymbol{H}}_{ul}\right|$.

$v \leftarrow \text{argmax}_{v\in\mathscr{U}}\widetilde{\widetilde{\boldsymbol{se}}}_v$

if $v = K$ **then**

  Exit Algorithm

end

$N = \lceil K/v \rceil$, set $T = \{1,...,N\}$

%Assigning one user for each group

for $n = 1 : \lceil N/2 \rceil$ **do**

  Find the highest correlation value: $g_{i,j}$

  if $n = \lceil N/2 \rceil \neq N/2$ **then**

    $l \leftarrow \text{argmin}_{l\in\{i,j\}}\widetilde{\widetilde{\widetilde{EVM}}}_l$

    $\mathscr{G}_{(n\times 2)-1} = \mathscr{G}_{(n\times 2)-1} \cup \{\mathscr{U}_l\}$

    Remove $\mathscr{U}_l$ from $\mathscr{U}$

  else

    $\mathscr{G}_{(n\times 2)-1} = \mathscr{G}_{(n\times 2)-1} \cup \{\mathscr{U}_i\}$

    $\mathscr{G}_{(n\times 2)} = \mathscr{G}_{(n\times 2)} \cup \{\mathscr{U}_j\}$

    $g_{i,j} = 0$, Remove $\mathscr{U}_i$&$\mathscr{U}_j$ from $\mathscr{U}$

  end

end

%Assigning the remaining users to one of the groups

for $k = 1 : (K - N)$ **do**

  $l \leftarrow \text{argmax}_{l\in T}\psi\left(\mathscr{G}_l, \mathscr{U}_k\right)$

  $p \leftarrow \text{argmin}_{p\in T_l}\nu\left(\mathscr{G}_p, \mathscr{U}_k\right)$

  if *l is one element* **then**

    $\mathscr{G}_l = \mathscr{G}_l \cup \{\mathscr{U}_k\}$

  else

    $\mathscr{G}_p = \mathscr{G}_p \cup \{\mathscr{U}_k\}$

  end

  Remove $\mathscr{U}_k$ from $\mathscr{U}$

end

Assigning some users to more than one group in order to maximise the capacity of each group.

instead of QPSK based on the application requirements.

Algorithm 4: to Perform $\widetilde{\widetilde{\text{EVM}}}$ Calculations for the Maximizing Number of Simultaneous Users and the Link Quality Algorithms.

set $\mathscr{U} = \{1,...,K\}, \mathscr{A} = \{\}, \boldsymbol{G} = \left|\hat{\boldsymbol{H}}_{ul}^{H} \hat{\boldsymbol{H}}_{ul}\right|$
Find the lowest correlation value: $g_{i,j}$
$\widetilde{\widetilde{\boldsymbol{evm}}}_1 = \nu(\mathscr{A}, \mathscr{U}_i)$, then $\mathscr{A} = \mathscr{A} \cup \{\mathscr{U}_i\}$.
$\widetilde{\widetilde{\boldsymbol{evm}}}_2 = \nu\left(\mathscr{A}, \mathscr{U}_j\right)$, then $\mathscr{A} = \mathscr{A} \cup \{\mathscr{U}_j\}$.
Remove $\mathscr{U}_i$&$\mathscr{U}_j$from $\mathscr{U}$
for $l = 3 : K$ **do**
    set $r = 0, T = \{1,...,K-l+1\}$.
    for $k = l : K$ **do**
        $r = r + 1$.
        $\widetilde{\widetilde{\boldsymbol{evm}}}_r^{tmp} = \nu(\mathscr{A}, \mathscr{U}_r)$
        $UE_r = \mathscr{U}_r$
    end
    $s \leftarrow \text{argmin}_{s \in T} \widetilde{\widetilde{\boldsymbol{evm}}}_s^{tmp}$
    $\widetilde{\widetilde{\boldsymbol{evm}}}_l = \widetilde{\widetilde{\boldsymbol{evm}}}_s^{tmp}$.
    $\mathscr{A} = \mathscr{A} \cup \{UE_s\}$
    Remove $\mathscr{U}_s$ from $\mathscr{U}$
    clear $\widetilde{\widetilde{\boldsymbol{evm}}}^{tmp}$.
end

5.3.3 Link Quality

This approach is suitable for applications that require maintaining the throughputs per user above a certain threshold or maintaining bit error rates below a predetermined threshold. As an example, consider wireless cameras at a major sporting or cultural event, where each camera requires minimum throughput value to support Ultra-High-Definition (UHD) quality for the video stream.

Similar to the Maximizing Number of Simultaneous Users approach, this commences with only one group and more groups can be created later if necessary. The number of groups is decided based on the $\widetilde{\widetilde{\text{EVM}}}$ calculations described in Algorithm 4 and the user assigning process is described in Algorithm 5. Unlike the previous approach, the EVM^{TH} is pre-determined based on increasing the minimum achievable throughput per user. In this approach the EVM^{TH} value doesn't have to comply with the 3GPP EVM requirements.

Algorithm 5: User Grouping for the Maximizing number of Simultaneous Users & the Link Quality Algorithms.

$\mathscr{U} = \{1,...,K\}, \mathscr{G} = \{\}, \boldsymbol{G} = \left|\hat{\boldsymbol{H}}_{ul}^{H}\hat{\boldsymbol{H}}_{ul}\right|$.

$v \leftarrow \text{argmax}_{v\in\mathscr{U}}\widetilde{\widetilde{\boldsymbol{evm}}}_v$, subject to $\left(\widetilde{\widetilde{\boldsymbol{evm}}}_v < \text{EVM}^{\text{TH}}\right)$

if $v = K$ **then**
  Exit Algorithm
end

$N = \lceil K/v \rceil$, set $T = \{1,...,N\}$

%Assigning one user for each group

for $n = 1 : \lceil N/2 \rceil$ **do**
  Find the highest correlation value: $g_{i,j}$
  if $(n = \lceil N/2 \rceil)\&(n \ odd \ number)$ **then**
    $l \leftarrow \text{argmin}_{l\in\{i,j\}}\widetilde{\widetilde{EVM}}_l$
    $\mathscr{G}_N = \mathscr{G} \cup \{\mathscr{U}_l\}$
    Remove $\mathscr{U}_l$ from $\mathscr{U}$
  else
    $\mathscr{G}_{(n\times 2)-1} = \mathscr{G}_{(n\times 2)-1} \cup \{\mathscr{U}_i\}$
    $\mathscr{G}_{(n\times 2)} = \mathscr{G}_{(n\times 2)} \cup \{\mathscr{U}_j\}$
    $g_{i,j} = 0$, Remove $\mathscr{U}_i \& \mathscr{U}_j$ from $\mathscr{U}$
  end
end

%Assigning the remaining users to one of the groups

for $k = 1 : (K - N)$ **do**
  $p \leftarrow \text{argmin}_{p\in T}\, v\left(\mathscr{G}_p, \mathscr{U}_k\right)$
  $\mathscr{G}_{p_1} = \mathscr{G}_{p_1} \cup \{\mathscr{U}_k\}$ ▷ if p is not one element, select p_1
  Remove $\mathscr{U}_k$ from $\mathscr{U}$
end

%Checking the EVM requirements for all users

if *any* $\widetilde{\widetilde{EVM}} > EVM^{req}$ **then**
  $N = N + 1, \mathscr{U} = \{1,...,K\}, \mathscr{G} = \{\}, \boldsymbol{G} = \left|\hat{\boldsymbol{H}}_{ul}^{H}\hat{\boldsymbol{H}}_{ul}\right|$
  Go to 7
end

Assigning some users to more than one group until the $\widetilde{\widetilde{EVM}}$ for any user become greater than EVM^{req} .

5.4 Results from Massive MIMO Simulator

In this section, the error in the reciprocity calibration matrix and the error in the channel estimation between the UEs and the BS are modelled in the Ma-MIMO simulator as a complex Gaussian distribution [130] [114] with an error variance of 0.02 (2%) and 0.01 (1%) used for each of them respectively. Whilst this value may be higher or lower and the model may not be so accurate in reality, it serves to illustrate the potential effects of CSI inaccuracies in Ma-MIMO. 3/4 rate LDPC code was used in the simulator. The same frame schedule used in section 4.7 was used here.

For the "link quality" approach, the EVM^{TH} value was selected to be below 3.5% to enable reliable data transmission with a minimum throughput of 80 Mbits/s for each user by using 256-QAM. For comparison purposes, two additional methods are considered. In the first method, two groups are created and users are assigned in an order where the minimum sum correlation is applied to minimize the IUI damage with each new user joining the group. In this section, this method is called "spatial correlation" where the assigning process relies only on the spatial correlation between the users. In the second method, the user grouping algorithm is deactivated and all users are served simultaneously using the highest MCS order the EVM value permits. These two additional methods cover the total number of groups created after using the "maximizing SE" approach as shown later in section 5.4.2 allowing us a fair SE comparison.

5.4.1 Channel Conditions

The proposed user grouping algorithms are applied using the Ma-MIMO simulator with the following channel conditions:

- IID channels: Four different scenarios were considered using IID channels, where M=128 and M=64 were used in the 1^{st} and the 2^{nd} scenarios respectively, while K=22 in both scenarios. These scenarios are similar to the ones used in the LOS measured indoor channels. In the 3^{rd} and 4^{th} scenarios, K was increased to 40 users, where M=128 and M=64 respectively.

- LOS measured indoor channels: The real channels captured from the trial described in section 4.1 were used. Two scenarios were considered in the Ma-MIMO simulator using these channels where M=128 and M=64 for each scenario respectively, while K=22 in both scenarios.

- LOS measured outdoor channels: Real channels captured from the trial described in section 3.2.6.2 were used. Two scenarios were considered in the Ma-MIMO simulator using the channels captured from this trial where M=100 and M=64 for each scenario respectively, while K=8 in both scenarios.

5.4.2 Results

Table 5.1 shows the number of groups, the maximum EVM values and the SE which resulted from each of the three proposed user grouping approaches using the 1^{st} scenario of the IID channels. It also shows the results when the spatial correlation method was used and when the user grouping algorithms were disabled. For maximizing the UL SE, 2 groups were used in 1^{st} scenario. Each group served 19 users with 256-QAM and the correspondent UL SE was 83.9 bits/s/Hz, where some users were assigned to both groups. If any additional user was assigned to any of the groups, 64-QAM would have been used and the UL SE would have decreased to 72.86 bits/s/Hz (since the EVM value becomes greater than 3.5%, which is the EVM threshold for using 256-QAM [94]). For maximizing the DL SE, 1 group only was used achieving 72.86 bits/s/Hz by using 64-QAM. When the "link quality" approach was used, the results was similar to the maximizing SE approach on UL data transmission. While in the DL data transmission, 8 groups were needed to maintain the EVM value below 3.5% and the throughput above 80 Mbits/s for each user providing the required data transmission quality. By using the "maximizing number of simultaneous users" approach, all users were served within one group in the UL and the DL data transmission, where 64-QAM was used. When the "spatial correlation" method was used, users were assigned to the groups based only on the spatial correlation. After the first data transmission interval, the highest MCS order were used based on the measured EVM values. By using the proposed "maximizing SE" approach, the UL SE was increased by 35.33 bits/s/Hz and 11.04 bits/s/Hz compared to the "spatial correlation" and "deactivating user grouping" methods respectively. While the DL SE was increased by 36.43 bits/s/Hz compared to the "spatial correlation" method. The $\widetilde{\text{EVM}}$ value allow the system to find the number of groups and the number of users in each group needed to establish the required data transmission.

Table 5.1: User grouping parameters: results for M=128 and K=22 (1^{st}scenario: IID Rayleigh Channels.)

	Max EVM%		Number of Groups		SE (b/s/Hz)	
	UL	DL	UL	DL	UL	DL
Maximizing SE	3.4	6.2	2	1	83.9	72.86
Link quality	3.4	3.4	2	8	83.9	13.24
Maximizing number of simultaneous users	4.2	6.2	1	1	72.86	72.86
Spatial Correlation	2.2	6.1	2	2	48.57	36.43
Deactivate user grouping	4.2	6.2	1	1	72.86	72.86

When K was increased to 40 and M was decreased to 64, the proposed algorithms created different number of groups based on the desired goal as it is shown in Table 5.4. By using the "maximizing SE" approach, the UL SE was increased by 33.12 bits/s/Hz and 11.04 bits/s/Hz compared to the "spatial correlation" and "deactivating user grouping" methods respectively.

Table 5.2: User grouping parameters: results for M=64 and K=22 (2^{nd}scenario: IID Rayleigh Channels.)

	Max EVM%		Number of Groups		SE (b/s/Hz)	
	UL	DL	UL	DL	UL	DL
Maximizing SE	6.5	7.9	1	2	72.86	49.68
Link quality	3.4	3.1	4	11	30.91	8.83
Maximizing number of simultaneous users	6.5	11.2	1	1	72.86	48.57
Spatial Correlation	5.1	7.6	2	2	36.43	36.43
Deactivate user grouping	6.5	11.2	1	1	72.86	48.57

Table 5.3: User grouping parameters: results for M=128 and K=40 (3^{rd}scenario: IID Rayleigh Channels.)

	Max EVM%		Number of Groups		SE (b/s/Hz)	
	UL	DL	UL	DL	UL	DL
Maximizing SE	6.2	7.7	1	2	132.48	96.05
Link quality	3.3	3.8	3	14	83.9	13.24
Maximizing number of simultaneous users	6.9	10.9	1	1	132.48	88.32
Spatial Correlation	4.9	7.9	2	2	66.24	66.24
Deactivate user grouping	6.2	10.9	1	1	132.48	88.32

Table 5.4: User grouping parameters: results for M=64 and K=40 (4^{th}scenario: IID Rayleigh Channels.)

	Max EVM%		Number of Groups		SE (b/s/Hz)	
	UL	DL	UL	DL	UL	DL
Maximizing SE	7.6	10.8	2	2	99.36	61.82
Link quality	3.3	3.2	7	20	26.49	8.83
Maximizing number of simultaneous users	11.8	16.5	1	2	88.32	75.07
Spatial Correlation	6.8	11.2	2	2	66.24	44.61
Deactivate user grouping	11.8	23	1	1	88.32	0

While the DL SE was increased by 17.21 bits/s/Hz compared to the "spatial correlation" method. When disabling the user grouping algorithms, zero throughput in DL data transmission was achieved due to the very large EVM value. When the LOS measured indoor channels were used, the spatial correlation between users was increased. Table 5.5 and Table 5.6 show the number of groups, the maximum EVM values and the SE which resulted from each user grouping approach. When using the LOS measured outdoor channels, the spatial correlation between users was

increased even further. Table 5.7 and Table5.8 show the number of groups, the maximum EVM values and the SE which resulted from each user grouping approach. The proposed user grouping algorithms consider the interference caused by the high spatial correlation and the impact of high spatial correlation on inaccurate CSI. The maximum SE was always achieved by using the "Maximizing SE" algorithm. The "link quality" approach maintained the EVM value below

Table 5.5: User grouping parameters: results for M=128 and K=22 (1^{st}scenario: LOS Measured indoor Channels).

	Max EVM%		Number of Groups		SE (b/s/Hz)	
	UL	DL	UL	DL	UL	DL
Maximizing SE	6.5	7.9	1	2	72.86	62.93
Link quality	3.3	3.4	3	8	39.744	13.24
Maximizing number of simultaneous users	7	10.2	1	1	72.86	48.57
Spatial Correlation	4.9	7	2	2	36.42	36.42
Deactivate user grouping	6.5	10.2	1	1	72.86	48.57

Table 5.6: User grouping parameters: results for M=64 and K=22 (2^{nd}scenario: LOS Measured indoor Channels).

	Max EVM%		Number of Groups		SE (b/s/Hz)	
	UL	DL	UL	DL	UL	DL
Maximizing SE	7.9	10.6	2	2	62.93	39.74
Link quality	3.4	3.6	5	11	22.08	8.83
Maximizing number of simultaneous users	10.3	17	1	1	48.57	24.28
Spatial Correlation	7.5	10.4	2	2	36.42	24.28
Deactivate user grouping	10.3	17	1	1	48.57	24.28

Table 5.7: User grouping parameters: results for M=100 and K=8 (1^{st}scenario: LOS Measured outdoor Channels).

	Max EVM%		Number of Groups		SE (b/s/Hz)	
	UL	DL	UL	DL	UL	DL
Maximizing SE	7.1	8.2	1	2	26.49	23.18
Link quality	2.8	3	4	4	8.83	8.83
Maximizing number of simultaneous users	7.1	9.8	1	1	26.49	17.66
Spatial Correlation	3.3	5.9	2	2	17.66	13.24
Deactivate user grouping	7.1	9.8	1	1	26.49	17.66

Table 5.8: User grouping parameters: results for M=64 and K=8 (2^{nd}scenario: LOS Measured outdoor Channels).

	Max EVM%		Number of Groups		SE (b/s/Hz)	
	UL	DL	UL	DL	UL	DL
Maximizing SE	7.9	7.7	1	2	26.49	19.87
Link quality	3.1	3.4	4	4	8.83	8.83
Maximizing number of simultaneous users	7.9	11	1	1	26.49	17.66
Spatial Correlation	5	7	2	2	13.24	13.24
Deactivate user grouping	7.9	11	1	1	26.49	17.66

3.5% providing a minimum throughput of 80 Mbits/s for each user by using 256-QAM. While the "maximizing number of simultaneous users" algorithm managed to serve the maximum number of users simultaneously using the same radio resources.

5.5 Experimental Campaigns & User Grouping

The experimental evaluation was a part of the UK 5G Test-beds and trials program [122]. Funded by the UK Government's DCMS, this event was the world's first urban 5G showcase[1]. In all the considered scenarios, UL power control was used to adjust the UL transmit power so the received SNR from all users was the same.

5.5.1 Trial Environment

The 5G showcase took place at Millennium Square in Bristol. The balcony of 'We The Curious' building was used to deploy the BS to serve 12 user clients placed 37.5m away down in the square. The Ma-MIMO system operated at a 3.51 GHz carrier frequency sharing a common 20MHz radio channel. The patch panel antenna array was setup in a 4x32 configuration with vertical polarisations for all 128 antennas. User clients' antennas were in LOS and were mounted outside along the top edge of the marquee in a straight line with 432mm spacing as shown in Figure 5.16.

5.5.2 Frame Schedule

The PHY frame schedule used for the system is shown in Figure 5.17. In the experimental campaigns, the frame schedule was configured to use one UL pilot, five UL data and one guard on the first half subframe followed by DL pilot, five DL data and one guard on the second half subframe. The first half OFDM subframe is for synchronization to achieve sample alignment.

[1]A video about the world's first urban 5G showcase is available at https://www.youtube.com/watch?v=7Qzv_TtyKMU

Figure 5.16: Outdoor trial environment with the 12 UEs 36.5m away.

5.5.3 Real-time Results

During the 5G showcase, a total of 24 HD videos were streamed in real-time in both UL and DL. In order to establish reliable live HD video streams, the proposed user grouping algorithm in this article was used. The "link quality" approach was selected to maintain the EVM value below 13%. This EVM threshold with QPSK MCS was sufficient to deliver the required real-time uncoded throughputs for each user with tolerable error level. The performance of the two other user grouping approaches were evaluated as well. Table 5.9 shows the number of groups, the maximum EVM values and the MCS which resulted from each of the three user grouping approaches. It also shows the MCS and the maximum EVM values when the user grouping algorithms were disabled.

For maximizing the SE, 4 and 6 groups were used for UL and DL scenarios respectively. The correspondent SE was 12.3 bits/s/Hz as it is shown in Table 5.10. When the "link quality" approach was used, the SE was decreased by 2.9 bits/s/Hz. This is because the aim of this approach is to maintain the EVM value below 13% to provide reliable uncoded video streams using QPSK, which was successfully established in the field. By using the "maximizing number of simultaneous users" approach, all users were served within one group in the UL data transmission and within 3 groups in the DL data transmission. Although more users were served with QPSK using the same radio resources, the uncoded throughput was decreased compared to the "link quality" approach. Since the Ma-MIMO testbed was not using any error correcting code, the errors corresponded to the high EVM values decreased the uncoded throughput. The lowest uncoded throughput was achieved by disabling the proposed user grouping algorithm. This led into zero throughput in DL data transmission due to the very large EVM value.

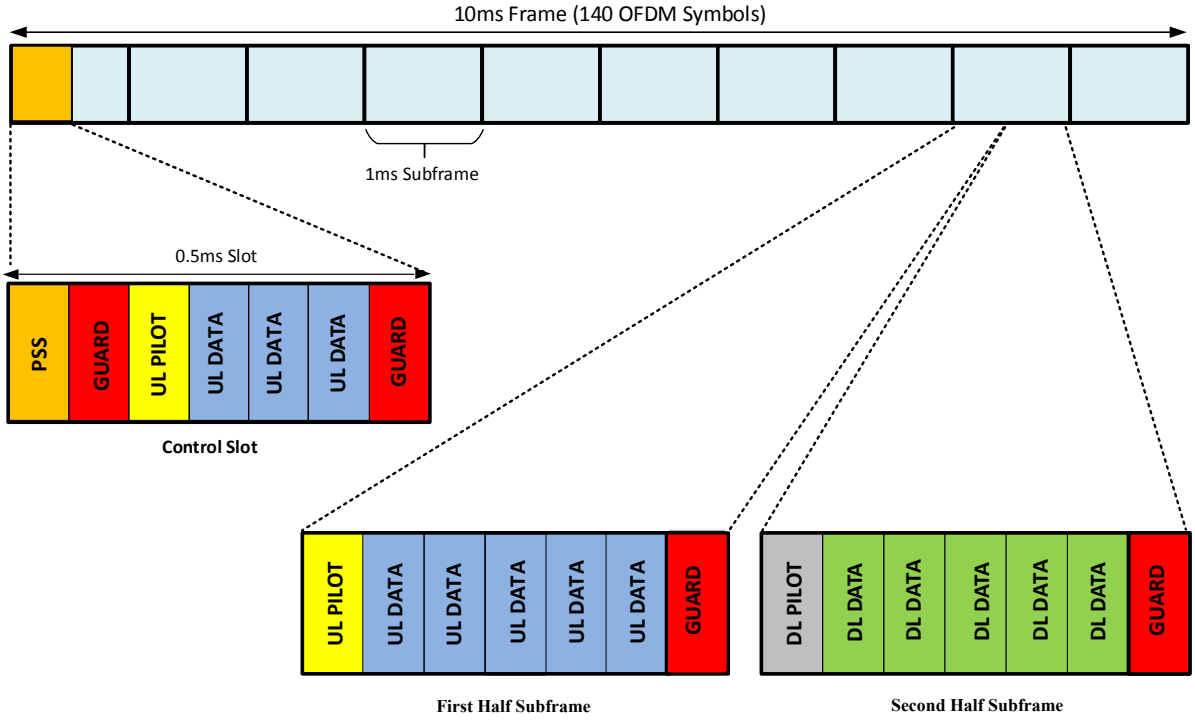

Figure 5.17: Frame Schedule.

Table 5.9: User grouping parameters results.

	Max EVM%		Number of Groups		MCS (2^b) $b=$	
	UL	DL	UL	DL	UL	DL
Maximizing SE	6	8	4	6	6	4
Link quality	12	12	2	4	2	2
Maximizing number of simultaneous users	16	16	1	3	2	2
Deactivate user grouping	16	35	1	1	2	2

Table 5.10: Trial throughputs and spectral efficiency results using user grouping algorithms.

	Uncoded UL throughput (Mbps)	Uncoded DL throughput (Mbps)	SE (b/s/Hz)
Maximizing SE	182	64	12.3
Link quality	135.3	53.2	9.4
Maximizing number of simultaneous users	84	58.6	7.1
Deactivate user grouping	84	0	4.2

By comparing the results obtained in this outdoor LOS real-time trial to the one in section

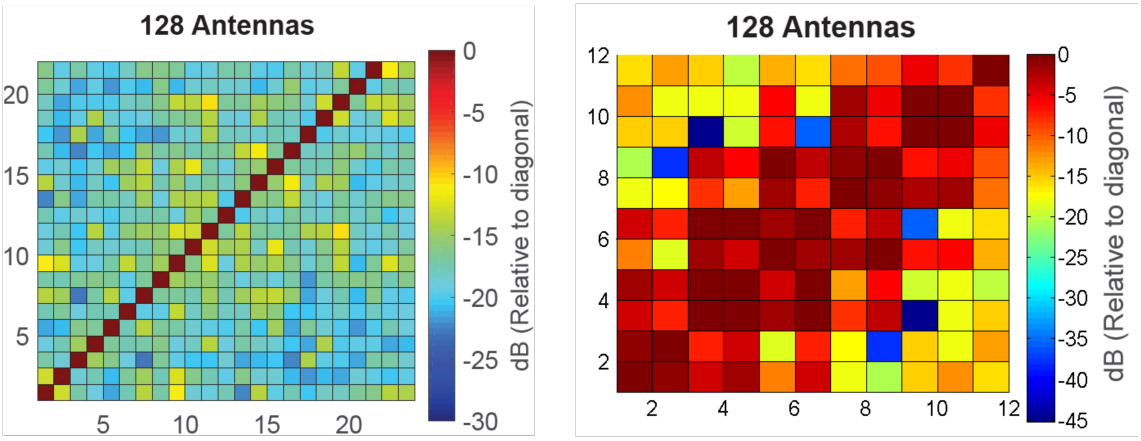

Figure 5.18: User-side Gramian intensity plots. Left, indoor trial with 22 UEs. Right, outdoor trial with 12 UEs.

4.1, performance degradation can be observed. The maximum uncoded throughput and the maximum SE were decreased by 1.664 Gbps and 133.3 bits/s/Hz respectively. Two main reasons are behind this performance degradation. First, the rich multipath scattering in an indoor environment creates a greater level of pairwise orthogonality between the user channel vectors and thus increases the achievable capacity. While in an outdoor environment where the LOS is the dominant signal, lower pairwise orthogonality is achieved between the user channel vectors. This can be seen in Figure 5.18, where the user-side Gramian matrix for the LOS indoor environment in [31] is on the left and the LOS outdoor environment from the 5G showcase is on the right. The high spatial correlation level between users in the outdoor environment increases the interference between users. This will either decrease the number of users that are using the same radio resources or the MCS order. The second main reason behind the performance degradation is the accuracy of the CSI. The distance between the users and the BS in the indoor environment trial was 24.8m. While in the outdoor trial the distance was increased by 11.7m. The maximum mean power level used in both trials for UL transmission was -16 dBm. By increasing the distance between the users and the BS, the CSI accuracy was decreased because of the noise floor effect on the pilots during the channel estimation process. This increased the interference level between users which decreased the uncoded throughput and SE.

5.6 Summary

In this chapter, adaptive user grouping algorithms for a single cell were proposed to enhance Ma-MIMO performance for different service types. Three different approaches were introduced for assigning users into different groups to establish the data transmission requirements for different

applications such as cellular networks, IoT and wireless cameras. The proposed algorithms are based on the novel EVM prediction method proposed in this chapter jointly relying on the channel correlation between users and the EVM performance which are the key elements behind ensuring reliable data transmission and increasing the system throughput. The channel correlation provides the interference level before equalizing the signal assuming perfect CSI. While the EVM performance considers the interference from the channel and the interference caused by the inaccurate CSI after equalizing the signal.

An experimental evaluation indicating the performance of the three approaches for the adaptive user grouping algorithm in a real-world deployment has been presented. At first, all users were assigned in one group during UL and DL data transmission. By using the "maximizing SE" approach, the system throughput had significantly increased. When the "maximizing number of simultaneous user" approach was used, more users were served using the same radio resources. Furthermore, a total of 24 reliable UL and DL video streams were successfully established by using the "link quality" approach.

CHAPTER 6

CONCLUSIONS AND RECOMMENDATIONS

This thesis has covered the journey of evaluating the practicality of using Ma-MIMO in real-world scenarios, identifying solutions to the operational deployments uncovered, designing, testing and optimising novel algorithms and methodologies. This research thus has contributed to the application of Ma-MIMO to both enhance spectrum efficiency for sub-6GHz carriers and enabling more reliable data connectivity using this technology. In Chapter 3, the University of Bristol Ma-MIMO testbed is introduced and real-time results from several experimental and measurement campaigns are presented. Improving the world's first real-time 128-antenna Ma-MIMO testbed was made based on the results from these experimental and measurement campaigns. Here, channel hardening was investigated in several environments and a simple UL closed loop PC was introduced as developed by the author. Further, OTA synchronisation between user clients was enhanced by using a single antenna to broadcast the PSS in Ma-MIMO instead of using all antennas with a random static pattern. Chapter 4 then evaluated the impact of spatially multiplexing an increasing number of users within a single-cell Ma-MIMO system. The trial and deployment of Ma-MIMO offering a record breaking spectrum efficiency of 145.6 bits/s/Hz was presented and the limiting factors when attempting to increase spectrum efficiency value in that trial were illustrated. It was shown and illustrated that for realistic performance the sum spectrum efficiency should be calculated based on the EVM performance instead of using Shannon capacity calculations. Lastly, Chapter 5 introduced a novel user grouping algorithms for a single cell Ma-MIMO to further enhance the Ma-MIMO advantages for different applications. For the first time, the methodology addresses the interference caused by correlation in the user as well as hardware impairments. Specifically, the author has uniquely achieved by extracting the EVM, and three different methodologies are applied to address specific wireless connectivity quality of service objectives. The user grouping algorithms were validated

experimentally with real-time results in the world's first urban 5G showcase in Bristol (March 2018).

Derived from the real-time evaluation and the findings through this thesis, the following are the recommendations to researchers and engineers who are addressing Ma-MIMO deployment and further advancing the use of this technology to fully exploit the spatial domain.

- **Recommendation 1:** *Exploiting the channel hardening in Ma-MIMO for designing power control algorithms*

  The channel hardening phenomenon in Ma-MIMO was demonstrated in chapter 3. It was shown in section 3.2.6.2 that fewer power control adjustments are needed when the number of antennas at the BS is increased. This decreases the required overheads from the BS used in open loop power control and the feedback from users used in closed loop power control. The highly improved channel is recommended to be exploited to lower the complexity of the power control algorithms in Ma-MIMO. This recommendation can be compared with the reduction in power control update rates in wide band code-division multiple access (WCDMA) when compared to narrow band CDMA. .

- **Recommendation 2:** *With a practical number of antennas and linear equalizers at the BS, ZF or MMSE should be used in Ma-MIMO*

  It was shown in chapter 4 that MF has low sensitivity to inaccurate CSI, but the interference level between users due to the spatial correlation is very high with practical number of antennas at the BS. So the idea of using MF is not applicable in real-world deployment. As shown in section 4.3, ZF and MMSE suppress the interference caused by the channels between users, but they have high sensitivity to the CSI accuracy. However, the overall interference in ZF and MMSE is significantly lower than that of MF. Considering that and the real-time obtained results from several trials in chapter 3 and chapter 4, ZF and MMSE are recommended to be used in real-world Ma-MIMO deployments.

- **Recommendation 4:** *Use a single antenna to enhance coverage of OTA sync signal*

  The PSS is repeatedly transmitted in the first OFDM symbol of the physical layer frame each 10 ms. It was shown in chapter 4 that by transmitting the PSS using a random static pattern from all antennas, the phase of the sync signal is generated randomly from each antenna at the BS creating nulls in different locations since the sync signal is not precoded. This has caused sync losses for the users based on their locations and the sync signal phases from the antennas at the BS. To overcome this problem, it is recommended to transmit the PSS signal from a single antenna as shown in section 3.3 and Appendix D. The power level during the sync OFDM symbol duration should be increased to compensate the loss of the antenna array gain, caused by using a single antenna. Sector antennas can be used for

transmitting the PSS signal, but they should be pointed at different locations as shown in Appendix D.

- **Recommendation 5:** *EVM performance should be used to evaluate algorithms and techniques in Ma-MIMO simulators*

  It was shown in chapter 4 that the maximum SE based on Shannon capacity calculations was achieved by increasing the number of simultaneous users. The current technology can't reach this theoretical results. For realistic performance, the EVM performance method proposed in section 4.5.3 is recommended to be used. Unlike Shannon capacity calculations, it was shown in section 4.5.3 and experimentally validated in section 4.7 that the maximum sum SE could be achieved by decreasing the number of simultaneous users.

- **Recommendation 6:** *Optimisation of the number of antennas at the BS in Ma-MIMO mainly relies on the equalizer, hardware quality, reciprocity calibration technique and the propagation environment*

  One of the common questions about Ma-MIMO technology is "how many antennas are needed at the BS?". It was shown in chapter 4 that several factors impact the performance of Ma-MIMO. The first main factor is the channel propagation between the BS and the users. User-side Gramian matrices for a LOS indoor environment and a LOS outdoor environment can be seen in section 3.2.3.2 and 5.5.3. Although the distance between users' antennas in the indoor environment is smaller than the outdoor environment, the spatial correlation between users in the indoor environment is lower than the outdoor environment due to the rich scattering environment. The second main factor is the equalizer used in the Ma-MIMO system. It was shown in chapter 4 that ZF and MMSE equalizers outperform MF with practical number of antennas at the BS. However, the performance might be improved if non-linear equalizers are used to mitigate the interference between users. Therefore, lower number of antennas might be needed to establish the same performance. The third main factor is the hardware quality. It was shown in section 4.6 that the CSI accuracy from high hardware quality with low number of antennas could be better than reducing the hardware quality and increasing the number of antennas. The fourth main factor is the reciprocity calibration technique. This only impacts the DL performance as shown in section 4.4. By increasing number of antennas, the impact of the calibration error is reduced. However, lower number of antennas can be used to achieve the same performance by decreasing the calibration error.

  Ma-MIMO simulators based on the four aforementioned factors can be used to decide number of antennas at the BS in order to achieve the required performance.

- **Recommendation 7:** *Estimating the SINR value based on the EVM performance*

The CSI accuracy highly impacts the performance in Ma-MIMO as shown in chapter 4. Many algorithms rely on the SINR value as an indicator of the system's performance. In the theoretical work, the interference caused by inaccurate CSI can be covered in the SINR calculations. However, this can't be done in a real-system as shown in section 5.1.1. In section 5.1, a practical SINR estimation method with high accuracy was presented based on the EVM performance. This method is recommended to cover all the interference sources.

- **Recommendation 8:** *A novel EVM prediction method for a single-cell Ma-MIMO*

  As shown in section 5.1, the EVM performance covers all the interference sources. However, the EVM value can be obtained after receiving the signals and multiplying them with the equalizer complex coefficients in UL scenario. So if a group of 24 users are transmitting data, the EVM values can be obtained for these 24 users. If the EVM values are needed to be calculated for a subset users taken from this group, only the subset users have to transmit signals in order to calculate the EVM values. So relying on the EVM performance would increase the complexity and the delay of any scheduling algorithm. However the novel EVM prediction method introduced in section 5.1.2 overcomes this problem. This method is recommended in a single cell Ma-MIMO with ZF and MMSE to predict the EVM value with high accuracy for a subset of users taken from the original set of simultaneous users without the need of re-transmit signals.

- **Recommendation 9:** *The need for user grouping algorithm to mitigate the impact of inter-user interference in a single-cell Ma-MIMO*

  The impact of multiplexing more simultaneous users in Ma-MIMO was illustrated in chapter 4. The spatial correlation between users and the CSI accuracy play major role in increasing number of simultaneous users. The need for user grouping algorithms was illustrated in section 5.2. To improve the performance of Ma-MIMO, the spatial correlation between user and the interference caused by inaccurate CSI should be considered when user grouping algorithm is designed.

- **Recommendation 10:** *Novel adaptive user grouping algorithms for a single-cell Ma-MIMO to further enhance the SE gain and the link reliability*

  In chapter 5, novel adaptive user grouping algorithms for a single-cell Ma-MIMO were introduced. For the first time, the methodology addresses the interference caused by the user channel vectors as well as hardware impairments. Here, this is uniquely achieved by extracting the EVM, and three different methodologies are applied to address specific wireless connectivity objectives. The first, maximizes the spectral efficiency which is more desirable for cellular networks as shown in section 5.3.1. The second, maximizes the number of users for low data rate bearers, which is suitable for the IoT as shown in section 5.3.2.

Whilst, the third approach focuses on specific quality per user, for applications such as wireless cameras at major cultural or sporting events as shown in section 5.3.3.

The aforementioned user grouping algorithms have improved the Ma-MIMO performance as shown from simulations and real-time evaluations in section 5.4.2 and section 5.5, respectively. Therefore, these algorithms are recommended to be used in Ma-MIMO to further enhance the SE gain and the link reliability.

The future work should consider the above recommendations. Considering a multi-cell scenario and exploring the required update rate for channel estimation, TPC commands, EVM prediction and user grouping are important and interesting areas. In addition to the work covered in this thesis, the following suggestions are recommended as future work for its possibility to improve the Ma-MIMO performance:

- *Real-time Evaluation for Distributed Ma-MIMO*

  The improved channel robustness in Ma-MIMO has enabled this technology to be a key element in 5G deployment. With practical number of antennas at the BS, the spatial correlation between users in a LOS outdoor environment is large compared to the indoor environment. This would effect the system's performance and the ability to serve larger number of simultaneous users. A theoretical promising solution is to allocate the BS antennas in different places to decrease the spatial correlation between users and mitigate shadowing (blockages), which is known as distributed Ma-MIMO [131]. However, real-time evaluation is required for this method. Several challenges should be handled and tested in field trials such as OTA synchronisation and reciprocity calibration. Besides, a comparison between Ma-MIMO and distributed Ma-MIMO is required since the second approach comes with high deployment cost so that a little performance improvement won't be enough to adopt this method.

- *Detecting Jamming Users: Based on the SINR and the EVM Performances*

  The user who is jamming the network by intentionally introducing inaccurate CSI could be detected based on the SINR and EVM performance. The difference between the EVM performance and the channel correlation between users could be exploited to detect the jamming user . The relations between the SINR value and the EVM performance introduced in chapter 5 can be used as an indicator. An interesting area is to find the maximum acceptable threshold for the difference between the EVM value and the estimated SINR (based on perfect CSI) before removing the user from the system.

- *An External Agent for Managing Radio Resources in sub-6 GHz wireless systems*

  It was shown in chapter 5 that user grouping improves the Ma-MIMO performance. However, this improvement might not be enough to meet the 5G requirements in a crowded area.

By serving large number of users, different time slots or frequencies are used to allocate users into different groups. With high spatial correlation between users, larger number of groups might be needed. This could led to a compromise between increasing the latency or decreasing the data rate. Since the 5G technology will keep relying on the existing wireless technology such as LTE, it could be useful to manage the radio resources between all of them. An external agent between the different wireless access point could enhance the wireless performance. For example, if some users have a very high spatial correlation in Ma-MIMO, some of them could be re-assigned to an LTE access point. This is a very interesting area for future work which is highly recommended to meet the 5G requirements in a major cultural or sporting events and an area within the EPSRC TOUCAN Programme Grant.

APPENDIX A

MASSIVE MIMO TESTBED'S SPECIFICATIONS

The University of Bristol massive MIMO testbed was designed and implemented based on the commercial off-the-shelf equipments from National Instruments. Table A.1 shows the main hardware components used to build the Ma-MIMO testbed.

Table A.1: Hardware components for the University of Bristol massive MIMO testbed

Component	**Model**	**Features**
Host	PXIe8135	2.3 GHz Quad-Core PXI Express Controller Up to 8 GB/s system and 4 GB/s slot bandwidth
SDR	USRP RIO 2943R / 2953R	2 RF Front Ends and 1 Xilinx Kintex-7 FPGA Centre frequency variable from 1.2–6 GHz 830 MB/s bidirectional throughput on up to 15 DMA channels
Co-Processor	FlexRIO 7976R	1 Xilinx Kintex-7 410T FPGA 2.4 GB/s bidirectional throughput on up to 32 DMA channels
Switch	PXIe-1085	Industrial form factor 18-slot chassis 7 GB/s bidirectional throughput per slot 2 switches per chassis with inter-switch traffic up to 3.2 GB/s Links between chassis bound to 7 GB/s bidirectional
Expansion Module	PXIe-8374	PXI Express (x4) Chassis Expansion Module Software-transparent link without programming Star, tree or daisy-chain configuration
Reference Clock Source	PXIe-6674T	10 MHz reference clock source with < 5 ppb accuracy 6 configurable I/O connections
Ref. Clock Distribution	OctoClock	10 MHz 8-channel clock and timing distribution network

APPENDIX B

NUMBER OF ANTENNAS AT THE BS AND CSI ACCURACY FOR MAXIMISING SE

The work in this section extends the results in section 4.6 for maximizing the SE based on the practical evaluation method introduced in section 4.5.3. It also covers the impact of reciprocity calibration error in DL data transmission introduced in section 4.4. The system model in section 4.2 is adopted for this work. ZF and MMSE decoders/precoders were used in the Ma-MIMO simulator mentioned earlier with rate 3/4 LDPC code as described in [121]. For the DL data transmission, $\sigma^2_{e_{ul}} = 1\%$ was used for the error variance in the UL channel estimation between the UE and the BS. IID Rayleigh channels are used for the results in Figure B.1 Figure B.2, Figure B.3 and Figure B.4. The results in Figure B.1 show the maximum sum SE when the total available number of users is 22. The correspondent number of bits used in the MCS order for maximizing the sum SE can be seen in Figure B.2. When $\sigma^2_{e_{dl}} = 0\%$, the maximum sum SE for UL and DL scenarios are the same. For UL and DL scenarios, maximizing the sum SE was less sensitive to inaccurate CSI when the number of antennas at the BS was increased from 64 to 128. The results in Figure B.3 show the maximum sum SE when the total number of users is 40. The correspondent number of bits used in the MCS order for maximizing the sum SE can be seen in Figure B.4. With perfect CSI and $M = 128$, the maximum sum SE was increased by 80 bits/s/Hz and 40 bits/s/Hz for UL and DL scenarios respectively. This is achieved by serving all the 40 users with 256-QAM in UL and 64-QAM in DL. When the $\sigma^2_{e_{ul}} \in [0.2\%, 0.4\%]$, the maximum sum SE is achieved by serving all the 40 UEs with 64-QAM. By comparing between the 22 available users scenario and the 40 available users scenario, it can be seen that the maximum sum SE is achieved when more users are available. That's because the BS has more options to select users with lower spatial correlation. Besides, using lower MCS order with larger number of users could achieve higher sum SE than using higher MCS order with lower number of users.

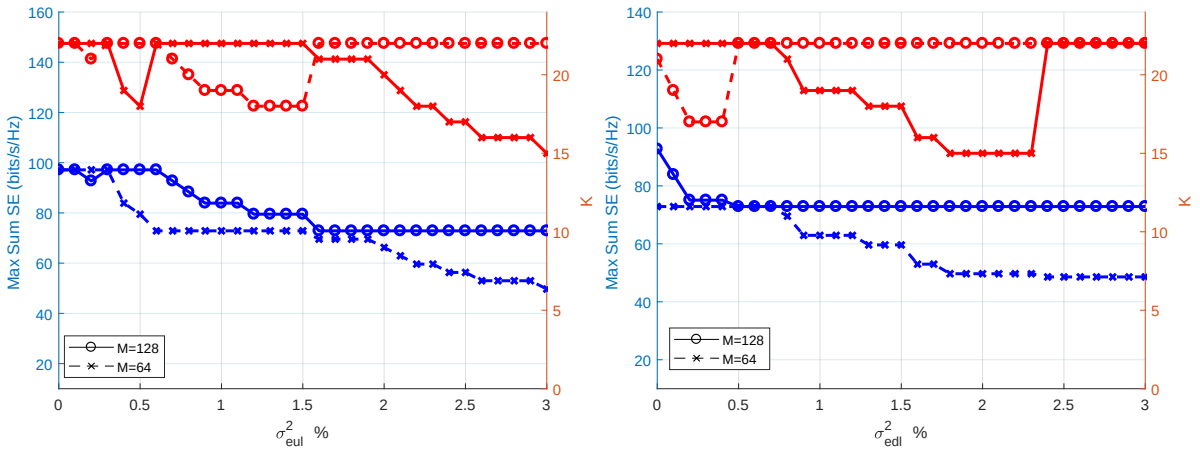

Figure B.1: Maximizing sum SE for 22 users with ZF and MMSE using IID Rayleigh Channels. UL scenario on the left and DL scenario on the right.

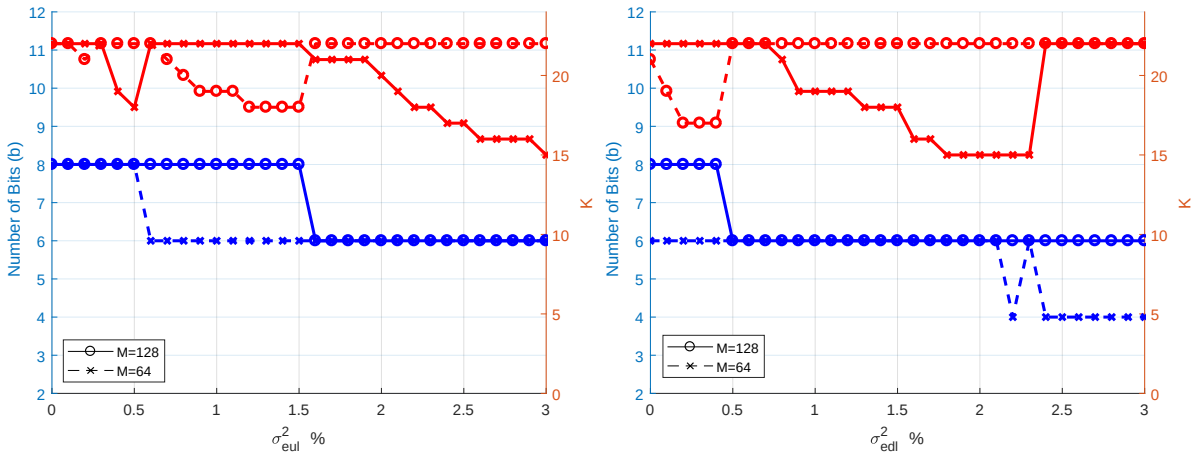

Figure B.2: The correspondent number of bits used in the MCS order to maximize sum SE for 22 users with ZF and MMSE using IID Rayleigh Channels. UL scenario on the left and DL scenario on the right.

The LOS indoor channels captured from the trail in section 4.1 are used for the results in Figure B.5 and Figure B.6. The maximum sum SE when the total available number of users is 22 can be seen in Figure B.5. The correspondent number of bits used in the MCS order for maximizing the sum SE can be seen in Figure B.6. Compared to the results from the IID channels, the maximum sum SE was decreased due to the higher spatial correlation between users.

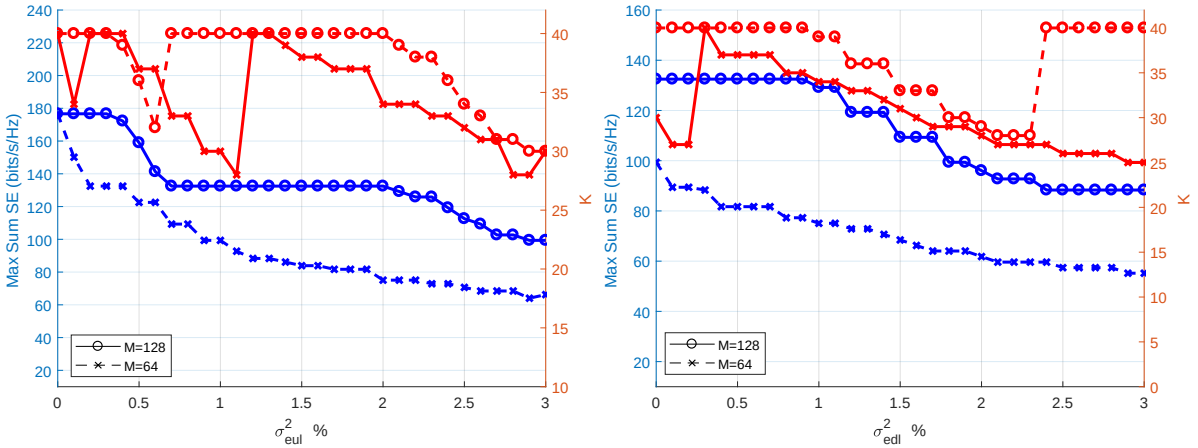

Figure B.3: Maximizing sum SE for 40 users with ZF and MMSE using IID Rayleigh Channels. UL scenario on the left and DL scenario on the right.

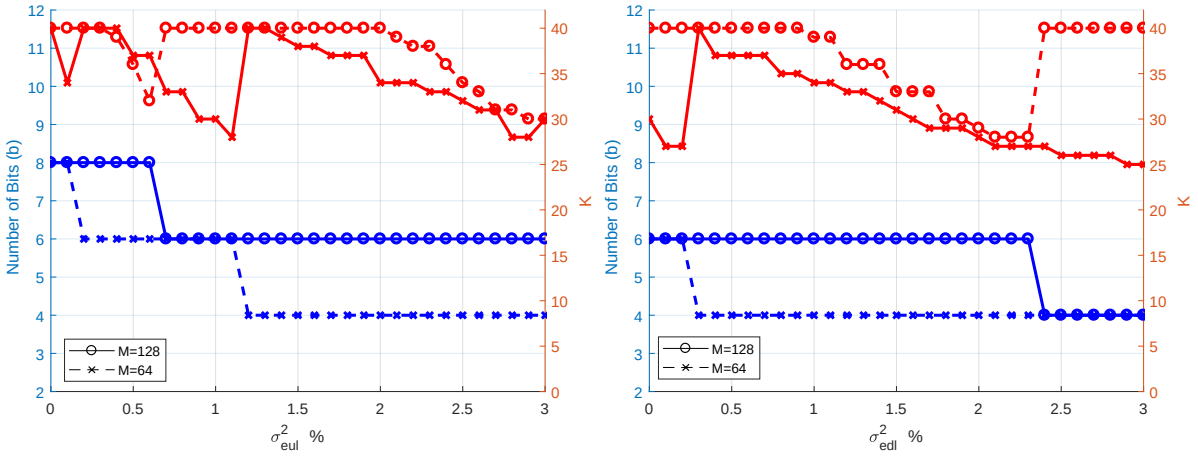

Figure B.4: The correspondent number of bits used in the MCS order to maximize sum SE for 22 users with ZF and MMSE using IID Rayleigh Channels. UL scenario on the left and DL scenario on the right.

The LOS outdoor channels captured from the trail in section 3.2.6.2 are used for the results in Figure B.7 and Figure B.8. The maximum sum SE when the total available number of users is 8 can be seen in Figure B.7. The correspondent number of bits used in the MCS order for maximizing the sum SE can be seen in Figure B.8. Compared to the results from the IID channels and the indoor channels, lower MCS order is used when number of selected user to maximise the sum SE is 8 or less. This is caused by the high spatial correlation between users due to the low scattering environment.

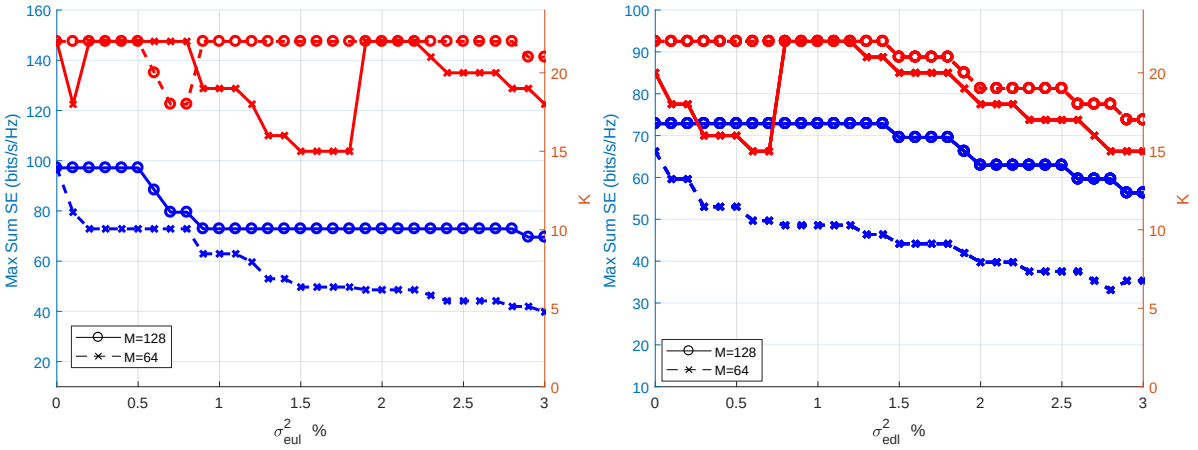

Figure B.5: Maximizing sum SE for 22 users with ZF and MMSE using LOS measured indoor channel. UL scenario on the left and DL scenario on the right.

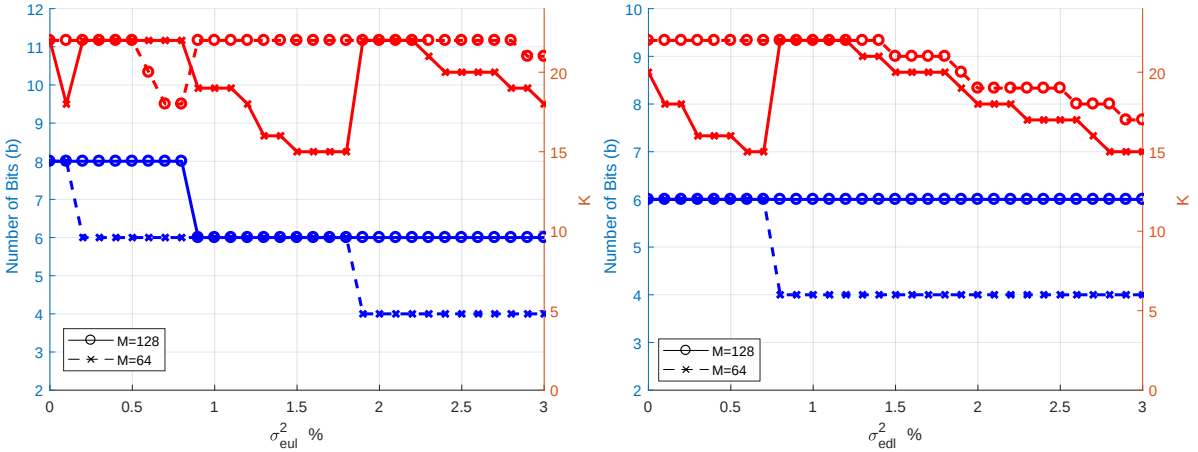

Figure B.6: The correspondent number of bits used in the MCS order to maximize sum SE for 22 users with ZF and MMSE using LOS indoor channel. UL scenario on the left and DL scenario on the right.

The hardware quality and the reciprocity calibration technique impact the accuracy of the CSI in Ma-MIMO. Deciding the required number of antennas at the BS in Ma-MIMO is effected by the hardware quality, the reciprocity calibration technique and the propagation environment.

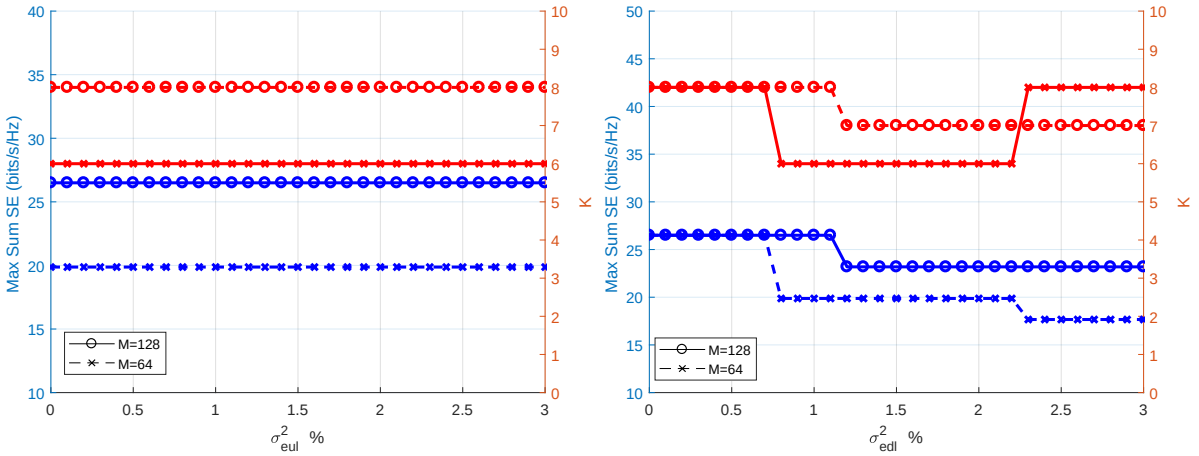

Figure B.7: Maximizing sum SE for 8 users with ZF and MMSE using LOS measured outdoor channel. UL scenario on the left and DL scenario on the right.

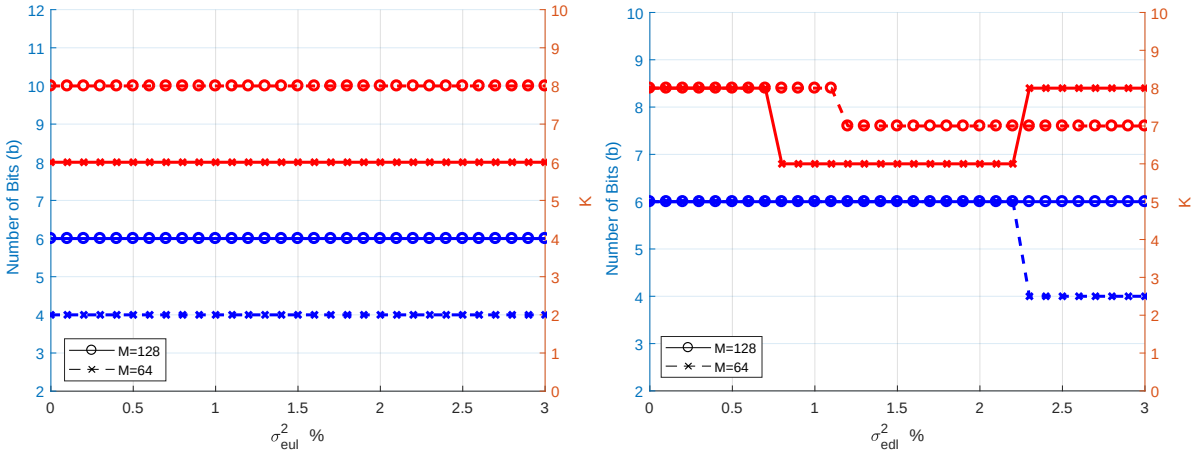

Figure B.8: The correspondent number of bits used in the MCS order to maximize sum SE for 8 users with ZF and MMSE using the LOS outdoor channel. UL scenario on the left and DL scenario on the right.

APPENDIX C

EXPERIMENTAL CAMPAIGN WITH BRITISH TELECOM

Massive MIMO was considered a key candidate for 5G technology the measurement campaign in this section was conducted. Although Ma-MIMO was covered in many theoretical researches, mobile operators wanted to understand the realistic benefits, challenges and requirements for the Ma-MIMO technology. Therefore, a collaboration measurement campaign was conducted by a researchers and engineers from BT, University of Bristol, Lund University and NI [40]. In addition to exploring the potential of Ma-MIMO technology in real-time, it was an opportunity to validate some off-line analysis based on data collected from previous measurement campaigns. The measurement campaign took a place at BT's R&D headquarters in Adastral Park, Ipswich [25][1]. An indoor and outdoor environments were covered as shown in in Figure C.1 and in Figure C.2. The University of Bristol Ma-MIMO testbed operated at a 3.51 GHz carrier frequency sharing a common 20MHz radio channel. The patch panel antenna array was setup in a 4x32 configuration with vertical polarisations for all 128 antennas.

For the outdoor environment, real mobile phone handset was evaluated in pedestrian use. It was also placed inside a car for higher mobility evaluations. Off-line comparisons and analysis were made based on the data captured from these experiments. For the indoor environment, two scenarios were considered in a large exhibition hall . In the first scenario, 12 user clients were placed on the opposite side of the BS as shown in Figure C.1. Twelve video steams were spatially multiplexed in real-time. In the second scenario, 24 users were divided into two groups, where each group had 12 users. The users where placed on the left and right sides of the large exhibition hall as shown in Figure C.3 and Figure C.4. The PSS signal was broadcasted from all the antennas at the BS and the sync signal was lost several times due to the reason described in section 3.3. Therefore, IUI was increased between users due to the ICI, ISI and interference

[1] A video of the measurement campaign at BT's R&D headquarters is available at https://bit.ly/2DMZQaV

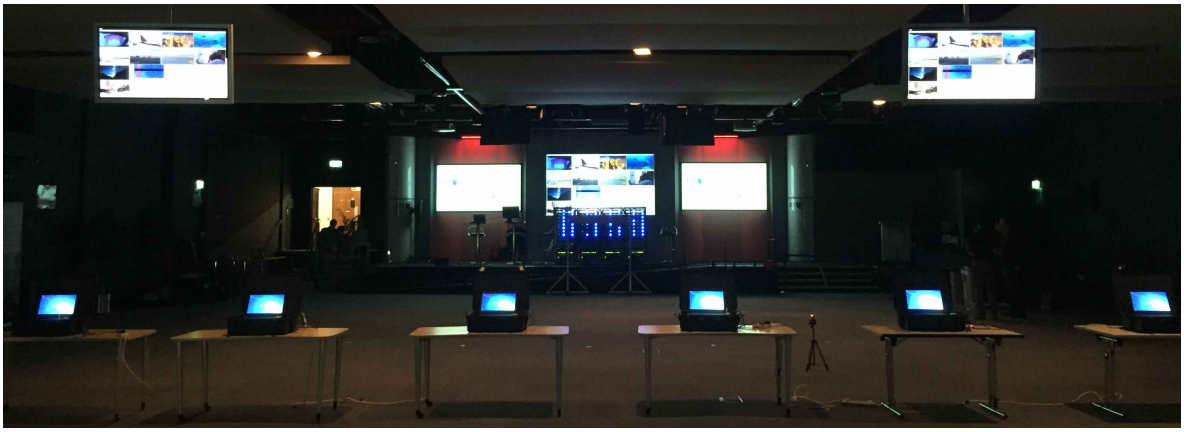

Figure C.1: Twelve real-time video steams in an indoor environment

Figure C.2: Outdoor evaluation. Left, UE side. Right, BS side.

between data streams cased by inaccurate CSI. Figure C.5 shows the 64-QAM constellations for 24 user captured from this trial. While Figure C.6 and Figure C.7 show the 64-QAM constellations after removing two users randomly. The observed EVM was enhanced by spatially multiplexing less number of users. Based on the results from this experimental campaign, it was recommended to improve the synchronisation method between the users and to increase the accuracy of channel estimation in Ma-MIMO systems.

Despite these challenges, 24 users were spatially multiplexed with 64-QAM for each user. This work had led Bristol, Lund and BT teams to receive the 2017 Collaborate to Innovate (C2I) Award for their submission 'Setting World Records in 5G Wireless Spectral Efficiency using Ma-MIMO' under the 'Information, Data & Connectivity' category [132].

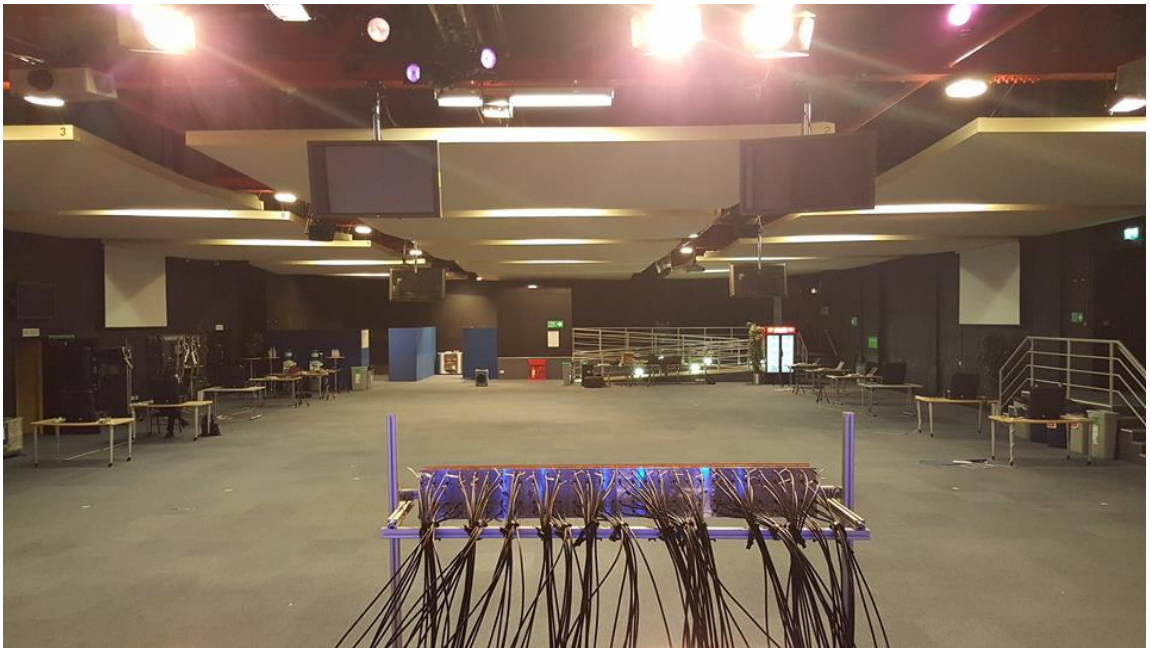

Figure C.3: BS view of the indoor evaluation with 24 users.

Figure C.4: User side view of the indoor evaluation with 24 users.

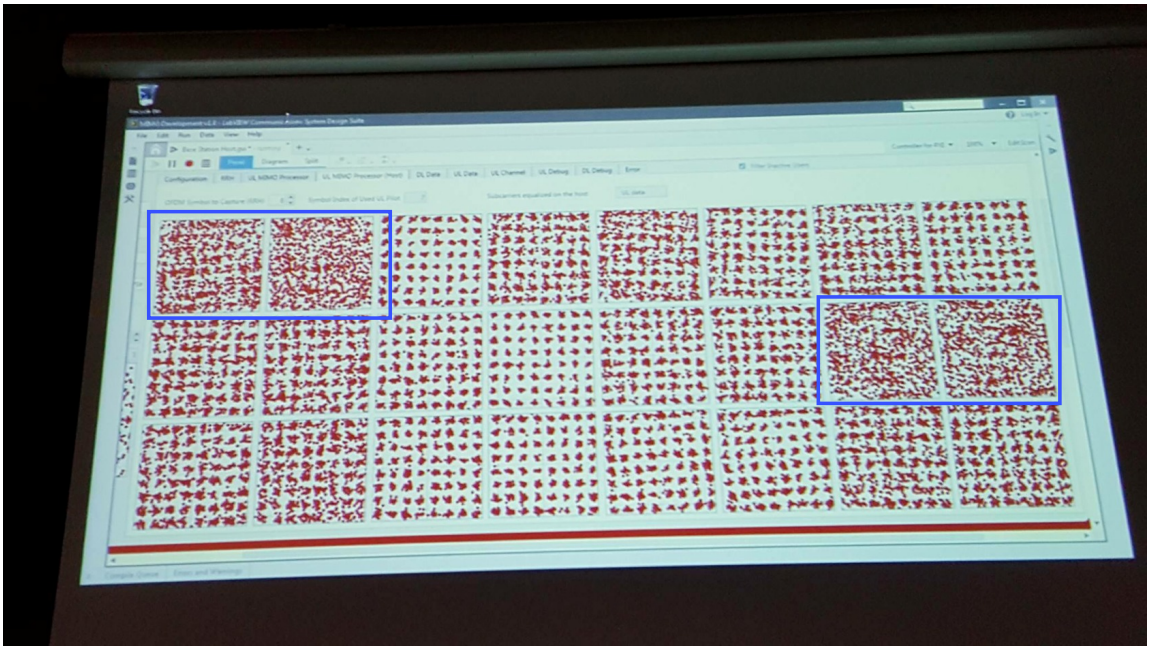

Figure C.5: 64-QAM UL constellations from 24 UEs. High EVM values can be observed from the constellations in the blue collared rectangular compared to the one in Figure C.6 and Figure C.7.

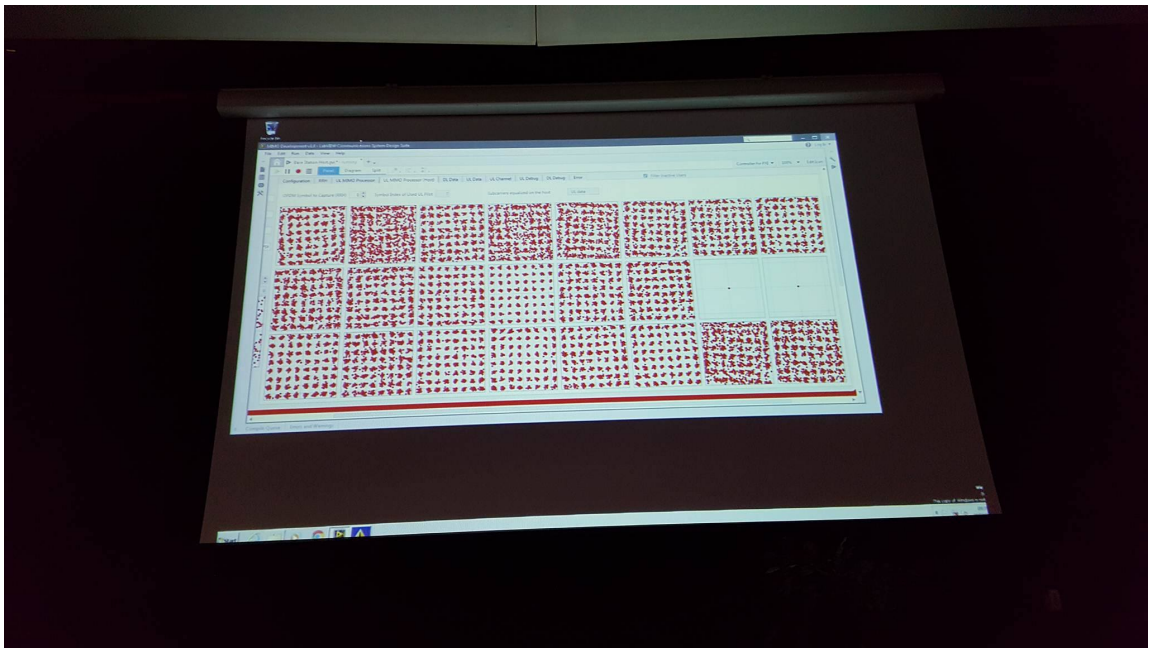

Figure C.6: 64-QAM UL constellations from 22 (After removing two user randomly)).

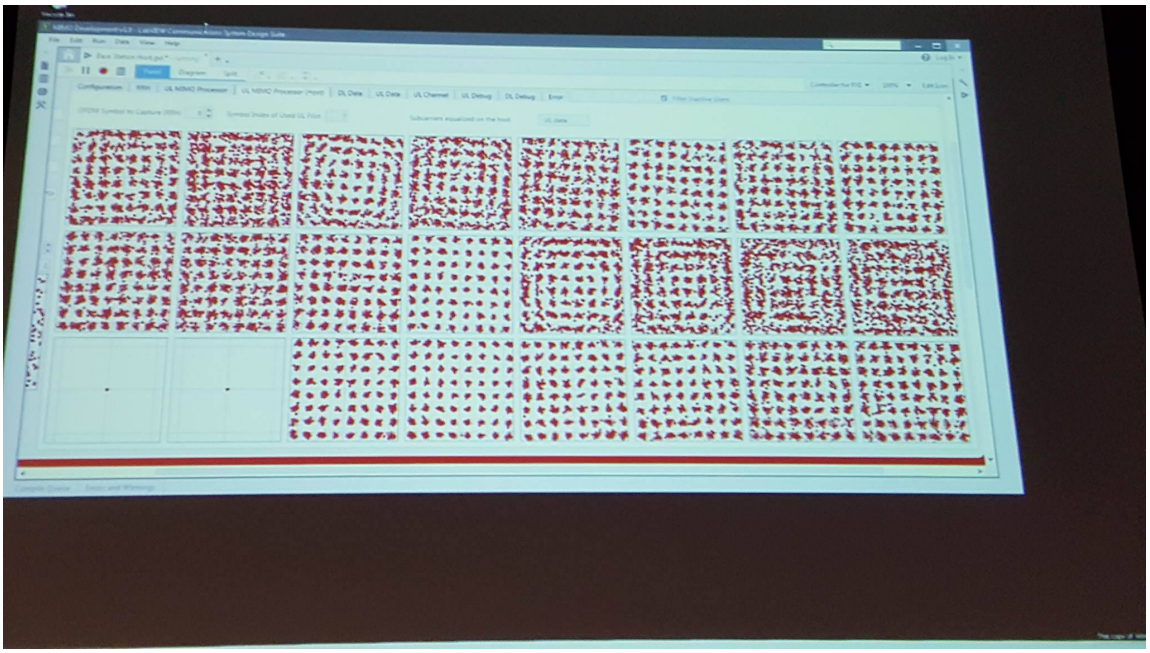

Figure C.7: 64-QAM UL constellations from 22 (After removing two user randomly)).

APPENDIX D

OUTDOOR EXPERIMENTAL CAMPAIGN FOR REAL-TIME EVALUATION

An outdoor experimental campaign was conducted to evaluate the improved OTA synchronisation method described in section 3.1.5 and exploring the possibility of serving all the 12 users in real-time HD video streams. This experimental campaign was a preparation for the first urban 5G showcase described in section 5.5. Bristol's Millennium Square was used with a patch panel antenna array to serve 8 user clients placed on the opposite side of the BS and 2 user clients on the balcony of We The Curious building. The Ma-MIMO system operated at a 3.51 GHz carrier frequency sharing a common 20MHz radio channel. The array was setup in a 32×4 configuration with vertical polarisations for all 128 antennas. Two sector antennas were used to transmit the synchronization signal. The first sector antenna is pointed toward the 8 user clients allocated at the opposite side of the BS while the second sector antenna is pointed toward the 2 user clients on the balcony as it is shown in Figure D.1. The sector antennas has increased the synchronization power level and improved the synchronization performance. In the experimental campaigns, the frame schedule was configured to use one UL pilot, two UL data and one guard followed by DL pilot, one DL data and one guard for each half subframe except the first half OFDM subframe which is used for OTA synchronization.

When the PSS was broadcasted from the two sector antennas, there was no sync loss. But when the PSS was broadcasted from all the 128 antennas, the average sync loss was 11 per second. Although the problem of OTA synchronisation described in section 3.3 was solved, the system was not able to spatially multiplex 12 reliable video streams on UL or DL. The Ma-MIMO system was only able to spatially multiplex six reliable video streams in UL data transmission and three reliable video streams in DL data transmission. This was achieved by using QPSK. Number of users was decreased gradually until a reliable video streams were achieved. These

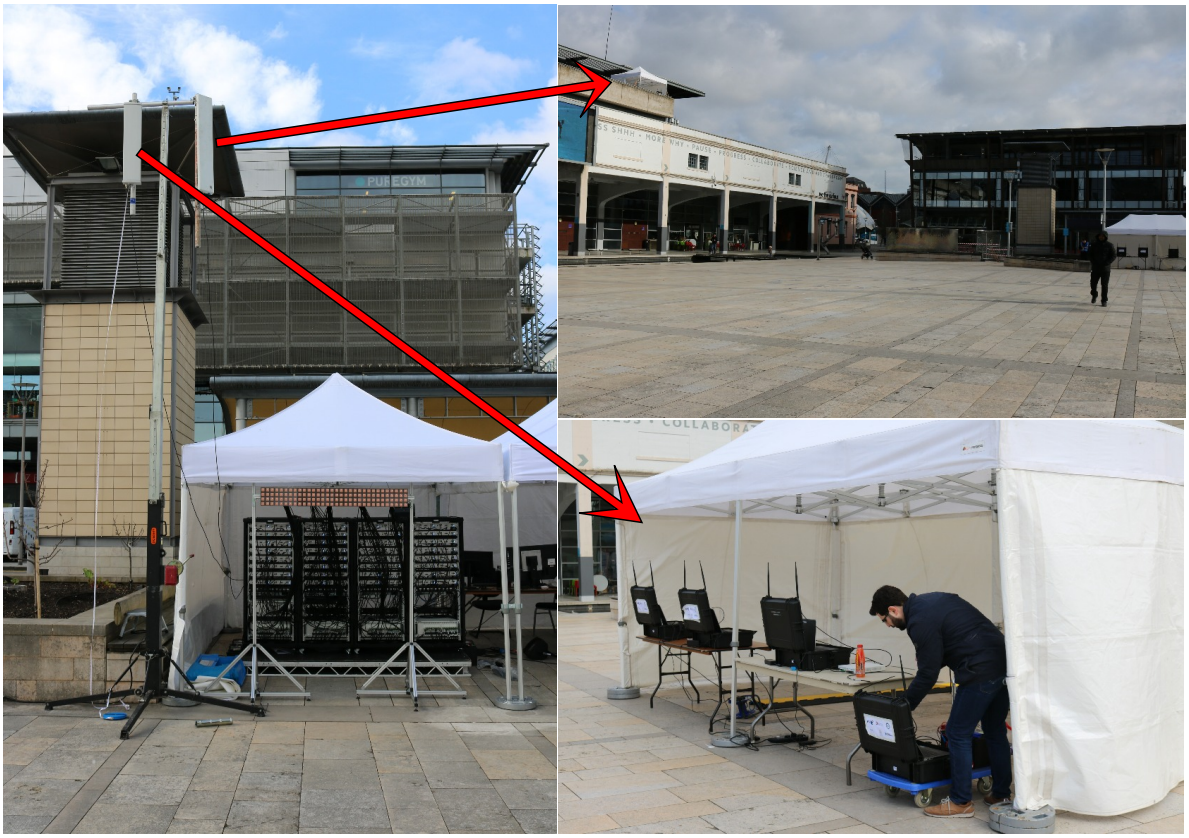

Figure D.1: Measurement Environment in Millennium Square with two sector antennas for OTA Synchronization

results have encouraged to implement the user grouping algorithm, proposed in section 5.3, in the Ma-MIMO testbed.

References

[1] "Could drones replace fireworks in the UK?." https://www.bbc.co.uk/news/uk-43195059, 2018.

[2] W. Sun, E. G. Ström, F. Brännström, Y. Sui, and K. C. Sou, "D2D-based V2V communications with latency and reliability constraints," in *2014 IEEE Globecom Workshops (GC Wkshps)*, pp. 1414–1419, Dec 2014.

[3] N. Nikaein and S. Krea, "Latency for Real-Time Machine-to-Machine Communication in LTE-Based System Architecture," in *17th European Wireless 2011 - Sustainable Wireless Technologies*, pp. 1–6, April 2011.

[4] S. Singh and N. Singh, "Internet of Things (IoT): Security challenges, business opportunities amp; reference architecture for E-commerce," in *2015 International Conference on Green Computing and Internet of Things (ICGCIoT)*, pp. 1577–1581, Oct 2015.

[5] H. Liang and W. Zhuang, "Efficient On-Demand Data Service Delivery to High-Speed Trains in Cellular/Infostation Integrated Networks," *IEEE Journal on Selected Areas in Communications*, vol. 30, pp. 780–791, May 2012.

[6] M. L. J. Vora, "EVOLUTION OF MOBILE GENERATION TECHNOLOGY: 1G TO 5G AND REVIEW OF UPCOMING WIRELESS TECHNOLOGY 5G," in *International Journal & Magazine of Engineering, Technology, Management and Research*, October 2015.

[7] 5GPP, "5G Vision: The 5G Infrastructure Public Private Partnership: the next generation of communication networks and services.." https://5g-ppp.eu/wp-content/uploads/2015/02/5G-Vision-Brochure-v1.pdf, 2015.

[8] ITU, "Working Party 5D - DRAFT NEW REPORT ITU-R M.[IMT-2020.TECH PERF REQ] - Minimum requirements related to technical performance for IMT-2020 radio interface(s)." https://5g-ppp.eu/wp-content/uploads/2015/02/5G-Vision-Brochure-v1.pdf, 2017.

[9] 3GPP, "3GPP TR 38.913 V14.3.0: Study on Scenarios and Requirements for Next Generation Access Technologies," 2017.

[10] FCC, “Completed Auctions Summary.” http://wireless.fcc.gov/auctions, 2017.

[11] ETSI, *Evolved Universal Terrestrial Radio Access (E-UTRA); Base Station (BS) radio transmission and reception (3GPP TS 36.104 version 13.5.0 Release 13)*, October 2016.

[12] 3GPP, “Technical Specification (TS) 25.101.” https://portal.3gpp.org/desktopmodules/Specifications/SpecificationDetails.aspx?specificationId=1151, 1999.
User Equipment (UE) radio transmission and reception (FDD).

[13] 3GPP, “Technical Specification (TS) 45.005.” https://portal.3gpp.org/desktopmodules/Specifications/SpecificationDetails.aspx?specificationId=2709, 2016.
GSM/EDGE Radio transmission and reception.

[14] IMDA, “Technical Specification - Short Range Devices,” October 2016.

[15] L. Wei, R. Q. Hu, Y. Qian, and G. Wu, “Key elements to enable millimeter wave communications for 5G wireless systems,” *IEEE Wireless Communications*, vol. 21, pp. 136–143, December 2014.

[16] L. X. S. L. ZHAO Jianping, LI Chenlei, “Technical challenges for high-frequency wireless communicationl,” in *Journal of Communications and Information Networks*, Aug 2016.

[17] Qualcomm, “5G mmWave: the next frontier in mobile broadband,” June 2016.
https://www.qualcomm.com/invention/technologies/5g-nr/mmwave.

[18] 3GPP, “3GPP TR 38.802 V14.1.0: Technical Specification Group Radio Access Network; Study on New Radio Access Technology - Physical Layer Aspects,” 2017.

[19] N. Instruments, “mmWave: The Battle of the Bands,” June 2016.
http://www.ni.com/white-paper/53096/en/.

[20] Arqiva, “Arqiva and Samsung Kick off UK’s First 5G Fixed Wireless Access Trial.” https://www.arqiva.com/news/press-releases/arqiva-and-samsung-kick-off-uks-first-5g-fixed-wireless-access-trial/, 2017.

[21] “Deutsche Telekom and Huawei Complete World’s First 5G High mmWave Technology over-the-air Field Tests.” https://www.huawei.com/en/press-events/news/2018/2/DectschTelckom-5G-High-mmWave-Technology, 2018.

[22] Marzetta and T. L., “Noncooperative Cellular Wireless with Unlimited Numbers of Base Station Antennas,” *IEEE Transactions on Wireless Communications*, vol. 9, pp. 3590–3600, nov 2010.

[23] A. L. Swindlehurst, E. Ayanoglu, P. Heydari, and F. Capolino, "Millimeter-wave massive MIMO: the next wireless revolution?," *IEEE Communications Magazine*, vol. 52, pp. 56–62, Sep. 2014.

[24] "What is LTE Advanced?." https://www.androidauthority.com/lte-advanced-176714/, 2018.

[25] T. Engineer, "UK trials of massive MIMO bring 5G communications closer to reality." https://www.theengineer.co.uk/uk-trials-of-massive-mimo-bring-5g-communications-closer-to-reality/, 2017.

[26] "Massive MIMO at the University of Bristol." https://www.telecomtv.com/content/5g/massive-mimo-at-the-university-of-bristol-16690/, 2018.

[27] W. B. Hasan, P. Harris, A. Doufexi, and M. Beach, "Real-Time Maximum Spectral Efficiency for Massive MIMO and its Limits," *IEEE Access*, vol. 6, pp. 46122–46133, 2018.

[28] W. B. Hasan, P. Harris, A. Doufexi, and M. Beach, "Impact of User Number on Massive MIMO with a Practical Number of Antennas," in *2018 IEEE 87th Vehicular Technology Conference (VTC Spring)*, pp. 1–5, June 2018.

[29] W. B. Hasan, P. Harris, A. Doufexi, and M. Beach, "Spatial Uplink Power Control for Massive MIMO," in *2017 IEEE 85th Vehicular Technology Conference (VTC Spring)*, pp. 1–6, June 2017.

[30] P. Harris, W. B. Hasan, L. Liu, S. Malkowsky, M. Beach, S. Armour, F. Tufvesson, and O. Edfors, "Achievable Rates and Training Overheads for a Measured LOS Massive MIMO Channel," *IEEE Wireless Communications Letters*, vol. 7, pp. 594–597, Aug 2018.

[31] P. Harris, W. B. Hasan, S. Malkowsky, J. Vieira, S. Zhang, M. Beach, L. Liu, E. Mellios, A. Nix, S. Armour, A. Doufexi, K. Nieman, and N. Kundargi, "Serving 22 Users in Real-Time with a 128-Antenna Massive MIMO Testbed," in *2016 IEEE International Workshop on Signal Processing Systems (SiPS)*, pp. 266–272, Oct 2016.

[32] P. Harris, W. B. Hasan, H. Brice, B. Chitambira, M. Beach, E. Mellios, A. Nix, S. Armour, and A. Doufexi, "An overview of massive MIMO research at the University of Bristol," in *Radio Propagation and Technologies for 5G (2016)*, pp. 1–5, Oct 2016.

[33] P. Harris, S. Malkowsky, J. Vieira, F. Tufvesson, W. B. Hasan, L. Liu, M. Beach, S. Armour, and O. Edfors, "Temporal Analysis of Measured LOS Massive MIMO Channels with Mobility," in *2017 IEEE 85th Vehicular Technology Conference (VTC Spring)*, pp. 1–5, June 2017.

[34] P. Harris, S. Malkowsky, J. Vieira, F. Tufvesson, W. B. Hasan, L. Liu, M. Beach, S. Armour, and O. Edfors, "Performance Characterization of a Real-Time Massive MIMO System Mobile Channelswith LOS ," *IEEE Journal on Selected Areas in Communications*, 2017.

[35] W. B. Hasan, P. Harris, H. Bromell, A. Doufexi, and M. Beach, "Adaptive User Grouping Based on EVM Prediction for Efficient &Robust Massive MIMO in TDD," *IEEE Transactions on Vehicular Technology*, 2018.

[36] W. B. Hasan, P. Harris, A. Doufexi, and M. Beach, "User Grouping for Massive MIMO in TDD." TD(17)03069, February 2017.

[37] W. B. Hasan, P. Harris, A. Doufexi, and M. Beach, "Preliminary Investigation of Uplink Power Control for Massive MIMO." TD(16)01084, June 2016.

[38] P. Harris, S. Malkowsky, J. Vieira, F. Tufvesson, W. B. Hasan, L. Liu, M. Beach, S. Armour, and O. Edfors, "Temporal Analysis of Measured LOS Massive MIMO Channels with Mobility." TD(17)03043, February 2017.

[39] P. Harris, W. B. Hasan, H. Brice, M. Beach, E. Mellios, A. Nix, S. Armour, and A. Doufexi, "Massive MIMO Mobility Measurements in LOS with Power Control." TD(16)02031, Oct 2016.

[40] U. of Bristol, L. University, N. Instruments, and B. Telecom, "Collaborate 2 Innovate: Information, Data & Connectivity Category." The Engineer, September 2017.

[41] P. Harris, S. Malkowsky, J. Vieira, and W. B. Hasan, "Communications Technology Changing the World." IEEE Communications Society, November 2016.
Honorary Certificate of Appreciation.

[42] A. Kaye and D. George, "Transmission of Multiplexed PAM Signals Over Multiple Channel and Diversity Systems," *IEEE Transactions on Communication Technology*, vol. 18, pp. 520–526, October 1970.

[43] G. J. Foschini, "Layered space-time architecture for wireless communication in a fading environment when using multi-element antennas," *Bell Labs Technical Journal*, vol. 1, pp. 41–59, Autumn 1996.

[44] V. K. Jones and G. C. Raleigh, "Channel estimation for wireless OFDM systems," in *IEEE GLOBECOM 1998 (Cat. NO. 98CH36250)*, vol. 2, pp. 980–985 vol.2, Nov 1998.

[45] G. D. Golden, C. J. Foschini, R. A. Valenzuela, and P. W. Wolniansky, "Detection algorithm and initial laboratory results using V-BLAST space-time communication architecture," *Electronics Letters*, vol. 35, pp. 14–16, Jan 1999.

[46] R. Prasad, S. Dixit, R. van Nee, and T. Ojanpera, *Globalization of Mobile and Wireless Communications* .
Springer, 2011.

[47] P. W. Wolniansky, G. J. Foschini, G. D. Golden, and R. A. Valenzuela, "V-BLAST: an architecture for realizing very high data rates over the rich-scattering wireless channel," in *1998 URSI International Symposium on Signals, Systems, and Electronics. Conference Proceedings (Cat. No.98EX167)*, pp. 295–300, Sep 1998.

[48] Y. S. Cho, J. Kim, W. Y. Yang, and C. G. Kang, *MIMO OFDM Wireless Communication with Matlab*.
John Wiley & Sons (Asia) Pte Ltd,, 2010.

[49] J. R. Hampton, *Introduction to MIMO Communications*.
Cambridge: Cambridge University Press, 2013.

[50] D. Astely, E. Dahlman, A. Furuskär, Y. Jading, M. Lindström, and S. Parkvall, "LTE: the evolution of mobile broadband," *IEEE Communications Magazine*, vol. 47, pp. 44–51, April 2009.

[51] M. Baker, "LTE-Advanced Physical Layer," *3GPP TSG RAN WG1, MT-Advanced Evaluation Workshop*, 2009.

[52] intel, "WiMAX and the IEEE 802.16m Air Interface Standard," *WiMAX FORUM*, 2010.

[53] Q. Atherosr, "802.11ac MU-MIMO: Bridging the MIMO Gap in Wi-Fi," 2015.

[54] D. Gesbert, M. Kountouris, R. W. H. Jr., C. b. Chae, and T. Salzer, "Shifting the MIMO Paradigm," *IEEE Signal Processing Magazine*, vol. 24, pp. 36–46, Sept 2007.

[55] G. Americas, *MIMO and Smart Antennas for Mobile Broadband Systems*.
2013.

[56] E. Björnson, E. G. Larsson, and T. L. Marzetta, "Massive MIMO: ten myths and one critical question," *IEEE Communications Magazine*, vol. 54, pp. 114–123, February 2016.

[57] T. L. Narasimhan and A. Chockalingam, "Channel Hardening-Exploiting Message Passing (CHEMP) Receiver in Large-Scale MIMO Systems," *IEEE Journal of Selected Topics in Signal Processing*, vol. 8, pp. 847–860, Oct 2014.

[58] B. S. Chockalingam, A. ; Rajan, *Large MIMO Systems*.
Cambridge: Cambridge University Press, 2014.

[59] E. G. Larsson, O. Edfors, F. Tufvesson, and T. L. Marzetta, "Massive MIMO for next generation wireless systems," *IEEE Communications Magazine*, vol. 52, pp. 186–195, February 2014.

[60] T. E. Bogale and L. B. Le, "Beamforming for multiuser massive MIMO systems: Digital versus hybrid analog-digital," in *2014 IEEE Global Communications Conference*, pp. 4066–4071, Dec 2014.

[61] H. Ji, Y. Kim, J. Lee, E. Onggosanusi, Y. Nam, J. Zhang, B. Lee, and B. Shim, "Overview of Full-Dimension MIMO in LTE-Advanced Pro," *IEEE Communications Magazine*, vol. 55, pp. 176–184, February 2017.

[62] A. Ghosh, "5G New Radio (NR): Physical Layer Overview and Performance ," *IEEE Communications Theory Workshop*, May 2018.

[63] F. Rusek, D. Persson, B. K. Lau, E. G. Larsson, T. L. Marzetta, O. Edfors, and F. Tufvesson, "Scaling Up MIMO: Opportunities and Challenges with Very Large Arrays," *IEEE Signal Processing Magazine*, vol. 30, pp. 40–60, Jan 2013.

[64] N. Jindal and A. Goldsmith, "Dirty-paper coding versus TDMA for MIMO Broadcast channels," *IEEE Transactions on Information Theory*, vol. 51, pp. 1783–1794, May 2005.

[65] K. T. Truong and R. W. Heath, "The viability of distributed antennas for massive MIMO systems," in *2013 Asilomar Conference on Signals, Systems and Computers*, pp. 1318–1323, Nov 2013.

[66] "Large Scale Antenna Systems Made Practical: Advanced Signal Processing for Compact Deployments." https://bit.ly/2CZi3lel, 2018.

[67] C. B. Peel, B. M. Hochwald, and A. L. Swindlehurst, "A vector-perturbation technique for near-capacity multiantenna multiuser communication-part I: channel inversion and regularization," *IEEE Transactions on Communications*, vol. 53, pp. 195–202, Jan 2005.

[68] T. L. Marzetta, E. G. Larsson, H. Yang, and H. Q. Ngo, *Fundamentals of Massive MIMO* . Cambridge University Press, 2016.

[69] S. Malkowsky, J. Vieira, K. Nieman, N. Kundargi, I. Wong, V. ?wall, O. Edfors, F. Tufvesson, and L. Liu, "Implementation of low-latency signal processing and data shuffling for TDD massive MIMO systems," in *2016 IEEE International Workshop on Signal Processing Systems (SiPS)*, pp. 260–265, Oct 2016.

[70] C. Shepard, H. Yu, N. Anand, E. Li, T. Marzetta, R. Yang, and L. Zhong, "Argos: practical many-antenna base stations," in *Proceedings of the 18th annual international conference on Mobile computing and networking - Mobicom '12*, no. i, p. 53, ACM Press, 2012.

[71] J. Vieira, F. Rusek, O. Edfors, S. Malkowsky, L. Liu, and F. Tufvesson, "Reciprocity calibration for massive MIMO: Proposal, modeling and validation," *CoRR*, vol. abs/1606.05156, 2016.

[72] F. Kaltenberger, H. Jiang, M. Guillaud, and R. Knopp, "Relative channel reciprocity calibration in MIMO/TDD systems," in *2010 Future Network Mobile Summit*, pp. 1–10, June 2010.

[73] "Huawei and China Unicom jointly complete world's first FDD Massive MIMO field verification." https://www.huawei.com/en/press-events/news/2017/1/world-first-FDD-Massive-MIMO-field-verification, 2017.

[74] "Huawei deploys world's first commercial FDD Massive MIMO in Philippines." http://www.telecomreviewasia.com/index.php/news/network-news/964-huawei-deploys-world-s-first-commercial-fdd-massive-mimo-in-philippines, 2018.

[75] J. Nam, J.-Y. Ahn, A. Adhikary, and G. Caire, "Joint spatial division and multiplexing: Realizing massive MIMO gains with limited channel state information," *2012 46th Annual Conference on Information Sciences and Systems (CISS)*, vol. 1, pp. 1–6, Mar. 2012.

[76] T. L. Marzetta, E. G. Larsson, H. Yang, and H. Q. Ngo, *Fundamentals of Massive MIMO*. Cambridge University Press, 2016.

[77] L. Lu, G. Y. Li, A. L. Swindlehurst, A. Ashikhmin, and R. Zhang, "An Overview of Massive MIMO: Benefits and Challenges," *IEEE Journal of Selected Topics in Signal Processing*, vol. 8, pp. 742–758, Oct 2014.

[78] E. Björnson, J. Hoydis, and L. Sanguinetti, "Massive MIMO Has Unlimited Capacity," *IEEE Transactions on Wireless Communications*, vol. 17, pp. 574–590, Jan 2018.

[79] "Massive MIMO and Channel Modeling for Millimiterwave." https://www.slideshare.net/cpqd/channel-models-for-massive-mimo, 2014.

[80] H. Q. Ngo and E. G. Larsson, "EVD-based channel estimation in multicell multiuser MIMO systems with very large antenna arrays," in *2012 IEEE International Conference on Acoustics, Speech and Signal Processing (ICASSP)*, pp. 3249–3252, March 2012.

[81] R. R. Mueller, M. Vehkaperae, and L. Cottatellucci, "Blind Pilot Decontamination," in *WSA 2013; 17th International ITG Workshop on Smart Antennas*, pp. 1–6, March 2013.

[82] H. Yin, D. Gesbert, M. Filippou, and Y. Liu, "A Coordinated Approach to Channel Estimation in Large-Scale Multiple-Antenna Systems," *IEEE Journal on Selected Areas in Communications*, vol. 31, pp. 264–273, Feb. 2013.

[83] A. Lozano, R. W. Heath, and J. G. Andrews, "Fundamental Limits of Cooperation," *IEEE Transactions on Information Theory*, vol. 59, pp. 5213–5226, Sept. 2013.

[84] J. G. Andrews, W. Choi, R. W. Heath, and C. From, "Overcoming interference in spatial multiplexing mimo cellular networks," *IEEE Wireless Communications*, vol. 14, no. December, pp. 95–104, 2007.

[85] P. Stenumgaard, D. Persson, E. Larsson, and K. Wiklundh, "An early-warning service for emerging communication problems in security and safety applications," *IEEE Communications Magazine*, vol. 51, pp. 186–192, May 2013.

[86] X. Gao, O. Edfors, F. Rusek, and F. Tufvesson, "Massive MIMO in real propagation environments," *CoRR*, vol. abs/1403.3376, 2014.

[87] X. Gao, F. Tufvesson, O. Edfors, and F. Rusek, "Measured propagation characteristics for very-large MIMO at 2.6 GHz," in *2012 Conference Record of the Forty Sixth Asilomar Conference on Signals, Systems and Computers (ASILOMAR)*, pp. 295–299, IEEE, Nov. 2012.

[88] MEDAV, "Antenna Array Calibration and MIMO Channel Sounding." http://www.medav.de/fileadmin/redaktion/documents/English/competence_antenna_e.pdf, 2008.

[89] D. Gesbert, M. Shafi, D. shan Shiu, P. J. Smith, and A. Naguib, "From theory to practice: an overview of MIMO space-time coded wireless systems," *IEEE Journal on Selected Areas in Communications*, vol. 21, pp. 281–302, Apr 2003.

[90] H. Suzuki, R. Kendall, K. Anderson, A. Grancea, D. Humphrey, J. Pathikulangara, K. Bengston, J. Matthews, and C. Russell, "Highly spectrally efficient Ngara Rural Wireless Broadband Access Demonstrator," in *2012 International Symposium on Communications and Information Technologies, ISCIT 2012*, pp. 914–919, 2012.

[91] M. Brown and M. Turgeon, "TitanMIMO." 2014.

[92] J. Vieira, S. Malkowsky, K. Nieman, Z. Miers, N. Kundargi, L. Liu, I. Wong, V. Öwall, O. Edfors, and F. Tufvesson, "A flexible 100-antenna testbed for Massive MIMO," in *2014 IEEE Globecom Workshops (GC Wkshps)*, pp. 287–293, Dec 2014.

[93] N. Instruments, "R1-162238 - A Dynamic TDD Radio Interface." http://www.3gpp.org/ftp/tsg_ran/WG1_RL1/TSGR1_84b/Docs/, 2016.
3GPP TSG RAN WG1 Meeting #84bis.

[94] 3GPP, *TS 36.104 V12.10.0 Release 12* .
2016-01.

[95] N. Instruments, "NI PXIe-6674T User Manual." http://www.ni.com/pdf/manuals/373089c.pdf, May 2015.

[96] "Octoclock Spec Sheet." http://www.ni.com/datasheet/pdf/en/ds-572, 2014.

[97] "PSS vs SSS in LTE." https://code.facebookf.com/posts/1072680049445290/introducing-facebook-s-new-terrestrial-connectivity-systems-terragraph-and-project-aries/, 2012.

[98] MAMMOET (Massive MIMO for Efficient Transmission) (Jan 2016), "ICT- 619086-D3.2: Distributed and Centralized Baseband Processing Algorithms, Architectures, and Platform,"
EU-project Deliverable.

[99] Y. Rao, "Implementing modified QR decomposition in hardware," July 31 2014.
US Patent App. 13/865,357.

[100] Y. Rao, "Software tool for implementing modified QR decomposition in hardware," Nov. 3 2015.
US Patent 9,176,931.

[101] P. K. S. R. Sonia, Nisha Malik and S. S. Malik, "Uplink Power Control Schemes in Long Term Evolution," in *IJEAT*, vol. 3, February, 2014.

[102] ETSI, *LTE; Evolved Universal Terrestrial Radio Access (E-UTRA); Physical Layer Procedures, ETSI TS 135 231 (V8.8.0)*.

[103] L. Wang, H. Q. Ngo, M. Elkashlan, T. Q. Duong, and K. Wong, "Massive MIMO in Spectrum Sharing Networks: Achievable Rate and Power Efficiency," *IEEE Systems Journal*, vol. 11, pp. 20–31, March 2017.

[104] K. Guo, Y. Guo, G. Fodor, and G. Ascheid, "Uplink power control with MMSE receiver in multi-cell MU-massive-MIMO systems," in *2014 IEEE International Conference on Communications (ICC)*, pp. 5184–5190, June 2014.

[105] H. V. Cheng, E. Björnson, and E. G. Larsson, "Uplink pilot and data power control for single cell massive MIMO systems with MRC," in *2015 International Symposium on Wireless Communication Systems (ISWCS)*, pp. 396–400, Aug 2015.

[106] K. Guo, Y. Guo, and G. Ascheid, "Energy-Efficient Uplink Power Allocation in Multi-Cell MU-Massive-MIMO Systems," in *Proceedings of European Wireless 2015; 21th European Wireless Conference*, pp. 1–5, May 2015.

[107] U. Gustavsson, C. Sanchéz-Perez, T. Eriksson, F. Athley, G. Durisi, P. Landin, K. Hausmair, C. Fager, and L. Svensson, "On the impact of hardware impairments on massive MIMO," in *2014 IEEE Globecom Workshops (GC Wkshps)*, pp. 294–300, Dec 2014.

[108] F. Athley, G. Durisi, and U. Gustavsson, "Analysis of Massive MIMO with hardware impairments and different channel models," in *2015 9th European Conference on Antennas and Propagation (EuCAP)*, pp. 1–5, May 2015.

[109] D. Mi, M. Dianati, L. Zhang, S. Muhaidat, and R. Tafazolli, "Massive MIMO Performance with Imperfect Channel Reciprocity and Channel Estimation Error," *IEEE Transactions on Communications*, vol. PP, no. 99, pp. 1–1, 2017.

[110] E. Björnson, J. Hoydis, M. Kountouris, and M. Debbah, "Massive MIMO Systems With Non-Ideal Hardware: Energy Efficiency, Estimation, and Capacity Limits," *IEEE Transactions on Information Theory*, vol. 60, pp. 7112–7139, Nov 2014.

[111] E. Björnson, E. G. Larsson, and M. Debbah, "Massive MIMO for Maximal Spectral Efficiency: How Many Users and Pilots Should Be Allocated?," *IEEE Transactions on Wireless Communications*, vol. 15, pp. 1293–1308, Feb 2016.

[112] P. Mogensen, W. Na, I. Z. Kovacs, F. Frederiksen, A. Pokhariyal, K. I. Pedersen, T. Kolding, K. Hugl, and M. Kuusela, "LTE Capacity Compared to the Shannon Bound," in *2007 IEEE 65th Vehicular Technology Conference - VTC2007-Spring*, pp. 1234–1238, April 2007.

[113] "5G Researchers Set New World Record For Spectrum Efficiency." Available:https://bit.ly/2LdO5KA, 2016.

[114] S. Wagner, R. Couillet, M. Debbah, and D. T. M. Slock, "Large System Analysis of Linear Precoding in Correlated MISO Broadcast Channels Under Limited Feedback," *IEEE Transactions on Information Theory*, vol. 58, pp. 4509–4537, July 2012.

[115] C. A. Balanis, *Antenna Theory: Analysis and Design*.
Wiley-Interscience, 2005.

[116] H. A. Mahmoud and H. Arslan, "Error vector magnitude to SNR conversion for nondata-aided receivers," *IEEE Transactions on Wireless Communications*, vol. 8, pp. 2694–2704, May 2009.

[117] M. A. Finlayson, *3GPP TS 36.141 version 10.1.0 Release 10*.
3GPP.

[118] M. A. Finlayson, *LTE- Advanced (3GPP Rel.12) Technology Introduction White Paper*.
3GPP.

[119] "Bristol and BT collaborate on massive MIMO trials for 5G wireless." https://goo.gl/RpFdop, 2017.

[120] X. Gao *et al.*, "Massive MIMO performance evaluation based on measured propagation data," *IEEE Transactions on Wireless Communications*, vol. 14, pp. 3899–3911, July 2015.

[121] S. Nowak and R. Kays, "An interleaving scheme for efficient binary LDPC coded higher-order modulation," in *2010 International ITG Conference on Source and Channel Coding (SCC)*, pp. 1–6, Jan 2010.

[122] "5G Layered Realities Weekend." http://www.bristol.ac.uk/news/2018/march/5gexperience.html., 2018.

[123] M. Feng and S. Mao, "Harvest the potential of massive MIMO with multi-layer techniques," *IEEE Network*, vol. 30, pp. 40–45, September 2016.

[124] X. Zou, G. Cui, M. Tang, S. Xiao, and W. Wang, "User grouping method for downlink beamforming in massive MIMO system," in *2014 IEEE 3rd International Conference on Cloud Computing and Intelligence Systems*, pp. 228–233, Nov 2014.

[125] M. Alkhaled, E. Alsusa, and W. Pramudito, "Adaptive user grouping algorithm for the downlink massive MIMO systems," in *2016 IEEE Wireless Communications and Networking Conference*, pp. 1–6, April 2016.

[126] Z. Xiang, M. Tao, and X. Wang, "Massive MIMO Multicasting in Noncooperative Cellular Networks," *IEEE Journal on Selected Areas in Communications*, vol. 32, pp. 1180–1193, June 2014.

[127] H. Zhou and M. Tao, "Joint multicast beamforming and user grouping in massive MIMO systems," in *2015 IEEE International Conference on Communications (ICC)*, pp. 1770–1775, June 2015.

[128] R. A. Shafik, M. S. Rahman, and A. R. Islam, "On the Extended Relationships Among EVM, BER and SNR as Performance Metrics," in *2006 International Conference on Electrical and Computer Engineering*, pp. 408–411, Dec 2006.

[129] T. W. C. Brown, D. A. Humphreys, M. Hudlicka, and T. H. Loh, "Prediction of SINR using BER and EVM for Massive MIMO Applications ," in *12th European Conference on Antennas and Propagation*, 2018.

[130] J. Vieira, F. Rusek, O. Edfors, S. Malkowsky, L. Liu, and F. Tufvesson, "Reciprocity Calibration for Massive MIMO: Proposal, Modeling, and Validation," *IEEE Transactions on Wireless Communications*, vol. 16, pp. 3042–3056, May 2017.

[131] E. Björnson, M. Matthaiou, A. Pitarokoilis, and E. G. Larsson, "Distributed massive MIMO in cellular networks: Impact of imperfect hardware and number of oscillators," in *2015 23rd European Signal Processing Conference (EUSIPCO)*, pp. 2436–2440, Aug 2015.

[132] U. of Bristol, “NI, BT, Bristol and Lund announced winners at the Collaborate to Innovate Awards 2017.” http://www.bris.ac.uk/news/2017/september/massive-mimo.html, 2017.